

Washington University in St. Louis  
**Washington University Open Scholarship**

---

All Theses and Dissertations (ETDs)

---

1-1-2011

# Dynamic Pion Studies in Nuclear Matter

Jonathan Morris

*Washington University in St. Louis*

Follow this and additional works at: <https://openscholarship.wustl.edu/etd>

---

## Recommended Citation

Morris, Jonathan, "Dynamic Pion Studies in Nuclear Matter" (2011). *All Theses and Dissertations (ETDs)*. 621.  
<https://openscholarship.wustl.edu/etd/621>

This Dissertation is brought to you for free and open access by Washington University Open Scholarship. It has been accepted for inclusion in All Theses and Dissertations (ETDs) by an authorized administrator of Washington University Open Scholarship. For more information, please contact [digital@wumail.wustl.edu](mailto:digital@wumail.wustl.edu).

WASHINGTON UNIVERSITY

Department of Physics

Dissertation Committee:

Willem H. Dickhoff, Chairperson

Mark G. Alford

James H. Buckley

Robert J. Charity

Michael C. Ogilvie

Demetrios G. Sarantites

Lee G. Sobotka

Dynamic Pion Studies in Nuclear Matter

by

Jonathan Morris

A dissertation presented to the  
Graduate School of Arts and Sciences  
of Washington University in  
partial fulfillment of the  
requirements for the degree  
of Doctor of Philosophy

December 2011

Saint Louis, Missouri

© Copyright by

Jonathan Morris

December, 2011

ABSTRACT OF THE DISSERTATION

DYNAMIC PION STUDIES IN NUCLEAR MATTER

by

Jonathan Morris

Doctor of Philosophy in Physics

Washington University in Saint Louis, December 2011

Professor Willem H. Dickhoff, Chairperson

A framework is developed which allows the extension of current realistic Nucleon-Nucleon interactions to include pionic degrees of freedom. A prescription for transforming any static pion model to one containing explicit energy dependence is provided. We show that adding energy dependence to the pionic component of the Nucleon-Nucleon interaction reduces the component of  $D$ -state wave function in the deuteron while adding a non-negligible chance of finding the deuteron in an  $NN\pi$  state. Retrofitting the static pion Reid soft-core potential with dynamic pions entailed a necessary refit of the parameters in the central and tensor parts of the potential to phase shifts and deuteron data. Dynamic pions offer a natural and physical way to handle inelasticities in phase shifts above pion-production threshold. Other observables, such as the  $(p, 2p)$  analyzing power  $A_y$ , which indicate explicit energy dependence, have resisted many attempts at modeling using static pion models, but dynamic pion models show some promise at explaining these data. Finally, the effects of dynamic pions in nuclear matter are explored, and it is shown that even below pion-production threshold, allowing pions to propagate leads to a decrease in saturation density without significant change to the overall binding energy per nucleon.

# Acknowledgements

I would first like to thank Prof. Wim Dickhoff for his continued support and guidance. It goes without saying that this project could not have been completed without his insight and ready advice. Although Wim shared with me his deep insight and encyclopedic knowledge, it is his patience, compassion, and understanding of my needs for which I am most grateful. He truly deserves my undying thanks. Thank you also to all of the members of my committee for any helpful comments on the present work.

I wish to also offer my humble gratitude to my wife Anis, whose patience was if anything more sorely tested than Wim's. I am proud to announce that your husband can now fulfill that role full-time! All of those tasks for which I have told you to "consider it done" are now ready to be addressed, or redressed, as the case may be. Thank you so much for your support, both moral and material, through these many years. Thank you for our four wonderful children: Sina, whose many talents are truly an inspiration to all who know her. Koan whose intelligence and humor remind me so much of my own. Alethea whose sweet-"Ness" and happy-"Ness" bring such light and joy to each day. Burke, whose amazing perseverance will undoubtedly lead him to excellence at whatever he chooses to pursue. Additionally, I thank my grandfather who from my earliest memory stressed the importance of lifelong learning (I apparently took that too literally).

Thanks to Dr. Natalie Alexander for helping me somehow manage a triple major in Physics, Classics, and Philosophy. I thank Pat McEwen and the STLCC for helping me find the time to complete this project at long last. I wish also to thank the ECT\* for the excellent training I received in Trento while participating in the Doctoral Training Program, and for allowing me to participate even though I am an American! Finally, I wish to thank the Luthra family for the Nishi Luthra award in support of travel. The time I spent at the ECT\* under your auspices was invaluable. Work was funded in part by the NSF.

# Contents

Abstract . . . . .	ii
Acknowledgements . . . . .	iii
List of Figures . . . . .	vi
List of Tables . . . . .	x
<b>1 Introduction . . . . .</b>	<b>1</b>
1.1 Motivation . . . . .	1
1.2 Outline . . . . .	4
<b>2 Dynamic Reid Formalism and Fit . . . . .</b>	<b>6</b>
2.1 Green's function description of dynamic one-pion-exchange . . . . .	6
2.2 Modification of the Reid soft-core potential . . . . .	13
2.2.1 One-pion-exchange potential . . . . .	15
2.2.2 Reid soft-core . . . . .	16
2.2.3 Dynamic one-pion-exchange potential . . . . .	18
2.3 Fit to data . . . . .	22
2.3.1 Phase shift details . . . . .	22
2.4 Results . . . . .	23
2.4.1 Off-shell $\mathcal{T}$ -matrix . . . . .	26
2.5 Conclusions and discussion . . . . .	26
<b>3 Inelastic Scattering . . . . .</b>	<b>33</b>
3.1 Two-body $A_y$ puzzle . . . . .	33
3.2 Computation of $A_y$ . . . . .	35
3.3 Inelastic $\mathcal{T}$ -matrix . . . . .	38

3.3.1	Lowest-order inelastic ( $p, 2p$ ) . . . . .	39
3.3.2	Higher-order inelastic ( $p, 2p$ ) . . . . .	41
3.4	Results for $A_y$ . . . . .	46
<b>4</b>	<b>Nuclear Matter Saturation Problem . . . . .</b>	<b>57</b>
4.1	Background . . . . .	57
4.2	Calculational details . . . . .	64
4.2.1	Treatment of the Pauli operator . . . . .	66
4.2.2	Calculation of the $G$ -matrix . . . . .	71
4.3	Self-energy and binding . . . . .	75
4.4	Results . . . . .	77
<b>5</b>	<b>Conclusion and Outlook . . . . .</b>	<b>90</b>
	<b>Appendix A Potential Parameters . . . . .</b>	<b>93</b>
A.1	Reid soft-core potential . . . . .	93
A.2	Dynamic Reid 1(DR1) refit parameters . . . . .	94
A.3	Dynamic Reid 1 plots . . . . .	96
A.4	Dynamic Reid 2 (DR2) plots . . . . .	103
	<b>Appendix B <math>G</math>-Matrix Coupled Channels . . . . .</b>	<b>108</b>
	<b>References . . . . .</b>	<b>115</b>

# List of Figures

2.1	Feynman diagram representing the one-pion exchange contribution. . . . .	8
2.2	Time-ordered contribution to dynamic one-pion-exchange. . . . .	10
2.3	Diagrammatic summation of dynamic one-pion-exchange terms relevant for $NN$ scattering. . . . .	11
2.4	$NN$ Ladder diagram . . . . .	12
2.5	Connection between $NN$ propagator and $\mathcal{T}$ -matrix . . . . .	12
2.6	Plot of $\tilde{Q}_{\ell=0}(k, k', 300MeV)$ . . . . .	28
2.7	Plot of RSC and DR1 phase shifts. . . . .	29
2.8	RSC deuteron wave-functions. . . . .	30
2.9	Plot of central part of $V_{O,T}$ for the ${}^3S_1$ channel. . . . .	30
2.10	Plot of DR2 fit to partial-wave analysis isovector phase shifts. . . . .	31
2.11	$\mathcal{T}$ -matrix elements for RSC and DR1 calculated at an energy of 1 MeV (Lab). . . . .	32
2.12	$\mathcal{T}$ -matrix elements for RSC and DR1 calculated at an energy of 300 MeV (Lab). . . . .	32



3.1	$A_y$ versus effective mean density(left) and versus separation energy (right). . . . .	35
3.2	Full inelastic $\mathcal{T}$ -matrix diagram for inelastic $(p, 2p)$ process. . . . .	38
3.3	Lowest-order pion-exchange contribution to the proton induced proton knockout process $(p, 2p)$ . . . . .	40
3.4	Lowest-order pion-exchange contribution to the proton induced proton knockout process as time-ordered terms. . . . .	42
3.5	Higher-order contribution to inelastic $\mathcal{T}$ -matrix diagram for $(p, 2p)$ . . . . .	43
3.6	Higher-order inelastic $\mathcal{T}$ -matrix diagram with momenta repara-metrized and energy $\Omega$ already integrated out. . . . .	45
3.7	$^1S_0$ Potential plot for RSC, elastic DR1, and inelastic DR1. . . . .	48
3.8	$^1D_2$ Potential plot for RSC, elastic DR1, and inelastic DR1. . . . .	49
3.9	$^3P_0$ Potential plot for RSC, elastic DR1, and inelastic DR1. . . . .	50
3.10	$^3P_1$ Potential plot for RSC, elastic DR1, and inelastic DR1. . . . .	51
3.11	$^3P_2$ Potential plot for RSC, elastic DR1, and inelastic DR1. . . . .	52
3.12	$^3F_2$ Potential plot for RSC, elastic DR1, and inelastic DR1. . . . .	53
3.13	$A_y$ computed using DR1, RSC, and PWA. . . . .	54
3.14	Free $A_y$ for 392 MeV (lab) beam energy. . . . .	55
3.15	Proton analyzing power for $pp$ scattering at 100-MeV proton lab energy as a function of the c.m. scattering angle. . . . .	56

4.1	Coester Band. . . . .	61
4.2	$^{208}\text{Pb}$ occupation numbers . . . . .	63
4.3	Saturation points for fully self-consistent treatment of SRC. . . . .	65
4.4	Plot of saturation curves for Bonn B potential using angle-averaged Pauli operator. . . . .	67
4.5	Pauli operator diagrams for the case $\mathbf{K}/2 > k_F$ . . . . .	69
4.6	Pauli operator diagrams for the case $\mathbf{K}/2 < k_F$ . . . . .	70
4.7	Plot of $\bar{Q}(K, q)$ and $k_F \times \frac{\partial \bar{Q}(K, q)}{\partial q}$ for the case $K/2 < k_F$ . . . . .	72
4.8	Plot of $\bar{Q}(K, q)$ and $k_F \times \frac{\partial \bar{Q}(K, q)}{\partial q}$ for the case $K/2 > k_F$ . . . . .	73
4.9	Fermi spheres of $\theta(k_F -  2\mathbf{P} - \mathbf{k} )$ for $k < k_F$ and $k > k_F$ . . . . .	77
4.10	Fermi spheres of $\theta(k_F -  2\mathbf{P} - \mathbf{k} )$ for $2P > k_F$ and $2P < k_F$ . . . . .	78
4.11	Real part of the on-shell self-energies for successive iterations in the case $k_F = 1.36 fm^{-1}$ . . . . .	83
4.12	Real part of the on-shell self-energies for increasing $k_F$ . . . . .	84
4.13	Saturation curves for DR1 and RSC. . . . .	86
4.14	Difference between potential energy contributions to binding energy of the static and the dynamic cases. . . . .	87
A.1	Plot of RSC and DR1 $^1S_0$ phase shifts. . . . .	96
A.2	Plot of RSC and DR1 $^1D_2$ phase shifts. . . . .	97
A.3	Plot of RSC and DR1 $^3P_0$ phase shifts. . . . .	97

A.4	Plot of RSC and DR1 ${}^3P_1$ phase shifts. . . . .	98
A.5	Plot of RSC and DR1 ${}^3P_2$ phase shifts. . . . .	98
A.6	Plot of RSC and DR1 ${}^3F_2$ phase shifts. . . . .	99
A.7	Plot of RSC and DR1 $\epsilon_2$ mixing angles. . . . .	99
A.8	Plot of RSC and DR1 ${}^1P_1$ phase shifts. . . . .	100
A.9	Plot of RSC and DR1 ${}^3D_2$ phase shifts. . . . .	100
A.10	Plot of RSC and DR1 ${}^3S_1$ phase shifts. . . . .	101
A.11	Plot of RSC and DR1 ${}^3D_1$ phase shifts. . . . .	101
A.12	Plot of RSC and DR1 $\epsilon_1$ mixing angles. . . . .	102
A.13	Plot of DR2 ${}^1S_0$ phase shifts. . . . .	104
A.14	Plot of DR2 ${}^1D_2$ phase shifts. . . . .	105
A.15	Plot of DR2 ${}^3P_0$ phase shifts. . . . .	105
A.16	Plot of DR2 ${}^3P_1$ phase shifts. . . . .	106
A.17	Plot of DR2 ${}^3P_2$ phase shifts. . . . .	106
A.18	Plot of DR2 ${}^3F_2$ phase shifts. . . . .	107
A.19	Plot of DR2 $\epsilon_2$ mixing angles. . . . .	107

# List of Tables

2.1	$\chi^2$ /datum for the RSC and DR1. . . . .	24
2.2	Deuteron data for the RSC and DR1. . . . .	25
3.1	Kinematics for direct recoilless $1s_{1/2}$ removal in $^{12}\text{C}$ ( $p, 2p$ ). . . . .	36
4.1	Comparison of gap-choice and continuous-choice contributions to binding energy. . . . .	80
4.2	Contributions to $E/A$ at various densities for all partial waves with total angular momentum $J \leq 2$ for DR1 and RSC. . . . .	81
4.3	Contributions to $E/A$ at various densities, broken down in terms of spin and isospin combinations for both the DR1 and RSC. . . . .	82

# Chapter 1

## Introduction

### 1.1 Motivation

The role of the pion in nuclear physics continues to be a challenging topic even though the relevance of the pion-exchange mechanism for understanding the nucleon-nucleon ( $NN$ ) interaction remains unchallenged. Indeed, the nonvanishing of the deuteron quadrupole moment represents clear evidence for the presence of a substantial tensor component in the  $NN$  interaction which is inevitable for a one-pion exchange mechanism. Modern interactions based on chiral perturbation theory also contain the pion-exchange mechanism explicitly [26, 27], although the complete interaction only contains static contributions. While the importance of pion terms for  $NN$  physics is clear, it has nevertheless been very difficult to establish experimental signatures that point to their presence in nuclei [8].

A promising avenue at one time appeared to be the study of response functions with pion quantum numbers which are expected to be enhanced at intermediate momentum transfer on the basis of infinite matter considerations. Indeed, it was suggested that the pion interacts so strongly with the nuclear-matter medium by coupling to particle-hole and  $\Delta$ -isobar-hole excitations that states with pionic quantum numbers become unstable and an ordered ground state of nuclear matter might be created [44]. The proximity of this pion-condensation transition suggested the study of corresponding response functions but no unambiguous experimental signature was obtained [15, 62, 68].

A direct way to probe the interaction of pions with the nuclear medium is to use real pions and perform scattering experiments. The interpretation of these experiments confirms the strong coupling of such real pions with the medium and the importance of the  $\Delta$ -isobar excitations [50].

The juxtaposition of these two limits involving the strong coupling of real pions with the medium and the essential contribution of pion-exchange to the  $NN$  interaction in which the pion is maximally virtual in the Born term suggests that it may be useful to consider a dynamic treatment of the pion starting at the two-body level. Most  $NN$  interactions do not incorporate such dynamic pion-exchange contributions but some versions of the Bonn potential have included this process [25, 41]. Recent work of the Mainz group [58] also includes some of these features, although the emphasis was on  $NN$  scattering above pion-production threshold, which also requires the explicit treatment of the  $\Delta$ -isobar. Since at this time we do not propose to treat  $NN$  scattering above the pion-production threshold, we will not include the nucleon-pion self-energy term but use experimental masses for nucleons and pions. We note that the inclusion of pion propagation in the medium is best handled in a Green's function method [24, 29]. Previous treatments of pion-propagation in the calculation of the effective interaction in the medium ( $G$ -matrix calculations) have employed the simpler "standard choice" for the single-particle spectrum [39], while our treatment will use the computationally more intensive "continuous choice" advocated by Jeukenne *et al.* [36].

Since a dynamic pion-exchange interaction leads to an energy-dependent  $NN$  interaction, the calculation of the deuteron properties are modified as compared to a static calculation. One consequence being the presence of an  $NN\pi$  component that reduces the  $NN$   $D$ -state probability. We note that the exchange of bosonic degrees of freedom plays a prominent role in electron systems, in particular the electron-electron interaction is dominated by the exchange of plasmon excitations and the electron self-energy is reasonably approximated by including the screened (dynamic) Coulomb interaction, often referred to as the  $GW$ -approximation [43]. A corresponding treatment of pion-exchange is therefore also a possible future application.

Experimental results [65] indicate that short-range correlations (SRC) have the dominant effect on the central density of  $^{208}\text{Pb}$ . It is therefore clear that they should

be included when trying to relate nuclear-matter saturation properties to the those of finite nuclei. In light of this dominance of SRC to nuclear saturation density it has been suggested that the inclusion of long-range pion exchange terms in nuclear matter may be responsible for the difficulties that have plagued a satisfactory resolution of the nuclear-matter saturation problem [21]. Indeed, the suggestion was made some time ago that pion-exchange in infinite matter allows for nontrivial contributions to binding from long-range correlations that will not occur in finite nuclei where momentum is no longer a good quantum number for particle states [22]. In particular, in nuclear-matter calculations, third-order pionic ring diagrams introduce substantial additional binding. This tends to draw the saturation point away from the empirical region. It will therefore be interesting to see if allowing in-medium propagation of pions can ameliorate this difficulty. In order to probe this suggestion it is necessary to construct a dynamic pion-exchange interaction and make a comparison between pion-exchange contributions in finite and infinite systems.

While there is uncertainty about the precise nature of the short-range part of the  $NN$  interaction, there is now evidence from recent lattice QCD calculations that the features of a strong repulsive short-range core emerge from first principles, particularly when the pion mass is reduced towards more realistic values [35]. The presence of short-range correlations is thus corroborated by QCD simulations and strongly suggests that fully microscopic nuclear many-body calculations should continue to address their consequences in detail. Recently developed realistic  $NN$  interactions, like CDBonn [40, 42] or the chiral interactions [26, 27] have in general softer cores than older potentials [30, 45, 55]. Even modern local potentials, such as Argonne v18 (AV18) [70], have a softer core compared to more traditional interactions.

We have decided to modify the older Reid soft-core interaction [54] because it has been widely used in many-body applications involving the Brueckner-Bethe-Goldstone hole-line expansion [18, 59]. In order to assess the difference between the static and dynamic version of the Reid potential it is therefore necessary to fit to the same data that Reid had available. We will demonstrate that a fit to the Nijmegen partial wave analysis (PWA) [60] within this dynamic Reid framework is also possible, confirming the applicability of this approach to all modern  $NN$  interactions. Another reason for continuing to employ  $NN$  interactions with a stronger core is their

capability to provide a depletion of the nuclear Fermi sea that is consistent with experimental observations. Softer interactions like CDBonn [42, 40] and AV18 [70] yield depletions of 11% and 13%, respectively, for the occupation of the zero-momentum state at normal nuclear-matter density [30, 45, 55]. The Reid potential generates a 15% depletion [23] which is closest to the experimental results obtained for deeply bound protons in  $^{208}\text{Pb}$  [65].

Another motivation to explore the possibilities of including dynamic pion-exchange is provided by considerations related to inelastic processes. The  $(e, e'p)$  reaction has been unrivaled as a tool to extract detailed spectroscopic information for bound protons, including absolute spectroscopic factors [38, 51]. Unfortunately, only stable targets can be employed in this reaction and no comparable information for neutrons can be accessed. It is therefore of considerable interest to explore the alternative hadronic  $(p, 2p)$  reaction that can also be used in inverse kinematics to explore the properties of protons in exotic nuclei [37]. In order for such a probe to be successful, it is imperative that experiments on stable targets yield sensible and consistent results in comparison with the  $(e, e'p)$  reaction. While progress is made in this regard with respect to spectroscopic factors [48], a clear puzzle has emerged related to the observed deviation of the polarization observable  $A_y$  for the removal of  $s_{1/2}$ -protons from nuclei [34]. While the use of the impulse approximation appears justified for the beam energies in these  $(p, 2p)$  experiments, it is important to realize that these experiments involve large amounts of energy transfer, typically above 100 MeV. For such inelastic processes it appears essential to allow a picture in which pions can carry such energies while they mediate the interaction. It was also with such future application in mind that the current project was initiated.

## 1.2 Outline

In Chapter 2 we present the Green's function formalism for describing our dynamic one-pion-exchange. We also present the details of the Reid soft-core potential and how we modify it. The details of our refit to experimental data are presented therein, with the explicit fit parameters placed in appendix A. Already at the level of the free  $\mathcal{T}$ -matrix there are consequences to dynamic pion-exchange. For instance, we find



that the D-state probability of the deuteron is significantly reduced. We also note large changes in the off-shell  $\mathcal{T}$ -matrix elements. In addition, this chapter illustrates that our approach offers a viable method for introducing dynamic pions into any interaction containing static pions. We illustrate the possibility of a refit of the original Reid to the PWA of the Nijmegen group [60] in the  $T = 1$  channels. Such a potential refit to modern data could be of use in the future as we explore the usefulness of using pions which carry energy to model inelastic scattering experiments where the pions manifestly carry energy, as in Ch. 3.

In Chapter 3 we discuss a fairly recent set of measurements of the polarization variable  $A_y$  [49]. These experiments demonstrate that in a series of inelastic  $(p, 2p)$  knockout experiments the value of  $A_y$  decreases with increasing separation energy. The failure to explain these data with free  $NN$   $\mathcal{T}$ -matrices has inspired us to develop a framework for describing inelastic scattering experiments based on a dynamically generated  $\mathcal{T}$ -matrix. Although we do not totally solve this two-body  $A_y$  problem, the approach developed in chapter 3 is a more natural way to describe inelastic two-body scattering.

In Chapter 4, we turn to a discussion of the nuclear-matter saturation problem. A brief historical overview of the problem is offered, followed by a discussion of the formalism for treatment of this problem using the Brueckner-Hartree-Fock approximation. We explore the effect of dynamic pion propagation on the on-shell self-energy and the consequences for nuclear-matter saturation. We demonstrate that at the level of Brueckner-Hartree-Fock, dynamic pion propagation leads to a smaller saturation density without appreciably changing the binding energy per nucleon. This shift moves the calculation toward the empirical region, and shows promise for later inclusion in more sophisticated treatments.

Finally, in Chapter 5 we discuss the most likely avenues for adaptation of our framework to other realistic  $NN$  interactions. We also suggest ways that our dynamic potential could be included in more sophisticated many-body calculations to improve the agreement between nuclear-matter calculations and the saturation properties of finite nuclei.

# Chapter 2

## Dynamic Reid Formalism and Fit

### 2.1 Green's function description of dynamic one-pion-exchange

The basic process that we plan to incorporate is the possibility of a pion propagating in its true sense from one nucleon to another. At the same time, we intend to limit ourselves to this process only, *i.e.* having only one pion present at any time. It is the treatment of this dynamic feature over the standard static mechanism that we plan to investigate with regard to its relevance for in-medium considerations and inelastic processes. We will therefore continue to represent dynamic two-pion-exchange and other mechanisms by phenomenology. If the dynamic pion-exchange provides useful new insights, subsequent implementation in other realistic interactions is straightforward. A reconsideration of this effect in the context of chiral interactions may then also be necessary.

The relevant Green's functions for consideration are the noninteracting free nucleon, treated nonrelativistically,

$$G^{(0)}(\mathbf{k}; E) = \frac{1}{E - \varepsilon(\mathbf{k}) + i\eta}, \quad (2.1)$$

where spin and isospin indices have been suppressed and (with  $\hbar = c = 1$  throughout) the energy

$$\varepsilon(\mathbf{k}) = \frac{k^2}{2m} \quad (2.2)$$

only includes kinetic energy in free space. For the pion we write

$$D^\pi(\mathbf{q}; \omega) = \frac{1}{\omega^2 - m_\pi^2 - q^2 + i\eta} = \frac{1}{2\sqrt{m_\pi^2 + q^2}} \times \left\{ \frac{1}{\omega - \sqrt{m_\pi^2 + q^2} + i\eta} - \frac{1}{\omega + \sqrt{m_\pi^2 + q^2} - i\eta} \right\}, \quad (2.3)$$

decomposing the boson propagator into a forward- and backward-going term and identifying the free pion energy

$$\varepsilon^\pi(q) = \sqrt{m_\pi^2 + q^2}. \quad (2.4)$$

The dynamic one-pion-exchange contribution to the  $NN$  interaction can be generated by considering the following integration procedure based on the diagram shown in Fig. 2.1. The appropriate propagator to consider is

$$I_\pi(\mathbf{k}, \mathbf{k}'; \Omega) = \int \frac{d\omega}{2\pi i} \int \frac{d\omega'}{2\pi i} G^{(0)}(\mathbf{k}; \Omega/2 + \omega) G^{(0)}(-\mathbf{k}; \Omega/2 - \omega) \times D^\pi(\mathbf{k}' - \mathbf{k}; \omega' - \omega) G^{(0)}(\mathbf{k}'; \Omega/2 + \omega') G^{(0)}(-\mathbf{k}'; \Omega/2 - \omega'). \quad (2.5)$$

We anticipated working in the center-of-mass of the  $NN$  system implying equal and opposite momenta of the nucleons in the initial and final state. Using the decomposition of Eq. (2.3), the two energy integrations can be performed straightforwardly employing contour integration with the result

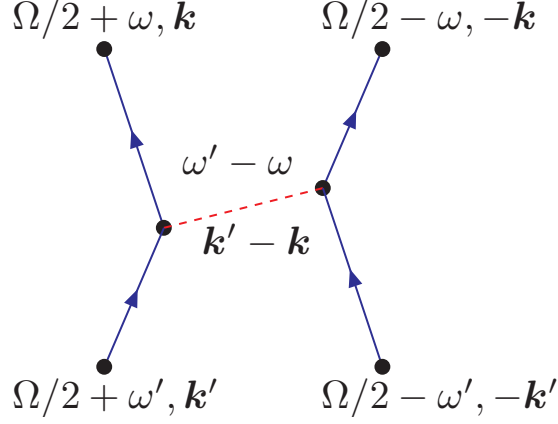


Figure 2.1: Feynman diagram representing the one-pion exchange contribution.

$$\begin{aligned}
I_\pi(\mathbf{k}, \mathbf{k}'; \Omega) &= \frac{1}{2\varepsilon^\pi(|\mathbf{k}' - \mathbf{k}|)} \frac{1}{\Omega - \varepsilon(\mathbf{k}) - \varepsilon(-\mathbf{k}) + i\eta} \\
&\times \frac{1}{\Omega - \varepsilon(\mathbf{k}) - \varepsilon(-\mathbf{k}') - \varepsilon^\pi(|\mathbf{k}' - \mathbf{k}|) + i\eta} \frac{1}{\Omega - \varepsilon(\mathbf{k}') - \varepsilon(-\mathbf{k}') + i\eta} \\
&+ \frac{1}{2\varepsilon^\pi(|\mathbf{k}' - \mathbf{k}|)} \frac{1}{\Omega - \varepsilon(\mathbf{k}) - \varepsilon(-\mathbf{k}) + i\eta} \\
&\times \frac{1}{\Omega - \varepsilon(\mathbf{k}') - \varepsilon(-\mathbf{k}) - \varepsilon^\pi(|\mathbf{k}' - \mathbf{k}|) + i\eta} \frac{1}{\Omega - \varepsilon(\mathbf{k}') - \varepsilon(-\mathbf{k}') + i\eta}. \tag{2.6}
\end{aligned}$$

The resulting two time-ordered contributions are shown in Fig. 2.2. Apart from the prefactor both terms represent two-nucleon propagators for the initial and final state with an intermediate propagator representing two nucleons and a pion. In free space the two time-ordered terms are identical and the propagator of Eq. (2.5) reads

$$I_\pi(\mathbf{k}, \mathbf{k}'; \Omega) = \frac{1}{\varepsilon^\pi(|\mathbf{k}' - \mathbf{k}|)} G_{NN}^{(0)}(k; \Omega) G_{NN\pi}^{(0)}(\mathbf{k}, \mathbf{k}'; \Omega) G_{NN}^{(0)}(k'; \Omega), \tag{2.7}$$

where

$$G_{NN}^{(0)}(k; \Omega) = \frac{1}{\Omega - 2\varepsilon(k) + i\eta} \tag{2.8}$$

is the free two-nucleon propagator and

$$G_{NN\pi}^{(0)}(\mathbf{k}, \mathbf{k}'; \Omega) = \frac{1}{\Omega - \varepsilon(k) - \varepsilon(k') - \varepsilon^\pi(|\mathbf{k}' - \mathbf{k}|) + i\eta} \quad (2.9)$$

represents the free propagation of two nucleons and a pion. The latter term still depends on the angle between  $\mathbf{k}$  and  $\mathbf{k}'$  in the free pion energy which also appears as a factor in Eq. (2.7). This angular dependence is projected out when the partial-wave basis is employed to describe the  $NN$  scattering process.

Alternatively, it is possible to identify the effective energy  $\tilde{\omega}$  for the pion propagator

$$D^\pi(|\mathbf{k}' - \mathbf{k}|; \tilde{\omega}) = \frac{1}{\tilde{\omega}^2 - m_\pi^2 - (\mathbf{k}' - \mathbf{k})^2 + i\eta} \quad (2.10)$$

with

$$\tilde{\omega}^2 = \left( \Omega - \frac{k^2 + k'^2}{2m} \right) \sqrt{m_\pi^2 + (\mathbf{k} - \mathbf{k}')^2}. \quad (2.11)$$

In the Born approximation, the propagation energy is equal to the relative energy and  $\tilde{\omega}$  vanishes, yielding the conventional static one-pion-exchange contribution. The dynamic contribution will therefore contribute in second and higher order in the construction of the  $NN$   $\mathcal{T}$ -matrix. By isolating the term with one pion in flight, as in Eq. (2.7), we avoid terms that would generate more than one pion in flight contributions when we determine the  $NN$   $\mathcal{T}$ -matrix.

For future applications not involving elastic processes, it is useful to develop the construction of the  $\mathcal{T}$ -matrix from the propagator formulation. Since initial and final state must correspond to two nucleons, it is indeed sufficient to consider the two-time version of the  $NN$  propagator which therefore leads to a single energy variable upon Fourier transformation [24]. Summing all terms in which at most one pion is in flight at any time is accomplished as follows

$$G_{NN}(\mathbf{k}, \mathbf{k}'; \Omega) = G_{NN}^{(0)}(\mathbf{k}, \mathbf{k}'; \Omega) + \frac{1}{2} \int \frac{d^3q}{(2\pi)^3} G_{NN}^{(0)}(\mathbf{k}; \Omega) \langle \mathbf{k} | (V_\pi(\Omega) + \Delta V) | \mathbf{q} \rangle G_{NN}(\mathbf{q}, \mathbf{k}'; \Omega) \quad (2.12)$$

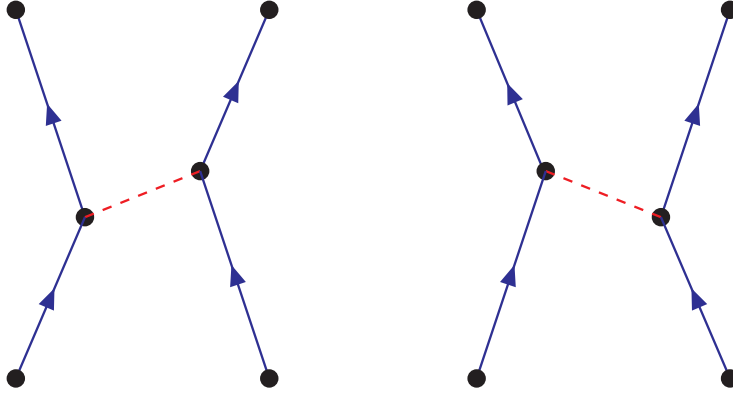


Figure 2.2: Time-ordered contribution to dynamic one-pion-exchange.

shown diagrammatically in Fig. 2.3 with individual terms identified in Fig 2.4. Note that spin and isospin degrees of freedom have been suppressed to simplify the notation in Eq. (2.12). The first term on the right side of Eq. (2.12) contains both direct and exchange contributions with corresponding delta-functions in the associated relative momenta, whereas the second noninteracting propagator corresponds to Eq. (2.8). The interaction matrix element denoted by  $V_\pi$  also contains the spin and isospin coupling of the pion to the nucleons in addition to the propagator of Eq. (2.10), as well as the relevant coupling constant. The diagonal dashed line in Figs. 2.3 and 2.4 represents dynamic pion exchange and Eq. (2.12) should be interpreted to iterate any number of times the process represented in lowest order by Eq. (2.7). To reiterate once more, the sequence of terms generated by Eq. (2.12) always starts with two nucleons, then can propagate as an  $NN\pi$  state but always returns to an  $NN$  state before possibly returning to an  $NN\pi$  state, while always ending up with two nucleons in the final state. To emphasize that only the one-pion-exchange part of the  $NN$  interaction is dynamic we have included an explicit  $\Delta V$  contribution to represent the static part in Eq. (2.12).

The construction of the corresponding  $\mathcal{T}$ -matrix from the  $NN$  propagator follows by clipping the initial and final noninteracting  $NN$  propagators from the first- and higher-order terms in Fig. 2.4. The corresponding summation can be rearranged

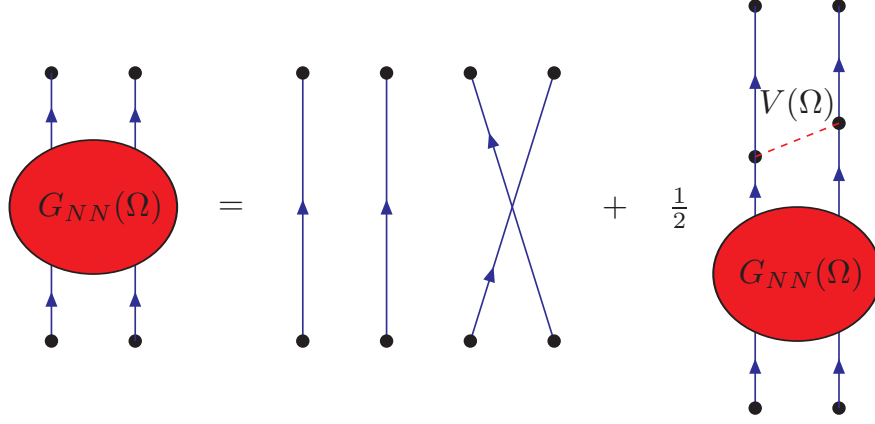


Figure 2.3: Diagrammatic summation of dynamic one-pion-exchange terms relevant for  $NN$  scattering. The dashed diagonal line represents both the dynamic one-pion-exchange term and additional static contributions.

according to

$$\begin{aligned} \langle \mathbf{k} | \mathcal{T}(\Omega) | \mathbf{k}' \rangle &= \langle \mathbf{k} | (V_\pi(\Omega) + \Delta V) | \mathbf{k}' \rangle \\ &+ \frac{1}{2} \int \frac{d^3q}{(2\pi)^3} \langle \mathbf{k} | (V_\pi(\Omega) + \Delta V) | \mathbf{q} \rangle G_{NN}^{(0)}(\mathbf{q}; \Omega) \langle \mathbf{q} | \mathcal{T}(\Omega) | \mathbf{k}' \rangle. \end{aligned} \quad (2.13)$$

We represent this result diagrammatically in Fig. 2.5 and clarify the inverse relation with  $G_{NN}$  in the second equality. The latter result can also be verified diagrammatically [24].

The homogeneous eigenvalue equation for the deuteron bound state is also modified due to the presence of the energy dependence. The proper derivation of this result proceeds from Eq. (2.12) and assumes a Lehmann representation of the full propagator which contains possible bound states. Since the noninteracting propagator does not contain negative energy poles, a homogeneous eigenvalue problem arises when one considers energies in the vicinity of the possible bound states. The corresponding eigenvalue equation in momentum space appropriate for the deuteron then

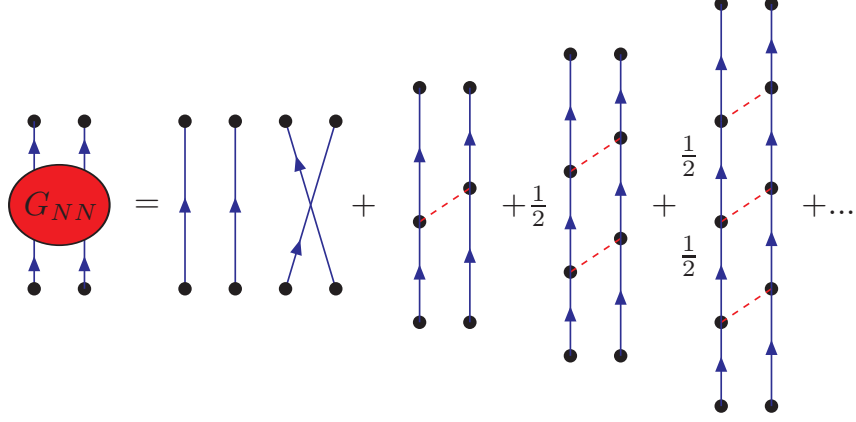


Figure 2.4: Individual terms summed by Eq. (2.12).

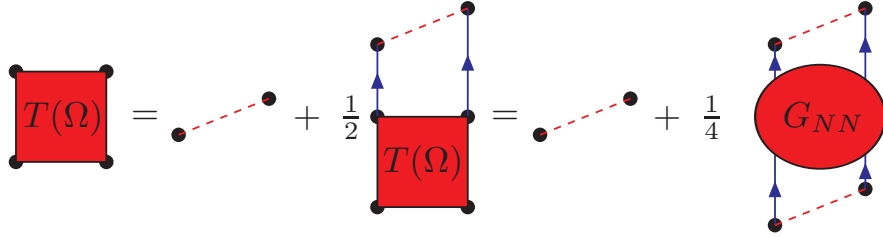


Figure 2.5: Summation for  $\mathcal{T}$ -matrix contributions also clarifying the relation with the  $NN$  propagator in the second equality.

becomes [24]

$$\begin{aligned} \frac{\hbar^2 k^2}{m} \psi_n(k(\ell S)JT) + \sum_{\ell'} \int \frac{dq q^2}{2(2\pi)^3} \langle k\ell | V^{JST}(E_n) | q\ell' \rangle \\ \times \psi_n(q(\ell' S)JT) = E_n \psi_n(k(\ell S)JT). \end{aligned} \quad (2.14)$$

Note that the projected  $NN$  interaction containing the dynamic pion-exchange contribution must be calculated at the deuteron energy which is a general property of eigenvalue equations derived from energy-dependent potentials [24]. The presence of



such an energy dependence also changes the normalization of the wave function amplitudes [24]. Indeed due to the dynamic pion-exchange term the normalization of the  $S$ - and  $D$ -state components of the  $NN$  part of the deuteron wave-function changes on account of the small presence of the not explicitly calculated  $NN\pi$  contribution. The corresponding probability for this  $NN\pi$  contribution is then given by

$$\begin{aligned}
P(NN\pi) &= \sum_{\ell\ell'} \int \frac{dq}{2(2\pi)^3} q^2 \int \frac{dq'}{2(2\pi)^3} q'^2 \psi_n^*(q(\ell S)JT) \\
&\times \left. \frac{\partial \langle q\ell | V^{JST}(E) | q'\ell' \rangle}{\partial E} \right|_{E_n} \psi_n(q'(\ell' S)JT) \quad (2.15)
\end{aligned}$$

and obviously leads to a reduction of the traditional  $D$ -state probability.

The present treatment of dynamic pion-exchange contains features that are similar to the treatment presented in Ref. [25], where all meson exchanges are considered using time-ordered perturbation theory. However, they do not take into account the probability of an  $NN\pi$  state [Eq. (2.15)] when they normalize. We do not however include the pion self-energy contribution and can therefore employ the physical mass of the nucleon but our result cannot immediately be extended above pion-production threshold without such terms explicitly considered. Since the current emphasis on chiral models of the  $NN$  interaction [26, 27] suggests a focus on pion-exchange terms, it is useful to limit the dynamic treatment of the exchange mechanism to its simplest manifestation as in the present formulation. We further advocate the study of this effect for the Reid soft-core (RSC) interaction as it has been one of the most employed realistic interactions in the context of many-body calculations based on diagrammatic approaches. In addition, it appears that  $(e, e'p)$  data favor a depletion of the proton Fermi sea in  $^{208}\text{Pb}$  [65] more in line with those obtained for harder interactions [55] like the RSC.

## 2.2 Modification of the Reid soft-core potential

A multitude of nuclear scattering data exist, and although they do not uniquely specify the form of the forces between nucleons, they do require that the potential

has certain components. Scattering data clearly require the presence of the one-pion-exchange contribution, while the quadrupole moment of the deuteron provides further evidence for the presence of a corresponding pion-exchange tensor force. The short range of the nuclear interaction (relative to electromagnetic forces) was first suggested by Yukawa [71] in 1935 proposing the exchange of a massive particle between nucleons. The corresponding radial dependence is given by

$$V_Y(r) = V_0 \frac{e^{-\mu r}}{\mu r}. \quad (2.16)$$

We can interpret this as representing the exchange of a particle of mass  $\mu$ . In order to discuss the changes involved with an energy dependent (dynamic) Yukawa interaction, a few features of the energy independent (static) version should be mentioned. The decomposition of the static Yukawa interaction into partial waves relies on the expansion of the static propagator

$$\begin{aligned} D^\pi(\mathbf{k}, \mathbf{k}') &= -\frac{1}{m_\pi^2 + (\mathbf{k} - \mathbf{k}')^2} \\ &= -\frac{1}{2kk'} \frac{1}{\left(\frac{m_\pi^2 + k^2 + k'^2}{2kk'}\right) - \cos \theta_{kk'}} \\ &= -\frac{1}{2kk'} \sum_{\ell=0}^{\infty} (2\ell + 1) Q_\ell(z) P_\ell(\cos \theta_{kk'}), \end{aligned} \quad (2.17)$$

where  $\theta_{kk'}$  is the angle between  $\hat{\mathbf{k}}$  and  $\hat{\mathbf{k}'}$ ,

$$z = \frac{m_\pi^2 + k^2 + k'^2}{2kk'}, \quad (2.18)$$

and  $Q_\ell$  is a Legendre function of the second kind. We can therefore expand the propagator according to

$$D^\pi(\mathbf{k}, \mathbf{k}') = \sum_{\ell=0}^{\infty} D_\ell^\pi(k, k') P_\ell(\cos \theta_{kk'}), \quad (2.19)$$

with

$$D_\ell^\pi(k, k') = \frac{2\ell + 1}{2} \int_{-1}^1 d \cos \theta_{kk'} P_\ell(\cos \theta_{kk'}) D^\pi(\mathbf{k}, \mathbf{k}') = -\frac{2\ell + 1}{2kk'} Q_\ell(z). \quad (2.20)$$

The projection of this propagator in a partial-wave basis then yields for the Yukawa interaction of Eq. (2.16)

$$\langle kLM | V_Y | k'L'M' \rangle = \delta_{LL'} \delta_{MM'} \frac{(4\pi)^2 V_0}{m_\pi 2kk'} Q_L(z). \quad (2.21)$$

As discussed above, we have chosen to study the effects of dynamic pion-exchange by modifying the Reid soft-core (RSC) interaction [54], but in principle the procedure can be adapted to the one-pion-exchange term of any realistic interaction.

### 2.2.1 One-pion-exchange potential

Before discussing the Reid potential, it will be useful to provide more details of the one-pion-exchange potential (OPEP). In momentum space, this potential has three parts, which we label  $A_1$ ,  $A_2$ , and  $A_3$  respectively. Defining  $\mathbf{q} \equiv \mathbf{k} - \mathbf{k}'$ , we can write the OPEP as follows:

$$V_\pi = -\frac{f_\pi^2}{m_\pi^2} \left[ \frac{1}{3} \frac{S_{12}(\hat{q}) \mathbf{q}^2 \boldsymbol{\tau}_1 \cdot \boldsymbol{\tau}_2}{m_\pi^2 + \mathbf{q}^2} + \frac{1}{3} \boldsymbol{\sigma}_1 \cdot \boldsymbol{\sigma}_2 \boldsymbol{\tau}_1 \cdot \boldsymbol{\tau}_2 - \frac{1}{3} \frac{m_\pi^2 \boldsymbol{\sigma}_1 \cdot \boldsymbol{\sigma}_2 \boldsymbol{\tau}_1 \cdot \boldsymbol{\tau}_2}{m_\pi^2 + \mathbf{q}^2} \right]. \quad (2.22)$$

Here, the term  $S_{12}(\hat{q})$  is the tensor operator given by

$$S_{12}(q) = 3\boldsymbol{\sigma}_1 \cdot (\mathbf{q}) \boldsymbol{\sigma}_2 \cdot (\mathbf{q}) - \mathbf{q}^2 \boldsymbol{\sigma}_1 \cdot \boldsymbol{\sigma}_2, \quad (2.23)$$

which possibly connects states of different orbital angular momentum for total spin  $S = 1$  states, if allowed by parity conservation. For reference,

$$A_1 = -\frac{1}{3} \frac{S_{12}(\hat{q}) \mathbf{q}^2 \boldsymbol{\tau}_1 \cdot \boldsymbol{\tau}_2}{m_\pi^2 + \mathbf{q}^2} \quad (2.24)$$

$$A_2 = -\frac{1}{3} \boldsymbol{\sigma}_1 \cdot \boldsymbol{\sigma}_2 \boldsymbol{\tau}_1 \cdot \boldsymbol{\tau}_2 \quad (2.25)$$

$$A_3 = \frac{1}{3} \frac{m_\pi^2 \boldsymbol{\sigma}_1 \cdot \boldsymbol{\sigma}_2 \boldsymbol{\tau}_1 \cdot \boldsymbol{\tau}_2}{m_\pi^2 + \mathbf{q}^2}, \quad (2.26)$$

The second term,  $A_2$ , is a constant, and in position space represents only a delta function contact force, which was never included in the original RSC. Let us then consider the central term,  $A_3$  which is diagonal in angular momentum. The basic numerical approach may be easily generalized to the coupled-channel tensor force. Recall the expansion of the energy independent propagator in terms of Legendre Functions and Legendre Polynomials (Eq. 2.19). If we want to select a particular value of angular momentum  $L$ , we can easily project it by multiplying by  $P_L(\cos(\theta_{kk'}))$  and integrating. Because of the orthogonality of the Legendre polynomials [2], only the  $l = L$  term will survive the integration as in Eq. (2.20) for the static case. We see that we can derive the expression for a particular partial wave by projection. This result can also be derived by performing a Fourier-Bessel transform on the position space representation of the Yukawa potential [12]. Our numerical scheme is to perform the same projection on the energy-dependent Yukawa potentials and express the partial waves in terms of energy dependent Extended Legendre Functions (ELFs)  $\tilde{Q}_L(k, k'; \Omega)$  rather than the Legendre functions  $Q_L(k, k')$ . This treatment of the ELFs is presented in section 2.2.3.

## 2.2.2 Reid soft-core

Although we could in principle apply this formalism to any Yukawa type potential, we chose the Reid soft-core (RSC) as a model Yukawa type interaction because of its soft (but not too soft) core, and its phenomenological treatment of higher meson mass and multiple-pion exchange. The RSC was a popular potential in the late sixties, which was fit directly to phase shift analyses [5]. This potential was constructed

with separate parameters for each partial wave. For illustration purposes, we provide below two examples of the type of fit used by Reid (in position space). We retain the notation of Reid, who uses *e.g.*  $V(^1S_0)$  to indicate the  $^1S_0$  channel of the potential in position space with the explicit  $x$  dependence understood. The full RSC is printed for reference in Appendix A.1.

$$V(^1S_0) = -h \frac{e^{-x}}{x} - 1650.6 \frac{e^{-4x}}{x} + 6484.2 \frac{e^{-7x}}{x} \quad (2.27)$$

where  $h = 10.463$  MeV. In the RSC,  $x = \mu r$  where  $\mu$  is the average pion mass in appropriate units  $m_\pi c^2 / \hbar c = 0.70 fm^{-1}$ . Thus, for each partial wave the RSC uses only phenomenological Yukawa terms with multiples of the pion mass. Other, heavier meson masses do not appear explicitly in the potential, but rather are handled phenomenologically with simulated multiple-pion exchange.

For the coupled channels (stemming from the presence of the tensor force) Reid has the following:

$$V(^3S_1 - ^3D_1) = V_C + V_T S_{12} + V_{LS} \mathbf{L} \cdot \mathbf{S} \quad (2.28)$$

where

$$V_C = h \frac{e^{-x}}{x} + 105.468 \frac{e^{-2x}}{x} - 3187.8 \frac{e^{-4x}}{x} + 9924.3 \frac{e^{-6x}}{x} \quad (2.29)$$

$$V_T = -h \left[ \left( 1 + \frac{3}{x} + \frac{3}{x^2} \right) \frac{e^{-x}}{x} - \left( \frac{12}{x} + \frac{3}{x^2} \right) \frac{e^{-4x}}{x} \right] \\ + 351.77 \frac{e^{-4x}}{x} - 1673.5 \frac{e^{-6x}}{x} \quad (2.30)$$

$$V_{LS} = 708.91 \frac{e^{-4x}}{x} - 2713.1 \frac{e^{-6x}}{x}. \quad (2.31)$$

The complicated structure of the tensor force is due in part to the presence of the tensor operator, and in part to the need to regulate the potential for small  $x$ . In momentum space, the Yukawa terms are replaced by Legendre functions as indicated

above [see Eq. (2.21)]. In our dynamic model, we add energy dependence only to the pion terms (all those attached to the coupling constant  $h$ ), while keeping all of the phenomenological higher mass terms static. After explaining the formalism of the dynamic pion, we will see that we were easily able to refit the dynamic potential often only changing two of the fit parameters in Reid's original potential.

### 2.2.3 Dynamic one-pion-exchange potential

We will now provide some additional details for the implementation of the dynamic one-pion-exchange interaction in a partial-wave basis. In momentum space, this non-relativistic contribution can be decomposed according to

$$V_\pi(\mathbf{k}, \mathbf{k}'; \Omega) = \frac{1}{3} \frac{f_\pi^2}{m_\pi^2} \left[ \frac{S_{12}(\mathbf{q}) \boldsymbol{\tau}_1 \cdot \boldsymbol{\tau}_2}{\tilde{\omega}^2 - m_\pi^2 - \mathbf{q}^2 + i\eta} - \frac{m_\pi^2 \boldsymbol{\sigma}_1 \cdot \boldsymbol{\sigma}_2 \boldsymbol{\tau}_1 \cdot \boldsymbol{\tau}_2}{\tilde{\omega}^2 - m_\pi^2 - \mathbf{q}^2 + i\eta} \right], \quad (2.32)$$

where  $\tilde{\omega}$  is given by Eq. (2.11) and  $\mathbf{q} = \mathbf{k}' - \mathbf{k}$ . For the static version, the energy  $\tilde{\omega}$  is zero, allowing no transfer of energy by the pion. This potential corresponds to the addition of an energy transfer to  $A_1$  and  $A_3$  from Eq. (2.26). The term which leads to a  $\delta$ -function in coordinate space ( $A_2$ ) has been left out, since it is not considered in the original RSC either. The main difference between the dynamic and static version of the tensor and Yukawa term lies of course in the denominator representing the pion propagator. The projection onto angular momentum states therefore requires the consideration of the angular dependence of the pion propagator

$$\begin{aligned} D^\pi(\mathbf{k}, \mathbf{k}'; \Omega) &= \frac{1}{\tilde{\omega}^2 - m_\pi^2 - \mathbf{q}^2 + i\eta} \\ &= \frac{1}{2kk'} \frac{1}{\beta \sqrt{z - \cos \theta_{kk'}} - (z - \cos \theta_{kk'}) + i\eta}, \end{aligned} \quad (2.33)$$

where  $\tilde{\omega}$  was defined in Eq. (2.11),  $z$  in Eq. (2.18), and the energy dependence is completely contained in  $\beta \equiv (\Omega - (k^2 + k'^2)/2m) / \sqrt{2kk'}$ . It is therefore possible to project this propagator in complete analogy to Eq. (2.19). The required integration therefore involves

$$\begin{aligned}
D_\ell^\pi(k, k'; \Omega) &= \frac{2\ell + 1}{2} \int_{-1}^1 d \cos \theta_{kk'} P_\ell(\cos \theta_{kk'}) D^\pi(\mathbf{k}, \mathbf{k}'; \Omega) \\
&\equiv -\frac{2\ell + 1}{2kk'} \tilde{Q}_\ell(z; \Omega),
\end{aligned} \tag{2.34}$$

defining  $\tilde{Q}_\ell$ , the energy-dependent generalization of the Legendre function  $Q_\ell$ . With the introduction of  $\tilde{Q}_\ell(z; \Omega)$  the problem of generating matrix elements of the Yukawa and tensor terms of the dynamic pion-exchange reduces to the same exercise as for the static version with  $\tilde{Q}_\ell$  replacing  $Q_\ell$ . To generate the energy-dependent matrix elements we can employ a numerical treatment of Eq. (2.34). This integral can also be performed analytically, although the usefulness of this analytical treatment is reduced by the presence of divergent terms.

The following are the steps that generate an analytical expression for the partial-wave projected dynamic one-pion-exchange contribution. We start with the propagator given in the form of Eq. (2.33) which exhibits the relevant angular dependence. Before exploring how this modified propagator changes the partial-wave expansion, we point out a few features. First, the energy dependence is entirely contained in  $\beta$ , which is zero for on-shell values of the energy  $\Omega$ . We see therefore that in the on-shell limit ( $\beta \rightarrow 0$ ) the propagator reduces to the static one. The effects of adding dynamic pions will therefore strictly be an off-shell effect. Second, we see that the dependence on  $\cos \theta_{kk'}$  appears inside a square root. This will change the structure of the integral for the projection with Legendre polynomials.

The integral in Eq. (2.34) can most easily be performed by making the substitution  $q = \sqrt{z - \cos \theta}$  yielding

$$D_\ell^\pi(k, k'; \Omega) = -\frac{2\ell + 1}{2kk'} \int_{\sqrt{z-1}}^{\sqrt{z+1}} \frac{P_\ell(z - q^2) dq}{q - \beta - i\eta}. \tag{2.35}$$

We can see from this form that the numerator will be a polynomial in powers of  $q^2$ , so we will need to perform for each value of angular momentum  $\ell$  integrals of the form

$$\begin{aligned}
\int_a^b \frac{q^n}{q - \beta - i\eta} &= \wp \int_a^b \frac{q^n}{q - \beta} + \int_a^b i\pi\delta(q - \beta)q^n \\
&= \sum_{j=1}^n \binom{n}{j} \frac{q^j}{j} \beta^{n-j} \Big|_{a-\beta}^{b-\beta} + \beta^n \ln \left( \left| \frac{b - \beta}{a - \beta} \right| \right) + i\pi\beta^n.
\end{aligned} \tag{2.36}$$

The imaginary part only occurs if we integrate across a pole ( $a < \beta < b$ ). The pole occurs whenever the energy is greater than the pion-production threshold, so in a natural way becomes complex allowing for pion production and complex phase shifts. We can now expand the Legendre polynomials in powers of  $q$  and integrate. Using the expansion of  $P_\ell$  given in Ref. [2], we find

$$P_\ell(z - q^2) = \sum_{k=0}^{\lfloor \frac{\ell}{2} \rfloor} \frac{(-1)^k (2\ell - 2k)!}{2^\ell (\ell - k)! (\ell - 2k)!} (z - q^2)^{\ell - 2k}, \tag{2.37}$$

where  $\lfloor \frac{\ell}{2} \rfloor = \frac{\ell}{2}$  if  $\ell$  is even, and  $\lfloor \frac{\ell}{2} \rfloor = \frac{\ell-1}{2}$  if  $\ell$  is odd. Using these results, we obtain

$$\begin{aligned}
D_\ell^\pi(k, k'; \Omega) &= -\frac{2\ell + 1}{2kk'} \sum_{n=0}^{\lfloor \frac{\ell}{2} \rfloor} \frac{(-1)^n (2\ell - 2n)!}{2^\ell (\ell - n)! (\ell - 2n)!} \\
&\quad \sum_{j=0}^{\ell - 2n} \binom{\ell - 2n}{j} z^j (-1)^{\ell - 2n - j} \left( (1 - \delta_{2\ell - 4n - 2j, 0}) \right. \\
&\quad \times \sum_{i=1}^{2\ell - 4n - 2j} \left( \frac{(q - \beta)^i \beta^{2\ell - 4n - 2j} \binom{2\ell - 4n - 2j}{i}}{i} \right) \\
&\quad \left. + \beta^{2\ell - 4n - 2j} \ln |q - \beta| + i\pi\beta^{2\ell - 4n - 2j} \right) \Big|_{q=\sqrt{z-1}}^{q=\sqrt{z+1}}, \tag{2.38}
\end{aligned}$$

where it is understood that the imaginary part only exists for energies above pion-production threshold. A few features of these functions should be noted.



1. Taking the limit  $\beta \rightarrow 0$ , which corresponds to turning off the energy dependence, or considering on-shell values, generates the familiar Legendre functions  $Q_\ell(z)$  up to a factor.
2. The individual powers of  $z$  and  $\beta$  have small  $k, k'$  behavior like  $\frac{1}{kk'}$ . These terms are each divergent for small  $k, k'$  but the sum of all terms is well behaved. The divergences become worse for larger  $\ell$ , with the worst one generally being of the form  $(\frac{1}{kk'})^{2\ell+1}$ . This is a feature also encountered for the  $Q_\ell(z)$ .
3. As  $\ell$  increases, the number of terms grows rapidly. Because each of these terms is divergent for small  $k$  or  $k'$ , and the number of terms becomes large, the cancellation of terms becomes numerically difficult to control. This makes the analytical expression cumbersome to work with numerically for large  $\ell$ , so for large  $\ell$  it is convenient to solve Eq. (2.34) through numerical integration.

The analytical solution is useful for exploring the features of this interaction, and provides a useful comparison with our numerical approach. For low  $\ell$  the analytical expression is sufficiently stable to use for fitting phase shift data. Figure 2.6 provides a 3-d plot that illustrates the dependence on  $k, k'$  of  $\tilde{Q}_\ell(k, k', \Omega)$  for  $\ell = 0$  above pion-production threshold.

Due to the increasing instability of our analytical projection for increasing  $\ell$ , we find it expedient to perform the integral in Eq. (2.34) numerically. Using only twelve points for energies below pion-production threshold, and a Gaussian quadrature, we find results that agree with the analytic expression (in regimes where that expression is stable) to high precision. The numerical projection is perfectly stable for small  $k$  and  $k'$ . However, for energies above pion-production threshold, integration across the pion pole leads to some difficulty. From the analytic expression plotted in Fig. 2.6 we observe a sharp cusp-like structure occurring in locations that vary with energy in a roughly parabolic shape in the  $k - k'$  plane. We smoothed the sharpness of this structure by including a 5 MeV width  $\Delta$  with the prescription  $\beta \rightarrow \beta + i\Delta$  for energies above pion-production threshold. We also found it necessary to increase the number of Gaussian quadrature points to as many as 96 for these energies to assure stability of the projection above pion-production threshold.

## 2.3 Fit to data

To assess the effects of adding energy dependence, we fit the parameters of our potential to the original  $np$  phase shift analysis of Arndt and MacGregor [5]. We could easily fit to more modern data sets, but then it would be difficult to assess whether the effects come from fitting to better data, or the energy dependence itself. We illustrate later in Fig. 2.10 that such a fit to more modern data is possible, although such a refit is beyond the scope of the present work.

### 2.3.1 Phase shift details

For uncoupled channels, we use the Lippmann-Schwinger Equation [24]:

$$\begin{aligned} \langle k\ell | \mathcal{T}^{JST}(k_0) | k'\ell' \rangle &= \langle k\ell | V^{JST} | k'\ell' \rangle \\ &+ \frac{m}{2\hbar^2} \sum_{\ell''} \int \frac{dq q^2}{(2\pi)^3} \langle k\ell | V^{JST} | q\ell'' \rangle \frac{1}{k_0^2 - q^2 + i\eta} \langle q\ell'' | \mathcal{T}_{pp}^{JST}(k_0) | k'\ell' \rangle. \end{aligned} \quad (2.39)$$

The on-shell value of  $\mathcal{T}$  is related to the phase shifts as follows:

$$\langle k_0\ell | \mathcal{S}^{JST}(k_0) | k_0\ell \rangle = \left[ 1 - 2\pi i \left( \frac{mk_0}{2\hbar^2} \right) \langle k_0\ell | \mathcal{T}^{JST}(k_0) | k_0\ell \rangle \right] \equiv e^{2i\delta_\ell^{JST}}, \quad (2.40)$$

and in practice we use

$$\tan \delta_\ell^{JST} = \frac{\text{Im} \langle k_0\ell | \mathcal{T}^{JST}(k_0) | k_0\ell \rangle}{\text{Re} \langle k_0\ell | \mathcal{T}^{JST}(k_0) | k_0\ell \rangle}. \quad (2.41)$$

For the coupled-channel Lippmann-Schwinger problem, we have non-diagonal  $\mathcal{S}$ -matrix elements given by:

$$\langle k_0\ell | \mathcal{S}^{JST}(k_0) | k_0\ell' \rangle = \left[ \delta_{\ell,\ell'} - 2\pi i \left( \frac{mk_0}{2\hbar^2} \right) \langle k_0\ell | \mathcal{T}^{JST}(k_0) | k_0\ell' \rangle \right], \quad (2.42)$$

where we can diagonalize the  $\mathcal{S}$ -matrix using the real matrix  $A$  with:

$$\langle k_0 \ell | \mathcal{S}^{JST}(k_0) | k_0 \ell' \rangle = \sum_{\alpha=1,2} \langle \ell | A^J(k_0) | \alpha \rangle e^{2i\delta_\alpha^{JST}} \langle \alpha | A^J(k_0) | \ell' \rangle. \quad (2.43)$$

$A$  is related to the mixing angle  $\epsilon_J$  as by

$$\langle \ell | A^J(k_0) | \alpha \rangle = \begin{pmatrix} \cos \epsilon^J & \sin \epsilon^J \\ -\sin \epsilon^J & \cos \epsilon^J \end{pmatrix}. \quad (2.44)$$

This mixing angle represents the amount that the  $L_1 = J - 1$  and  $L_2 = J + 1$  states mix in the wave functions of the scattered state. The terms  $\delta_\alpha^{JST}$  are referred to as *eigen phases*, and in practice these must be related to the more experimentally accessible *bar phases*. The relationships between these two quantities is given by [12]

$$\bar{\delta}_{L_1} + \bar{\delta}_{L_2} = \delta_{L_1} + \delta_{L_2} \quad (2.45)$$

$$\sin(\bar{\delta}_{L_1} - \bar{\delta}_{L_2}) = \frac{\tan 2\bar{\epsilon}_J}{\tan 2\epsilon_J} \quad (2.46)$$

$$\sin(\delta_{L_1} - \delta_{L_2}) = \frac{\sin 2\bar{\epsilon}_j}{\sin 2\epsilon_J}. \quad (2.47)$$

Since analyses of experimental data are usually framed in terms of bar phases, we transformed our eigen phases into bar phase to compare with the (bar) phase shift analysis of Arndt and MacGregor, to which Reid originally fit his soft-core potential.

## 2.4 Results

Table 2.1 compares the  $\chi^2/\text{datum}$  of our dynamic refit Dynamic Reid 1 (DR1 found in Appendix. A.2) to the partial-wave analysis of Arndt and MacGregor [5] and the original RSC potentials.

We were able to get  $\chi^2/\text{datum}$  similar and generally better than the RSC potential itself. We performed the fitting using a gradient search method, taking as our parameters the coefficients of the higher mass Yukawa terms in the RSC. Each single-channel partial wave was fitted separately, while for the coupled channels the  $J + 1$  and  $J - 1$  partial waves and mixing angle  $\epsilon_J$  were fit simultaneously. Plots

Table 2.1:  $\chi^2/\text{datum}$  for the RSC and DR1. The first set of six partial waves are the uncoupled channels which are fit independently. The two sets of partial waves at the bottom are coupled channels, and include the mixing angles  $\epsilon_J$ . Each set of coupled channels must be fit simultaneously, while with the  ${}^3S_1$  -  ${}^3D_1$  channel there is the additional constraint that one must find the proper binding energy for the deuteron.

Partial Wave	RSC	DR1
${}^1S_0$	2.31	0.94
${}^1P_1$	0.94	0.75
${}^1D_2$	0.76	0.72
${}^3P_0$	2.47	1.59
${}^3P_1$	1.83	0.90
${}^3D_2$	1.04	0.77
${}^3S_1$	0.50	1.00
${}^3D_1$	1.31	0.68
$\epsilon_1$	0.45	0.062
${}^3P_2$	2.90	0.70
${}^3F_2$	1.09	0.92
$\epsilon_2$	0.40	0.073

comparing our fit to Reid's and the original data are seen in Fig. 2.7 as well as in App. A.3.

In particular, for the deuteron channel ( ${}^3S_1 - {}^3D_1$ ) we had the additional requirement that we fit the deuteron binding energy. For this partial wave, after minimizing the  $\chi^2$  we found that our potential, when evaluated at the correct binding energy, yielded a slightly smaller binding energy. By making the potential slightly more attractive, it was easy to tune the potential to the correct binding energy  $E_b = -2.2246\text{MeV}$  while producing a negligible change to the  $\chi^2$ . In other words, fitting the phase shift in a natural way leads to the correct binding energy, as it should since the presence of the bound state is reflected in the phase shift. We should also point out that in the case of the deuteron, we varied only four (three central and one tensor) of the possible seven parameters to get our fit. No doubt we could have

varied more parameters to improve the fit, but we judged our  $\chi^2$  already sufficiently low and of similar quality to the RSC potential. When we fit this potential to modern data with smaller error bars there are more parameters available to vary to ensure a high quality fit. We do notice that our model, although fitting the same data, yields a significantly smaller  $D$ -state probability. In Fig. 2.8, we can see this reflected in the reduced amplitude of the wave functions, relative to those produced by the RSC. Deuteron data are tabulated below in Table 2.2. We can see how dynamical effects influence the long-range behavior of the pion by considering how the higher mass (static) terms of our potential must be modified to maintain a good fit to the scattering data. If we split the potential into a pion piece plus other terms (O.T.) as follows:  $V = V_{pi} + V_{O.T.}$ , we can look at how  $V_{O.T.}$  behaves in both the RSC and the DR1. In Fig. 2.9, we have plotted the  $V_{O.T.}$  for both the DR1 and the RSC, as well as the respective difference for the  ${}^3S_1$  partial wave. In this plot, we see that for the RSC, the  $V_{O.T.}$  is attractive at short range (not plotted) but becomes repulsive at long range, while for the DR1 it remains attractive at both long and short range. This indicates that in the RSC, the higher-mass terms serve to moderate the strength of the pion at long-range, while for the DR1 the dynamical effects provide this moderation in strength themselves. A similar trend is observed for the  ${}^1S_0$  channel, and we observe that fitting the potential to more modern data does not significantly affect the plot.

As we will demonstrate, our method is fairly successful at fitting more modern analyses such as the Partial Wave Analysis (PWA) of the Nijmegen group [60], so that

Table 2.2: Deuteron data for the RSC and DR1. A clear  $D$ -state probability reduction is observed, with minimal change to the  $S$ -state probability. The reduction in  $D$ -state probability almost perfectly corresponds to the probability of finding an  $NN\pi$  state.

Observable	RSC	DR1
$D$ -state Probability	6.47%	4.92%
$S$ -state Probability	93.53%	93.40%
$NN\pi$ Probability	0%	1.68%
Binding Energy	-2.2232	-2.2246

if the dynamic pion model can be shown to aid in understanding inelastic scattering and in medium effects, we could improve this model by including electromagnetic terms and fitting to proton-proton ( $pp$ ) data as well. For illustrative purposes only, we also provide below (Fig. 2.10) plots of the Dynamic Reid 2 (DR2) refit to the PWA for the isovector  $np$  data. Larger plots are available for comparison in App. A.4. No error bars are provided with these PWA numbers, so we cannot quote a  $\chi^2$  but we can qualitatively show that a reasonable fit is attainable. This fit to more modern data should allow us in the future to assess how much of the success of our dynamic model with inelastic scattering data is due to the addition of energy dependence, and how much is due to the quality of data to which the potential has been fit.

### 2.4.1 Off-shell $\mathcal{T}$ -matrix

Also noteworthy to point out are the effects of the inclusion of energy dependence on the off-shell  $\mathcal{T}$ -matrix elements. As we can see in Fig. 2.11, The energy dependence slightly suppresses both the real and imaginary parts of the  $\mathcal{T}$ -matrix at low energy. As the energy increases, the discrepancy between the imaginary parts of both static and dynamic potentials is minimal, but the real part suffers drastic changes and gains a double cusp-like structure at higher energies, as seen in Fig. 2.12. This structure corresponds to the double cusp-like structure in the potential, which has been smoothed out by the inclusion of a 5 MeV pion width. This altered  $\mathcal{T}$ -matrix will be shown in Chapter 3 to have some consequences, however slight, in understanding inelastic  $pp$  scattering experiments.

## 2.5 Conclusions and discussion

We see that modifying the RSC to include dynamic pions is not only possible but can be done with a minimal changing of the original parameters. We have offered a prescription that would allow the modification of any modern static interaction to allow dynamic propagation of pions. One of the consequences of replacing static pions with their dynamic counterparts is a reduced  $D$ -state probability for the deuteron,

accompanied by a small but non-negligible  $NN\pi$  component. We also see a significant difference between the static and dynamic  $\mathcal{T}$ -matrices off-shell, which begs an examination of scenarios where off-shell elements might be influential. Our potential DR1 will allow us in the chapters to come to assess the importance and consequences of dynamic pion propagation in a variety of contexts, beginning with inelastic  $(p, 2p)$  scattering from light nuclei (Ch. 3), and concluding with Brueckner-Hartree-Fock nuclear-matter calculations (Ch. 4).

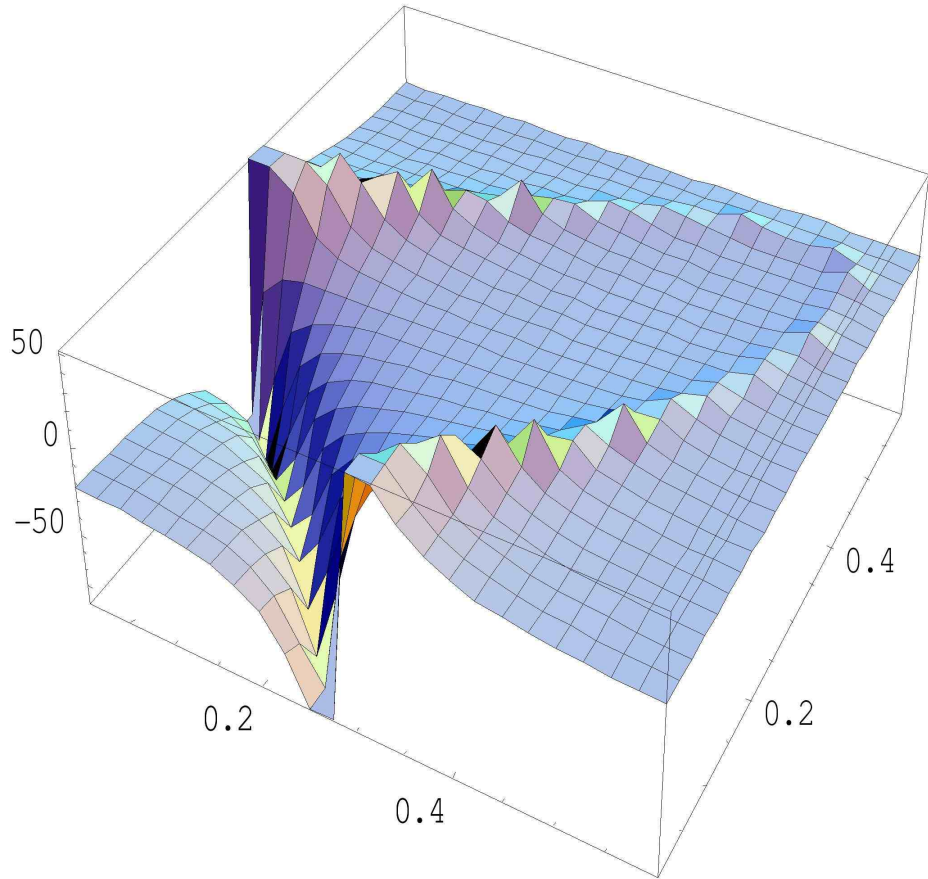


Figure 2.6: Plot of  $\tilde{Q}_{\ell=0}(k, k', 300 \text{ MeV})$ . The cusp like structures enclose a parabolic region that moves away from the origin with increasing energy. This structure is very sharp and difficult to integrate across numerically. Note that the jaggedness of edges is an artifact of the plotting software.



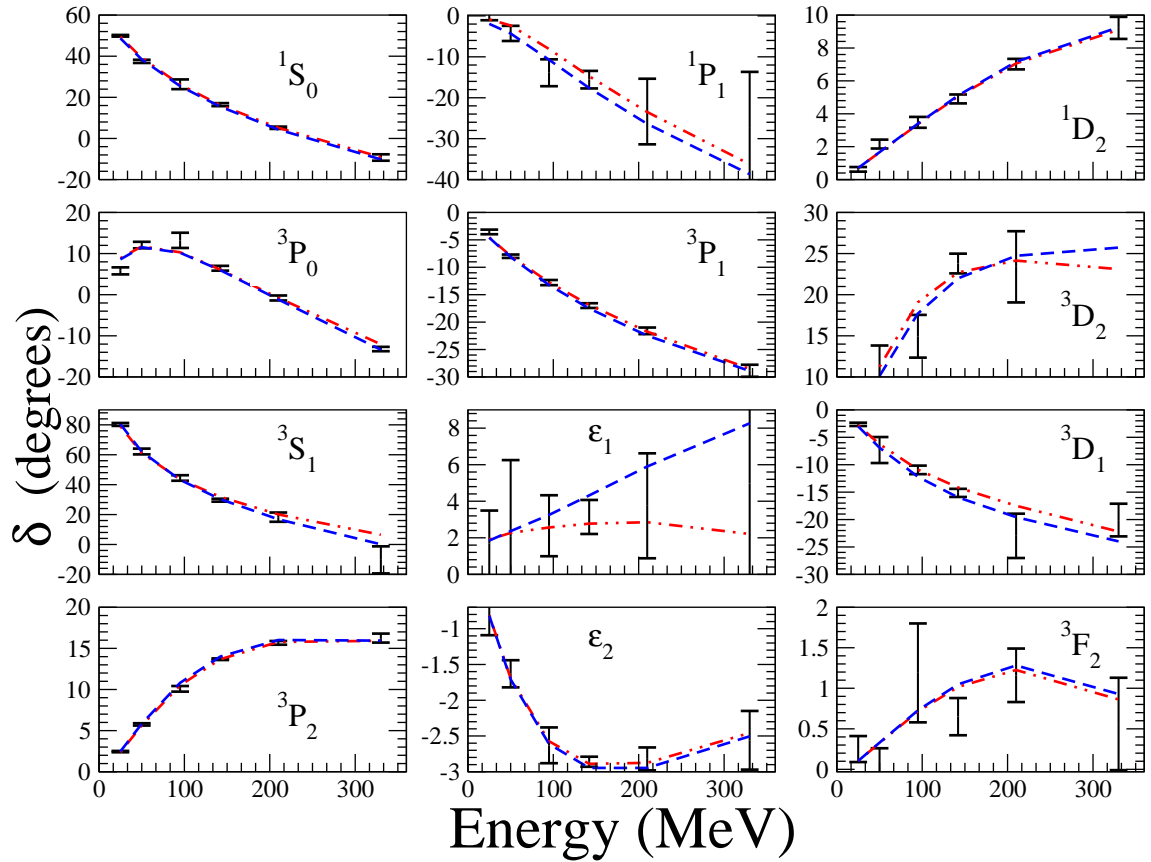


Figure 2.7: Plot of RSC and DR1 phase shifts and mixing angles. Black error bars are from the original analysis of Arndt and MacGregor [5]. Dashed (blue) curve is Reid's fit. Red dash-dot-dotted line is the DR1 refit.

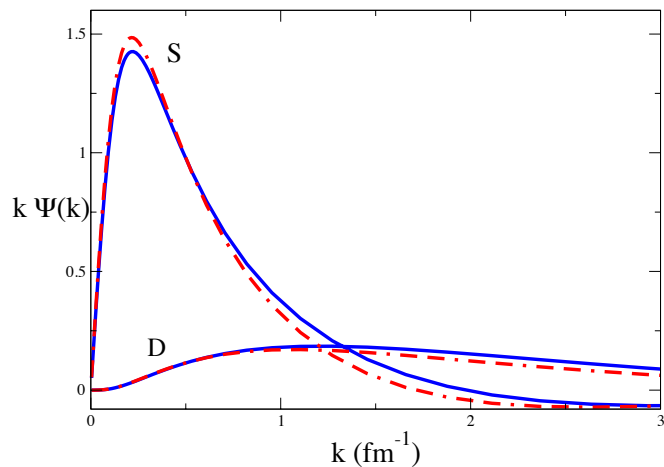


Figure 2.8:  $k$ -space wave-functions multiplied by  $k$  for the deuteron. Solid blue curves are RSC wave functions, while dash-dash-dotted red curves are those of the DR1. The latter have been normalized to  $1 - P(NN\pi)$ .

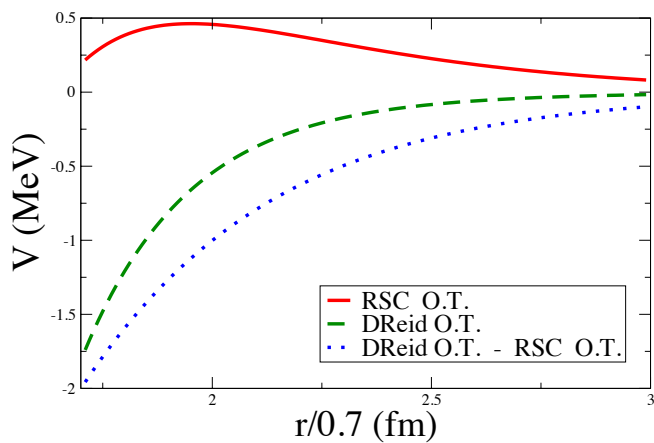


Figure 2.9: Plot of central part of  $V_{O,T}$  for the  ${}^3S_1$  channel. Solid (red) curve is for RSC. Dashed (green) is for DR1, and dotted (blue) is of the difference  $(V_{O,T.-DR1}) - (V_{O,T.-RSC})$ .

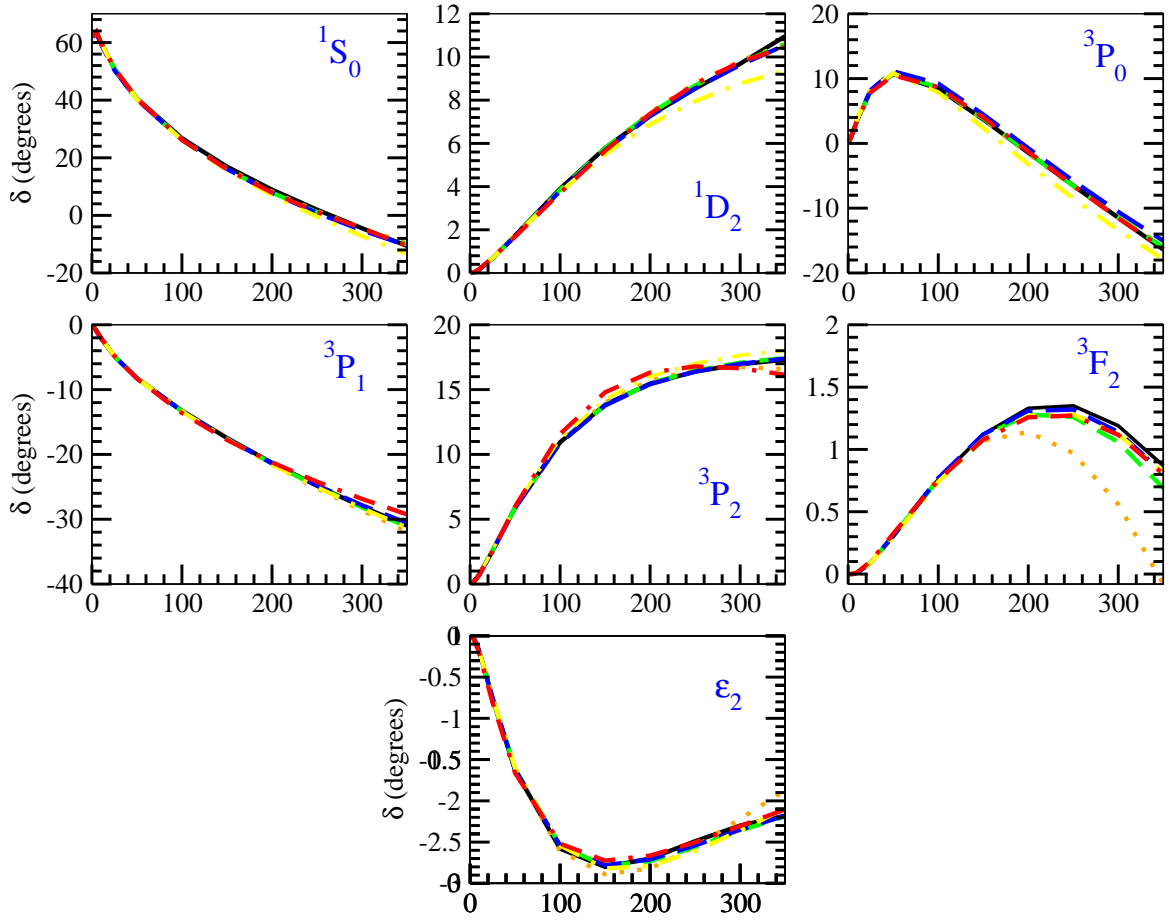


Figure 2.10: Plot of DR2 fit to partial-wave analysis isovector phase shifts and mixing angle. Solid black lines are the PWA. DR2 is represented by red dashed lines, while the other curves for comparison are Nijm 1 (orange dots), Nijm 2 (green dashes), Reid 93 (blue long dashes), and Nijm 93 (yellow dash-dots).

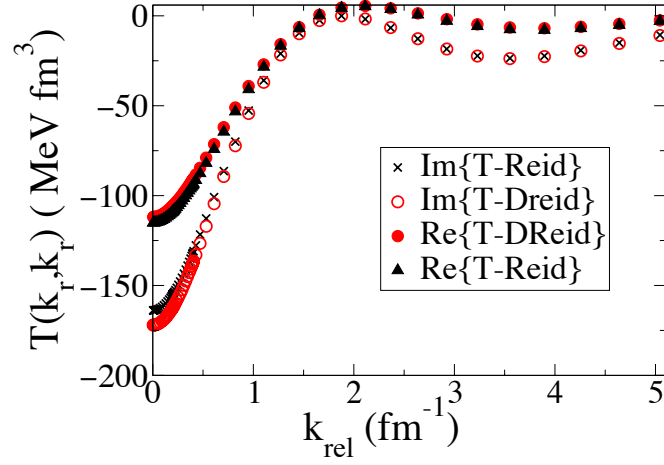


Figure 2.11:  $\mathcal{T}$ -matrix elements for RSC and DR1 calculated at an energy of 1 MeV (Lab).

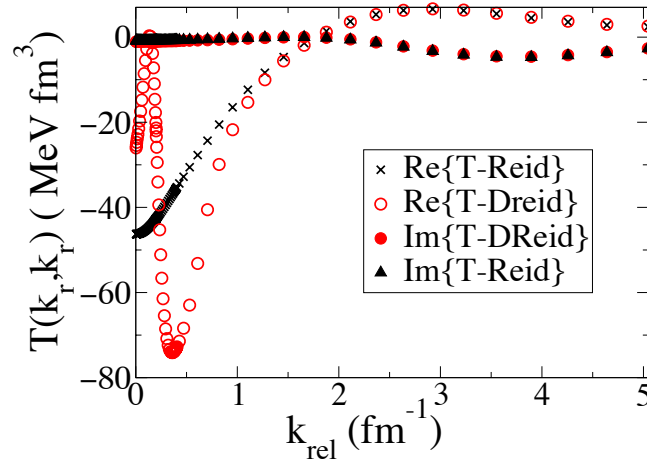


Figure 2.12:  $\mathcal{T}$ -matrix elements for RSC and DR1 calculated at an energy of 300 MeV (Lab).

# Chapter 3

## Inelastic Scattering

### 3.1 Two-body $A_y$ puzzle

The dynamic potential detailed in Ch. 2 necessarily agrees on-shell with the RSC and any other phase-shift equivalent potentials. Therefore any consequences of using the dynamic interaction must be seen in experimental arrangements that are sensitive to off-shell  $\mathcal{T}$ -matrix elements. Probably the simplest such experimental set-up is inelastic ( $pp$ ) scattering. One such project [49] involves a series of direct ( $p, 2p$ ) experiments in which the polarization variable  $A_y$  has been measured for proton-induced proton knock-out for a wide range of light nuclei. Due to the binding energies of the removed protons, these experiments are necessarily inelastic and should therefore probe off-shell aspects of the  $\mathcal{T}$ -matrix. Interestingly, a puzzle has arisen for this set of experiments. Compared to free  $pp$  scattering it seems that  $A_y$  is reduced by increasing amounts as the size of the target nucleus increases. So far, attempts at explaining this reduction using experimental (on-shell)  $NN$   $\mathcal{T}$ -matrix elements have been unsatisfactory. In this chapter we will first give an overview of this new two-body  $A_y$  puzzle, and why we think that a dynamic  $NN$  interaction might be better suited for understanding these experiments.

$A_y$  is the difference between y-direction spin up and spin down differential cross section measurements normalized by total differential cross section. It is defined by

$$A_y = \frac{\sigma_y(\uparrow) - \sigma_y(\downarrow)}{\sigma_y(\uparrow) + \sigma_y(\downarrow)}. \quad (3.1)$$

In a series of direct  $1s_{1/2}$  (where the principle quantum number starts with 1) proton knockout measurements at the Research Center for Nuclear Physics (RCNP) of Osaka University,  $A_y$  was measured for a variety of nuclei with fixed proton beam energy of  $E_{lab} = 392$  MeV. Incoming spin was polarized, and outgoing protons were detected using two spectrometers. The Grand Raiden (GR) spectrometer was held at a fixed angle of 25.5 degrees, while the Large Acceptance Spectrometer (LAS) was placed at angles which were varied to control the kinematics. By controlling the angle of the LAS, the collisions were chosen such that the remaining nucleus did not recoil. These measurements showed a reduction of  $A_y$  relative to free proton-proton scattering. For many nuclei, this reduction in  $A_y$  seemed (Fig. 3.1) to correlate to effective mean density. However,  ${}^3\text{He}$  and  ${}^4\text{He}$  did not fit this trend. In the second panel of Fig. 3.1 we see  $A_y$  plotted versus  $1s_{1/2}$  removal energy  $E_s$ , and see a much clearer trend. Attempts have been made to explain and model this reduction in  $A_y$  using both the plane-wave impulse approximation (PWIA) and the distorted-wave impulse approximation (DWIA), but both of these methods utilize experimental (on-shell)  $NN$   $\mathcal{T}$ -matrix elements. However, the kinematics are such that there is explicit energy transfer, and so we maintain that it is more appropriate to use a dynamic interaction like that detailed in Ch. 2 to describe these data. An example of the magnitude of energy that can be transferred in these experiments can be seen in Table 3.1. In the case of  ${}^{12}\text{C}$  there is an energy transfer of 124 MeV (direct) or 304 MeV (exchange) in the lab frame. Because these amounts are non-negligible, it is appropriate to explore the construction of an inelastic  $\mathcal{T}$ -matrix using the dynamic potential DR1 in the PWIA so that this energy transfer can be explicitly built in from the beginning. Distorted-wave effects will not be considered in the present work.

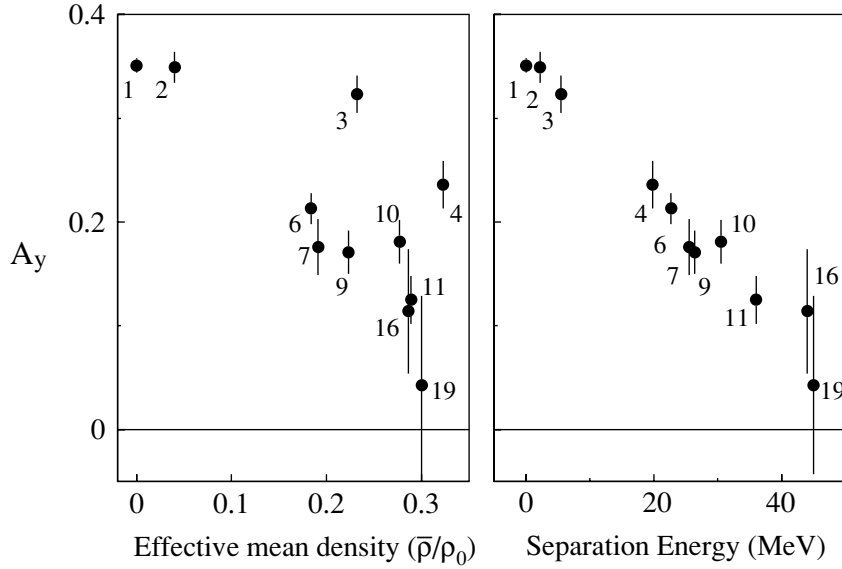


Figure 3.1:  $A_y$  for a series of direct  $1s_{1/2}$  removal (p,2p) reactions versus effective mean density(left) and separation energy (right). Numbers indicate nucleon number A. Figure taken from [49].

## 3.2 Computation of $A_y$

In this section we first provide the details of the standard treatment for computing  $A_y$  using a partial-wave basis. Our approach differs from the standard one in that we use  $\mathcal{T}$ -matrix elements generated from our dynamic potential, rather than experimentally determined (on-shell)  $\mathcal{T}$ -matrix elements. Additionally, because we generate the full  $\mathcal{T}$ -matrix, we can use the appropriate off-shell element based on experimental kinematics. Using as our basis states  $|\mathbf{p}_1 s_1 m_{s_1} \tau_1 m_{\tau_1}; \mathbf{p}_2 s_2 m_{s_2} \tau_2 m_{\tau_2}\rangle$  with all spins in the z-direction, we define *e.g.*  $\sigma_y(\uparrow)$  as given by Eq. (3.1) as follows.

$$\sigma_y(\uparrow) = \sum_{\substack{m_{s_2} m'_{s_1} \\ m'_{s_2}}} \frac{1}{2} \left| \langle \mathbf{p}_1 \frac{1}{2} \uparrow_y \tau_1 m_{\tau_1}; \mathbf{p}_2 \frac{1}{2} m_{s_2} \tau_2 m_{\tau_2} | \mathcal{T} | \mathbf{p}'_1 \frac{1}{2} m'_{s_1} \tau'_1 m'_{\tau_1}; \mathbf{p}'_2 \frac{1}{2} m'_{s_2} \tau'_2 m'_{\tau_2} \rangle \right|^2 \quad (3.2)$$

Table 3.1: Kinematics for direct recoilless  $1s_{1/2}$  removal in  $^{12}\text{C}$  ( $p, 2p$ ) where  $E_p$  denotes beam energy and  $E_{p'}$ ,  $E_{p''}$ , and  $E_\alpha$  denote respectively the two outgoing proton energies, and the energy of the excited hole-state.

Quantity	Lab Energy (MeV)
$E_p$	392
$E_{p'}$	268
$E_{p''}$	88
$E_\alpha$	-36

where in the preceding the spin projections  $m'_{s_1}$ ,  $m_{s_2}$ , and  $m'_{s_2}$  are eigenstates of the z-direction spin operator  $s_z$  and

$$|\uparrow_y\rangle = \frac{1}{\sqrt{2}}(|\uparrow_z\rangle + i|\downarrow_z\rangle), \quad (3.3)$$

with a similar expression for  $\sigma_y(\downarrow)$ . The task then becomes to compute  $\mathcal{T}$ -matrix elements of the form (suppressing the proton spins  $s_1$  and  $s_2$  and isospins  $\tau_1$  and  $\tau_2$ ):

$$|\langle \mathbf{p}_1 m_{s_1} m_{\tau_1}; \mathbf{p}_2 m_{s_2} m_{\tau_2} | \mathcal{T} | \mathbf{p}'_1 m'_{s_1} m'_{\tau_1}; \mathbf{p}'_2 m'_{s_2} m'_{\tau_2} \rangle|^2. \quad (3.4)$$

We can use the following expansion [24]

$$\begin{aligned} |\mathbf{p}_1 m_{s_1} m_{\tau_1}; \mathbf{p}_2 m_{s_2} m_{\tau_2}\rangle = & \\ & \frac{1}{\sqrt{2}} \sum_{\substack{SM_S TM_T \\ LM_L JM_J}} (\frac{1}{2} m_{s_1} \frac{1}{2} m_{s_2} | SM_S) (\frac{1}{2} m_{\tau_1} \frac{1}{2} m_{\tau_2} | TM_T) Y_{LM_L}^*(\hat{\mathbf{k}}) \\ & (LM_L SM_S | JM_J) (1 - (-1)^{L+S+T}) | \mathbf{P}\mathbf{p}(LS) JM_J TM_T \rangle \end{aligned} \quad (3.5)$$

to express the  $\mathcal{T}$ -matrix in the partial-wave basis. We can further simplify by noting that for each partial wave, the  $\mathcal{T}$ -matrix is proportional to  $\delta_{J,J'} \delta_{M_J, M'_J} \delta_{S, S'}$ . In addition, we recall that in the present chapter we are interested only in proton-proton scattering and so consider only  $T = 1$  channels. All of the isospin Clebsch-Gordon



coefficients are therefore equal to unity, and we may suppress them with no loss of generality. Taking  $\hat{\mathbf{p}} = \hat{\mathbf{z}}$  where  $\mathbf{p} = \frac{1}{2}(\mathbf{p}_1 - \mathbf{p}_2)$  is the relative momentum, we can also simplify the spherical harmonics that will appear in our final expression for each partial wave. The  $\mathcal{T}$ -matrix contribution is given by

$$\begin{aligned} \mathcal{T}_z(m_{s1}) = \frac{1}{2} \sum_{\substack{m_{s2} m'_{s1} \\ m'_{s2}}} \sum_{\substack{L, J \\ L', S}} \sum_{\substack{M_S M_{S'} \\ M_L M_{L'}}} (\frac{1}{2} m_{s1} \frac{1}{2} m_{s2} | S M_S) (\frac{1}{2} m'_{s1} \frac{1}{2} m'_{s2} | S M'_S) \\ (L M_L S M_S | J M_J) (L' 0 S M'_S | J M_J) Y_{L'0}^*(\hat{\mathbf{z}}) Y_{L M_L}(\theta, \phi) \\ \mathcal{T}_{\mathcal{L}, \mathcal{J}, \mathcal{S}} (1 - (-1)^{L+S+T}) (1 - (-1)^{L'+S+T}) i^{(L-L')}. \end{aligned} \quad (3.6)$$

In the preceding formula, the phase  $i^{(L-L')}$  comes from a convention for our definition of  $\mathcal{T}$ . This expression for  $\mathcal{T}_z(m_{s1})$  can be further simplified using the properties of the Clebsch-Gordon coefficients. The third and fourth such coefficients indicate  $M_L = M'_S - M_S$ . In addition, since the tensor force can only change the angular momentum  $L$  by 2, the antisymmetry factors  $(1 - (-1)^{L+S+T})(1 - (-1)^{L'+S+T})$  both contain either odd or even exponents for a given channel and we can reduce their number by squaring one of them and removing the other, yielding

$$\begin{aligned} \mathcal{T}_z(m_{s1}) = \frac{1}{2} \sum_{\substack{m_{s2} m'_{s1} \\ m'_{s2}}} \sum_{\substack{L, J \\ L', S}} \sum_{\substack{M_S M_{S'} \\ M_L}} (\frac{1}{2} m_{s1} \frac{1}{2} m_{s2} | S M_S) (\frac{1}{2} m'_{s1} \frac{1}{2} m'_{s2} | S M'_S) \\ (L(M'_S - M_S) S M_S | J M_J) (L' 0 S M'_S | J M_J) Y_{L'0}^*(\hat{\mathbf{z}}) \\ Y_{L(M'_S - M_S)}(\theta, \phi) \mathcal{T}_{\mathcal{L}, \mathcal{J}, \mathcal{S}} (1 - (-1)^{L+S+T})^2 i^{(L-L')}. \end{aligned} \quad (3.7)$$

Now that we have an expression for differential cross section in the  $z$ -direction, we can easily obtain an expression for  $\sigma_y$  using the following expressions that result from

Eq. (3.3) and inserting them into Eq. (3.2)

$$\mathcal{T}_y(\uparrow) = \frac{1}{\sqrt{2}}(\mathcal{T}_z(\uparrow) + i\mathcal{T}_z(\uparrow)) \quad (3.8)$$

$$\mathcal{T}_y(\uparrow) = \frac{1}{\sqrt{2}}(\mathcal{T}_z(\uparrow) - i\mathcal{T}_z(\uparrow)). \quad (3.9)$$

Traditionally [49] this strategy is employed using the on-shell values of the  $\mathcal{T}$ -matrix generated by solving the Lippman-Schwinger equation for free proton-proton scattering [Eqs. (2.41) and (2.42)], or using the on-shell  $\mathcal{T}$ -matrix elements generated by phase-shift analyses of experimental elastic proton-proton scattering data. However, these on-shell elements are not entirely appropriate since some energy is explicitly transferred to the nucleus in these experiments. Furthermore, this  $\mathcal{T}$ -matrix is generated by summing ladder diagrams that are more appropriate for elastic proton-proton scattering than for an inelastic  $(p, 2p)$  process. A more appropriate strategy for modeling this type of experiment is discussed in subsection 3.3.

### 3.3 Inelastic $\mathcal{T}$ -matrix

We construct an inelastic scattering  $\mathcal{T}$ -matrix for a single incoming particle and an outgoing two-particle one-hole  $(2p1h)$  state as seen in Fig. 3.2. This diagrammatic equation involves two different  $\mathcal{T}$ -matrices. The  $\mathcal{T}$ -matrix on the left (yellow box) is the inelastic  $\mathcal{T}$ -matrix which represents the full ladder summation for a  $(p, 2p)$  process

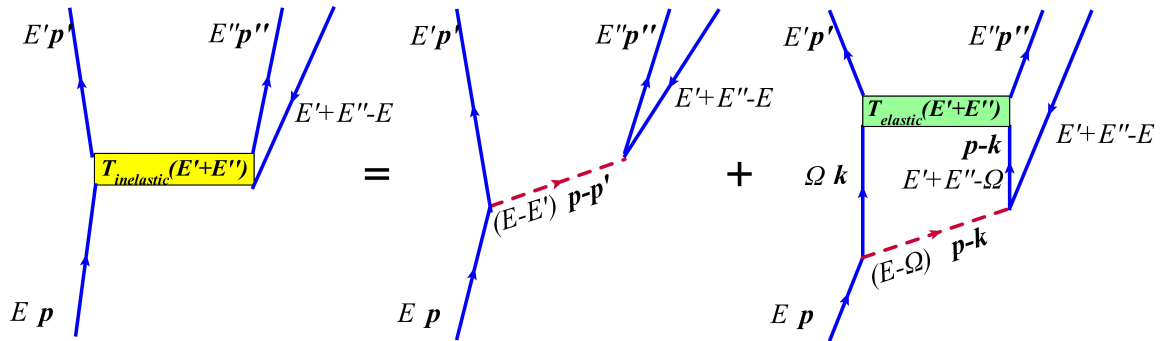


Figure 3.2: Full inelastic  $\mathcal{T}$ -matrix diagram for inelastic  $(p, 2p)$  process.

where a free nucleon enters a nucleus and two nucleons emerge. We will see during this discussion that there is an explicit dependence upon separation energy  $E_s = -E_\alpha$  where  $E_\alpha$  is the energy of the excited hole. It is this dependence that could shed some light on the  $E_s$  dependence observed in  $A_y$  for these inelastic knockout experiments. The  $\mathcal{T}$ -matrix in the second term on the right (green box) is the full elastic  $\mathcal{T}$ -matrix generated as described in chapter 2, but with a reduction in energy at which it is evaluated by an amount equal to the separation energy, as we shall see when we evaluate the integration over external and loop energies. Evaluation of the integral equation for the inelastic  $\mathcal{T}$ -matrix involves evaluating both terms on the right hand side of the diagram separately. We wish to get a sense of how the pion behaves when it is allowed to transfer energy in an inelastic  $(p, 2p)$  process, so will begin by evaluating the lowest order term.

### 3.3.1 Lowest-order inelastic $(p, 2p)$

This lowest-order process is depicted in Fig. 3.3 including the relevant energies and momenta. The relevant propagator for this process is given by

$$\begin{aligned} \tilde{I}_\pi(\mathbf{p}, \mathbf{p}', \mathbf{p}'', \alpha; E) &= \int \frac{dE'}{2\pi i} \int \frac{dE''}{2\pi i} G^{(0)}(\mathbf{p}; E) \\ &\times D^\pi(\mathbf{p} - \mathbf{p}'; E - E') G^{(0)}(\mathbf{p}'; E') G^{(0)}(\mathbf{p}''; E'') G^{(0)}(\alpha; E' + E'' - E), \end{aligned} \quad (3.10)$$

where

$$G^{(0)}(\alpha; E) = \frac{\theta(F - \alpha)}{E - E_\alpha - i\eta} \quad (3.11)$$

represents the propagation of a hole, signified by the step function, in the single-particle ( $sp$ ) state  $\alpha$ . For simplicity we assume that the energies of the projectile and detected protons are sufficiently high that nonorthogonality with the  $sp$  state  $\alpha$  is irrelevant. The energy integrations in Eq. (3.10) can be performed as for Eq. (2.5)

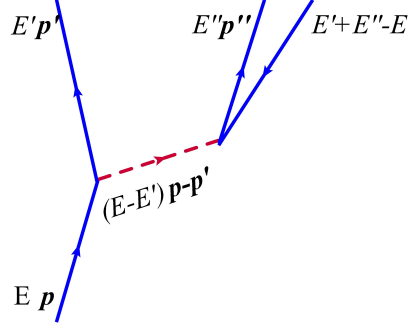


Figure 3.3: Lowest-order pion-exchange contribution to the proton induced proton knockout process  $(p, 2p)$ .

with result

$$\begin{aligned} \tilde{I}_\pi(\mathbf{p}, \mathbf{p}', \mathbf{p}'', \alpha; E) = & \quad (3.12) \\ G_f^{(0)}(\mathbf{p}', \mathbf{p}'', \alpha; E) \frac{1}{2\varepsilon^\pi(|\mathbf{p} - \mathbf{p}'|)} \frac{1}{E - \varepsilon(\mathbf{p}') - \varepsilon^\pi(|\mathbf{p} - \mathbf{p}'|) + i\eta} G_i^{(0)}(\mathbf{p}; E) \\ + G_f^{(0)}(\mathbf{p}', \mathbf{p}'', \alpha; E) \frac{1}{2\varepsilon^\pi(|\mathbf{p} - \mathbf{p}'|)} \frac{1}{E_\alpha - \varepsilon(\mathbf{p}'') - \varepsilon^\pi(|\mathbf{p} - \mathbf{p}'|) + i\eta} G_i^{(0)}(\mathbf{p}; E), \end{aligned}$$

where

$$G_f^{(0)}(\mathbf{p}', \mathbf{p}'', \alpha; E) = \frac{1}{E - \varepsilon(\mathbf{p}') - \varepsilon(\mathbf{p}'') + E_\alpha + i\eta} \quad (3.13)$$

represents the final state propagator and

$$G_i^{(0)}(\mathbf{p}; E) = \frac{1}{E - \varepsilon(\mathbf{p}) + i\eta} \quad (3.14)$$

the propagator for the initial projectile. The two resulting terms are depicted graphically as time-ordered contributions in Fig. 3.4. For future convenience, we define

these two time-ordered terms as the  $(p, 2p)$  pion propagator

$$G_{\pi}^{(0)}(p, 2p)(\mathbf{p}, \mathbf{p}', \alpha; E) \equiv \frac{1}{2\varepsilon^{\pi}(|\mathbf{p} - \mathbf{p}'|)} \quad (3.15)$$

$$\times \left( \frac{1}{E - \varepsilon(\mathbf{p}') - \varepsilon^{\pi}(|\mathbf{p} - \mathbf{p}'|) + i\eta} + \frac{1}{E_{\alpha} - \varepsilon(\mathbf{p}'') - \varepsilon^{\pi}(|\mathbf{p} - \mathbf{p}'|) + i\eta} \right)$$

and we can rewrite Eq. (3.12) as

$$\tilde{I}_{\pi}(\mathbf{p}, \mathbf{p}', \mathbf{p}'', \alpha; E) = G_f^{(0)}(\mathbf{p}', \mathbf{p}'', \alpha; E) G_{\pi}^{(0)}(p, 2p)(\mathbf{p}, \mathbf{p}', \alpha; E) G_i^{(0)}(\mathbf{p}; E). \quad (3.16)$$

We now recognize that a very different situation occurs compared to elastic  $NN$  scattering when the experimental conditions of the  $(p, 2p)$  reaction of Refs. [48, 34] are considered. In particular, in the first term of Eq. (3.12) the pion can now transfer a particularly large amount of energy, while there is an explicit removal energy dependence (expressed by  $E_{\alpha}$ ) in the second term where the pion is completely virtual. This simple analysis therefore clarifies that the use of the free  $NN$   $\mathcal{T}$ -matrix for quasi-free  $(p, 2p)$  reactions is not appropriate and the energy dependence of the interaction represented by pion-exchange should be explicitly considered. This observation provided an important motivation for the construction of a dynamic pion-exchange interaction that can properly treat the energy dependence of inelastic processes. The example discussed here also clarifies that an explicit removal energy dependence of the knockout process can be expected. As discussed previously, such a dependence appears to be observed in the polarization observable  $A_y$  for the removal of  $s_{1/2}$  protons [48].

### 3.3.2 Higher-order inelastic $(p, 2p)$

Now we can turn our attention to the second diagram on the RHS of Fig. 3.2. We include this diagram with the relevant momenta and energy in Fig. 3.5. This contribution to the full inelastic  $\mathcal{T}$ -matrix can be computed by integrating over external

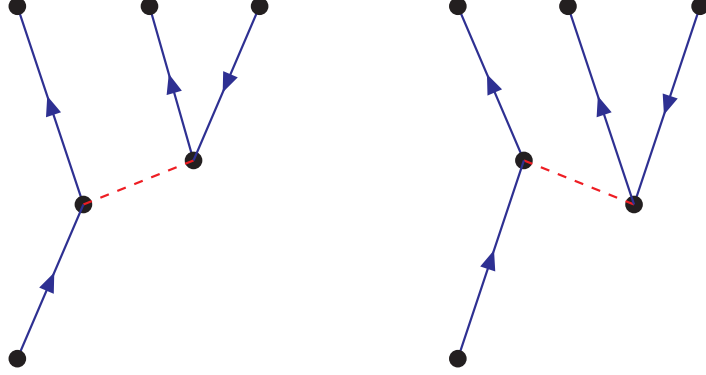


Figure 3.4: Lowest-order pion-exchange contribution to the proton induced proton knockout process as time-ordered terms representing Eq. (3.12).

and loop energies (suppressing spin and isospin)

$$\begin{aligned}
\tilde{I}_\pi(\mathbf{p}, \mathbf{p}', \mathbf{p}'', \mathbf{k}, \alpha; E) &= \int \frac{d\Omega}{2\pi i} \int \frac{dE'}{2\pi i} \int \frac{dE''}{2\pi i} G^{(0)}(\mathbf{p}; E) D^\pi(\mathbf{p} - \mathbf{k}; E - \Omega) \\
&\times G^{(0)}(\mathbf{k}; \Omega) G^{(0)}(\mathbf{p} - \mathbf{k}; E' + E'' - \Omega) \langle \mathbf{k} - \mathbf{p}/2 | \mathcal{T}(E' + E'') | \frac{1}{2}(\mathbf{p}' - \mathbf{p}'') \rangle \\
&\times G^{(0)}(\mathbf{p}'; E') G^{(0)}(\mathbf{p}''; E'') G^{(0)}(\alpha; E' + E'' - E).
\end{aligned} \tag{3.17}$$

This integral can be evaluated by first performing the  $dE''$  integral and closing in the lower half plane, then closing the  $dE'$  integral in the upper half plane, leaving only the  $d\Omega$  integral in the following form:

$$\begin{aligned}
\tilde{I}_\pi(\mathbf{p}, \mathbf{p}', \mathbf{p}'', \mathbf{k}, \alpha; E) &= \\
&G^{(0)}(\mathbf{p}; E) G^{(0)}(\mathbf{k} - \mathbf{p}'; E + E_\alpha) \langle \mathbf{k} - \mathbf{p}/2 | \mathcal{T}(E + E_\alpha) | \frac{1}{2}(\mathbf{p}' - \mathbf{p}'') \rangle \\
&\times \int \frac{d\Omega}{2\pi i} G^{(0)}(\mathbf{p} - \mathbf{k}; \Omega - E - E_\alpha) G^{(0)}(\mathbf{k}; \Omega) \frac{1}{2\varepsilon^\pi(|\mathbf{p} - \mathbf{k}|)} \\
&\times \left( \frac{1}{\Omega - E + \varepsilon^\pi(|\mathbf{p} - \mathbf{k}|) - i\eta} - \frac{1}{\Omega - E - \varepsilon^\pi(|\mathbf{p} - \mathbf{k}|) + i\eta} \right)
\end{aligned} \tag{3.18}$$

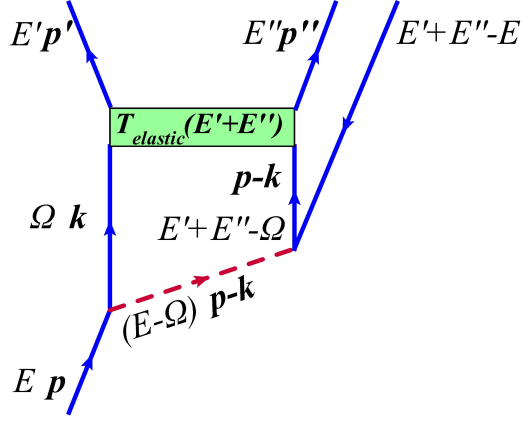


Figure 3.5: Higher-order contribution to inelastic  $\mathcal{T}$ -matrix diagram for  $(p, 2p)$

Now, closing the contour for the first term in the lower half plane, and the second term in the upper half plane, we have finally,

$$\begin{aligned} \tilde{I}_\pi(\mathbf{p}, \mathbf{p}', \mathbf{p}'', \mathbf{k}, \alpha; E) = & \quad (3.19) \\ & G_i^{(0)}(\mathbf{p}; E) \langle \mathbf{k} - \mathbf{p}/2 | \mathcal{T}(E + E_\alpha) | \frac{1}{2}(\mathbf{p}' - \mathbf{p}'') \rangle G_f^{(0)}(\mathbf{p}, \mathbf{p}'; E + E_\alpha) \\ & \times \frac{1}{E + E_\alpha - \varepsilon(|\mathbf{p} - \mathbf{k}|) - \varepsilon(\mathbf{k}) + i\eta} G_{\pi(p, 2p)}^{(0)}(\mathbf{p}, \mathbf{k}, \alpha; E). \end{aligned}$$

Here we see that this propagator is a function of beam energy  $E$  and both incoming nucleon momentum and outgoing momenta. The  $\mathcal{T}$ -matrix

$$\langle \mathbf{k} - \mathbf{p}/2 | \mathcal{T}(E + E_\alpha) | \frac{1}{2}(\mathbf{p}' - \mathbf{p}'') \rangle$$

is precisely the elastic (dynamic + static terms)  $\mathcal{T}$ -matrix that we discussed in Ch. 2, with its energy shifted by minus the separation energy ( $-E_s = E_\alpha$ ) since  $E' + E'' = E + E_\alpha$  by energy conservation. The internal momentum variable  $\mathbf{k}$  must still be integrated over in order to fully evaluate the diagram, but this integration cannot be done analytically due to the numerical construction of the  $\mathcal{T}$ -matrix.

Before further clarifying this momentum integral, it is important to stress that although these diagrams seem pictorially to include only dynamic pion-exchange in

the dashed lines, these terms must be understood to represent an interaction that contains a dynamic pion plus additional phenomenological higher-mass meson-exchange terms which are purely static in character. The elastic  $\mathcal{T}$ -matrix which appears in Fig. 3.5 has also been constructed with both dynamic pion terms and static higher-mass terms.

For the evaluation of this integral in the partial-wave basis, we find it more convenient at this stage to reparametrize the loop momenta in such a way that angles which occur in the pion propagator are the same angles we have previously introduced. This allows us to use a strategy similar to the one used for elastic scattering (sec. 2.2.3) to express our states in a partial-wave expansion. This reparametrization can be seen in Fig. 3.6.

By reparametrizing in this way, we make sure that the angle which occurs in the inelastic tree-level structure between  $\mathbf{p}_0/2$  and  $\mathbf{k}$  is also the angle between relative momentum of the beam ( $\mathbf{k}_1$ ) and the intermediate two particle propagator ( $\mathbf{k}_2$ ) where

$$\begin{aligned}\mathbf{k}_1 &= \frac{\mathbf{p}_0}{2} \\ \mathbf{k}_2 &= \mathbf{k}.\end{aligned}\tag{3.20}$$

This complication comes from the fact that it is generally convenient to compute the  $\mathcal{T}$ -matrix in terms of relative momenta, but we wish to easily be able to connect with the external variables which are provided by the relativistic kinematics of the experiment in question. The integral over  $\mathbf{k}$  now reads:

$$\begin{aligned}&\frac{1}{2} \int \frac{d^3k}{(2\pi)^3} \langle \mathbf{p}', \mathbf{p}'' | \mathcal{T}_{elastic}(E + E_\alpha) | \frac{\mathbf{p}_0}{2} + \mathbf{k}, \frac{\mathbf{p}_0}{2} - \mathbf{k} \rangle \\ &\quad \times \frac{1}{E + E_\alpha - \varepsilon(\frac{\mathbf{p}_0}{2} + \mathbf{k}) - \varepsilon(\frac{\mathbf{p}_0}{2} - \mathbf{k})} \\ &\quad \times \langle \frac{\mathbf{p}_0}{2} - \mathbf{k}, \frac{\mathbf{p}_0}{2} + \mathbf{k} | \tilde{V}_\pi(E, E_\alpha) + \Delta V | \mathbf{p}_0, \alpha \rangle\end{aligned}\tag{3.21}$$



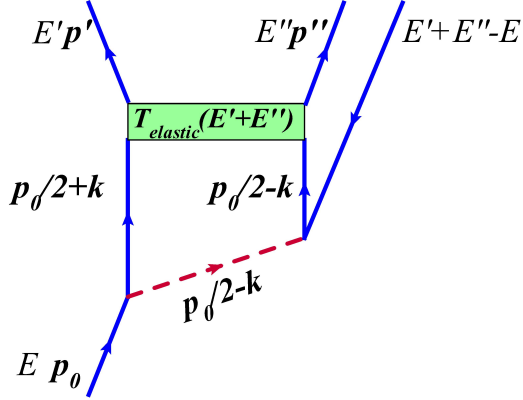


Figure 3.6: Higher-order inelastic  $\mathcal{T}$ -matrix diagram with momenta reparametrized and energy  $\Omega$  already integrated out. Both the elastic  $\mathcal{T}$ -matrix and the  $(p, 2p)$  interaction should be understood to include both static and dynamic terms.

where

$$\begin{aligned} \langle \frac{\mathbf{p}_0}{2} - \mathbf{k}, \frac{\mathbf{p}_0}{2} + \mathbf{k} | \tilde{V}_\pi(E, E_\alpha) | \mathbf{p}_0, \alpha \rangle &= \frac{1}{2\varepsilon^\pi(|\frac{\mathbf{p}_0}{2} + \mathbf{k}|)} \times \\ &\left( \frac{V_\pi^{O.P.}}{E - \varepsilon(|\frac{\mathbf{p}_0}{2} + \mathbf{k}|) - \varepsilon^\pi(|\frac{\mathbf{p}_0}{2} - \mathbf{k}|) + i\eta} \right. \\ &\quad \left. + \frac{V_\pi^{O.P.}}{E_\alpha - \varepsilon(|\frac{\mathbf{p}_0}{2} - \mathbf{k}|) - \varepsilon^\pi(|\frac{\mathbf{p}_0}{2} - \mathbf{k}|) + i\eta} \right) \end{aligned} \quad (3.22)$$

with  $V_\Delta$  representing the static higher-mass part of the potential, and the superscript ‘‘O.P.’’ recalling that the operator structure is included. The final inelastic  $\mathcal{T}$ -matrix equation written in terms of relative momenta  $\mathbf{k}_1$  and  $\mathbf{k}_2$  is

$$\begin{aligned} \langle \mathbf{k}_1 | \mathcal{T}_{inelastic}(E + E_\alpha) | \mathbf{k}_2 \rangle &= \langle \mathbf{k}_1 | (\tilde{V}_\pi(E, E_\alpha) + \Delta V) | \mathbf{k}_2 \rangle \\ &+ \frac{1}{2} \int \frac{d^3q}{(2\pi)^3} \langle \mathbf{k}_1 | (\tilde{V}_\pi(E, E_\alpha) + \Delta V) | \mathbf{q} \rangle G_{NN}^{(0)}(\mathbf{q}; E + E_\alpha) \\ &\times \langle \mathbf{q} | \mathcal{T}_{elastic}(E + E_\alpha) | \mathbf{k}_2 \rangle. \end{aligned} \quad (3.23)$$

A few observations about this integral must now be made.

1. This integral generates the full behavior of the inelastic  $\mathcal{T}$ -matrix . In our numerical scheme, it forms a matrix in momentum space which can be interpolated to any set of momenta. In practice, this matrix is used to interpolate a single value (or three in the case of coupled channels) in accordance with the relevant external momenta for the computation of scattering observables such as  $A_y$ . In the case of inelastic scattering, this samples off-shell elements of the  $\mathcal{T}$ -matrix where we have shown our interaction can differ substantially (see e.g. Fig. 2.12) from  $\mathcal{T}$ -matrices generated using static interactions.
2. Although the nucleon propagators are nonrelativistic, external variables are chosen in accordance with relativistic kinematics.
3. The angles appearing in all denominators are the same angles between relative momenta that we used in section 2.2.3 to perform our numerical projection onto angular momentum states in the case of elastic scattering, and an analogous (although not identical) projection is possible here as well. In this fashion, the integral equation is reduced to matrix multiplication.
4. In the case of elastic scattering, this matrix multiplication ultimately reduces to the Lippmann-Schwinger equation. The Lippman-Schwinger equation is typically solved [33] using a matrix inversion, and the elastic case allowed us to test the stability of our matrix multiplication. We found no appreciable reduction in accuracy for the matrix multiplication versus matrix inversion methods of solving the integral equation.

### 3.4 Results for $A_y$

We observed that non-negligible shifts occur in the potential when computed with the inclusion of dynamic pions. These differences in potential are illustrated in Figs. (3.7-3.12). In all channels there is a substantial difference between the inelastic DR1 and both the elastic version of DR1 and the static potential (RSC). These plots each represent the diagonal in momentum space of the potential in that uncoupled channel (or, in the case of the coupled channels, one orbital angular momentum block

of that channel) as a function of relative momentum. Displayed in black are the RSC values of the potential, while for comparison we provide the real parts of both the elastic (red) and inelastic (blue) versions of the DR1. The latter two potentials are computed with a 15MeV pion width for ease of presentation, but the change in width from the 5 MeV width used when fitting the DR1 has negligible affect on the computed value of  $A_y$ . We note that these plots are all generated for the kinematic conditions of the  $^{12}\text{C}$   $A_y$  data, with beam energy of 392 MeV and separation energy  $E_s = 36$  MeV. For these conditions, we sample a slightly off-shell  $\mathcal{T}$ -matrix element with relative momenta  $k_r = 2.39 \text{ fm}^{-1}$  and  $k'_r = 1.97 \text{ fm}^{-1}$ . We also remind the reader that although there is a complex part of the potential for energies above the pion production threshold, we do not use it in the construction of our  $\mathcal{T}$ -matrix. In any account, the value of the imaginary part of  $V$  is orders of magnitude smaller than the real part in the range of relative momenta (near  $2 \text{ fm}^{-1}$ ) relevant to calculation of  $A_y$ . The major discrepancy between potentials can be seen for low relative momenta. However, in the vicinity of the half off-shell values of relative momenta needed for calculation of  $A_y$  the majority of the channels agree substantially. Upon integration in the Lippmann-Schwinger equation these low  $k_r$  differences lead to changes in the  $\mathcal{T}$ -matrix elements, although in the case of the RSC and elastic DR1 there must still be some congruence between them in order to fit the same phase shifts. We expected these differences to lead to a substantial difference in the calculated value of  $A_y$ . Using the  $\mathcal{T}$ -matrix generated as discussed in section 3.3 we were able to compute  $A_y$  for a 392 MeV beam as a function of increasing separation energy  $E_s = -E_\alpha$ . We can see in Fig. 3.13 that at this energy the inclusion of our full inelastic  $\mathcal{T}$ -matrix (blue) creates a modest reduction in  $A_y$  compared to the partial-wave analysis (green), RSC (black) and the on-shell elements from the elastic  $\mathcal{T}$ -matrix (red). The latter three graphs of  $A_y$  are displayed to show the relative effect on  $A_y$  of the quality of the fit to data of the potential. We observe that using the full inelastic  $\mathcal{T}$ -matrix leads to an overall reduction of the magnitude of nearly 10% for small separation energy. However, as separation energy increases the amount of reduction in  $A_y$  becomes not much greater than the reduction already expected using the static RSC or simply using on-shell elastic  $\mathcal{T}$ -matrix elements generated from the PWA. Our task now is

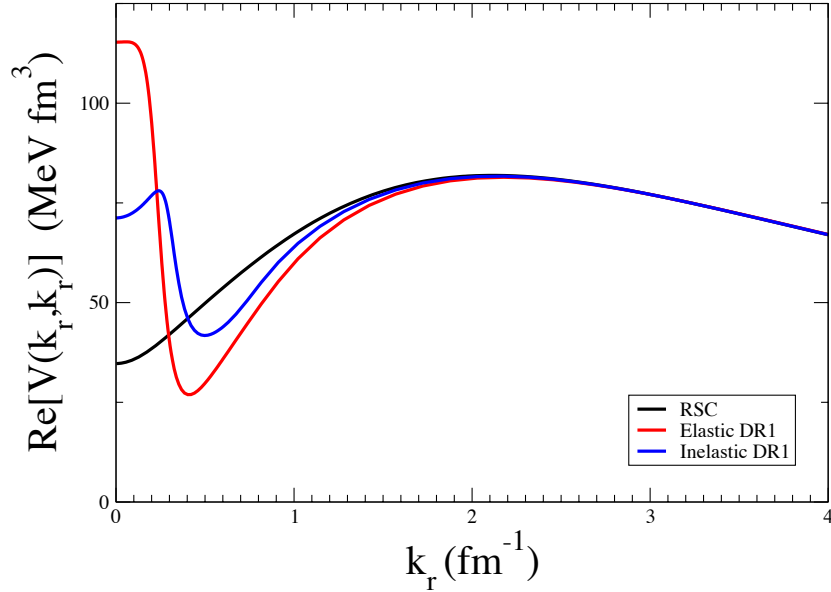


Figure 3.7: Diagonal in momentum space of the  ${}^1S_0$  potential for beam energy of 392 MeV with a 36MeV separation energy. Black is the RSC, red is the elastic DR1 and blue is the inelastic DR1. For these kinematic conditions, the appropriate half on-shell element has  $k_r = 2.39 \text{ fm}^{-1}$  and  $k'_r = 1.97 \text{ fm}^{-1}$ .

to understand why the differences in the  $\mathcal{T}$ -matrices do not translate into a more significant difference in  $A_y$ .

Before continuing, we should note that the limit  $E_\alpha \rightarrow 0$  does not lead to the free scattering case. One can see this by considering Eq. (3.16). If one sets  $E_\alpha = 0$  in this equation one is not left with simply the static pion propagator. The first term is unaffected by the limit, and does not reduce to the corresponding term for the elastic pion propagator found by setting  $\omega = 0$  in Eq. (2.3). The second term likewise does not reduce to the like term in Eq. (2.3) in the limit  $\omega \rightarrow 0$  due to the presence of the  $\varepsilon(\mathbf{p}'')$  term, which cannot be zero in the kinematic conditions presently under study. In other words, the pair of diagrams displayed in Fig. 3.4 do not reduce to the diagrams of Fig. 2.2 in the limit  $E_\alpha \rightarrow 0$ . The former represents a nucleon

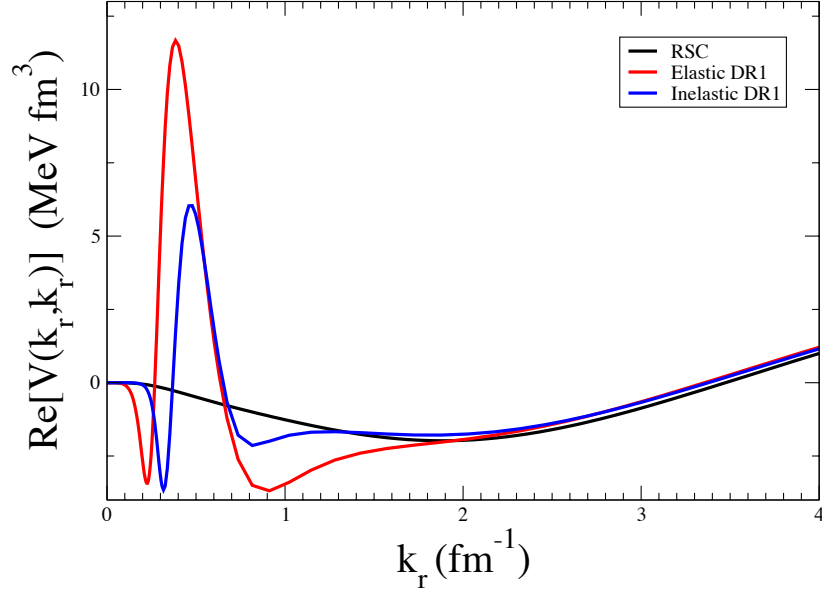


Figure 3.8:  ${}^1D_2$  potential. Details are as in Fig. 3.7

scattering off a nucleus, exciting a particle-hole state, while the second corresponds to scattering of one nucleon off another (free) nucleon. Therefore, we should *not* expect our inelastic  $\mathcal{T}$ -matrix to yield an  $A_y$  which agrees with the elastic treatment of  $A_y$  in the limit of zero separation energy.

We also point out that most of the reduction in  $A_y$  as separation energy increases is already observed for the static treatment. The majority of this reduction observed in  $A_y$  comes from two factors. The largest factor is the shift in C.M. angle that comes with increasing separation energy and the kinematics necessary to keep the collisions recoilless. We can see in Fig. 3.14 that for a given energy  $A_y$  is roughly sinusoidal when viewed as a function of center-of-mass scattering angle. For free  $pp$  scattering  $A_y$  is a constant for fixed center-of-mass scattering angle. However, for this quasi-free scattering with fixed lab angle, the kinematics necessary to ensure recoilless collision results in increasing center-of-mass scattering angles as separation energy increases, leading to a sampling of the  $A_y$  curve at different angles and a subsequent (for the lab

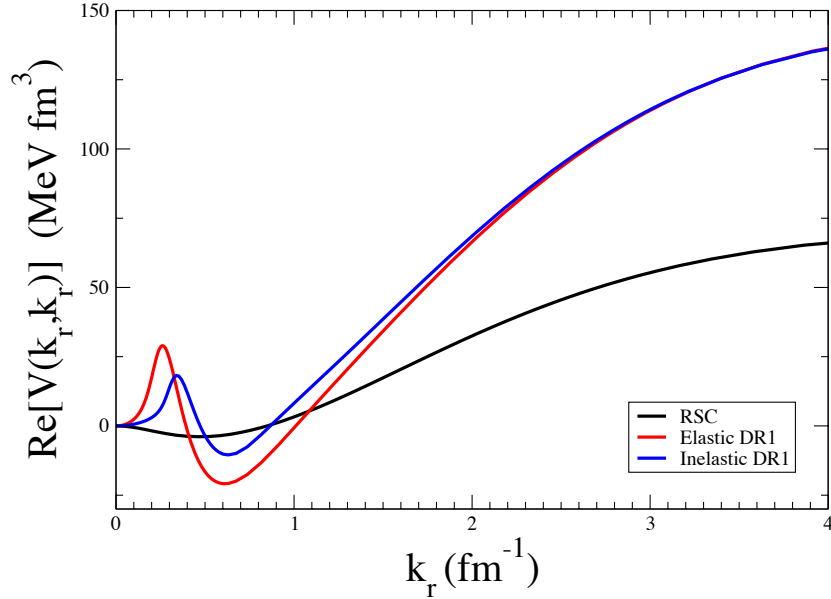


Figure 3.9:  ${}^3P_0$  potential. Details are as in Fig. 3.7

angle and energies considered in the current work) reduction in  $A_y$ . This reduction is an artifact of the fixed laboratory angle of the experimental set-up, and could just as easily become an enhancement of  $A_y$  for some other experimental set-up (e.g. if we were sampling values of  $A_y$  for angles *before* the peak of the  $A_y$  curve. This part of the reduction of  $A_y$  as a function of separation energy was also pointed out in Ref. [49], and accounts for perhaps one fifth of the experimentally observed reduction in  $A_y$ . This angular shift is the major factor in the reduction in  $A_y$  that we are seeing in Fig. 3.13. The second major factor is the shifted energy in the  $\mathcal{T}$ -matrix itself.  $A_y$  increases with energy. Since for *increasing* separation energy we are using  $\mathcal{T}$ -matrices at *decreasing* energies we see a corresponding reduction due simply to the fact that we are computing  $A_y$  for successively smaller energies as the separation energy increases.

To understand why our inelastic calculation does not have a greater effect on  $A_y$  we must consider exactly how the various terms in the potential contribute to  $A_y$ . Recall that  $A_y$  is a measure of asymmetry in cross section measurements for

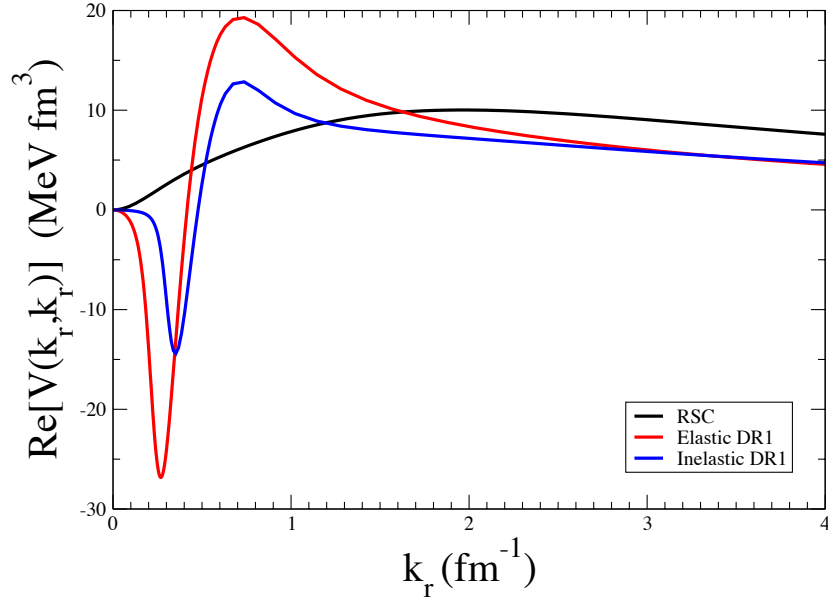


Figure 3.10:  ${}^3P_1$  potential. Details are as in Fig. 3.7

projectiles with opposite spin projection in the  $y$ -direction. This asymmetry comes about because of the presence of the two-body spin-orbit coupling in the potential. More precisely, this asymmetry is only possible in an observable if an odd power of  $\mathbf{S}$  appears within the observable. Since the central and tensor components have even powers of spin, they cannot contribute to any difference between the results of spin-up and spin-down measurements. The  $\mathbf{L} \cdot \mathbf{S}$  coupling is linear in spin, but on its own could not contribute to a non-zero  $A_y$  because it appears in an amplitude squared in the differential cross section (Eq. 3.2). Only when even and odd powers (*e.g.* from central or tensor and spin-orbit terms) of  $\mathbf{S}$  are included together can the amplitude squared contain cross terms with odd powers of spin.

Our model does not touch the spin-orbit coupling directly, other than to rescale the coupling constant in our refit to data after the addition of the dynamic pion. This rescaling ensures a good fit to the data in the elastic limit, but does not introduce any true dynamic corrections to the spin orbit terms. We expected that by including

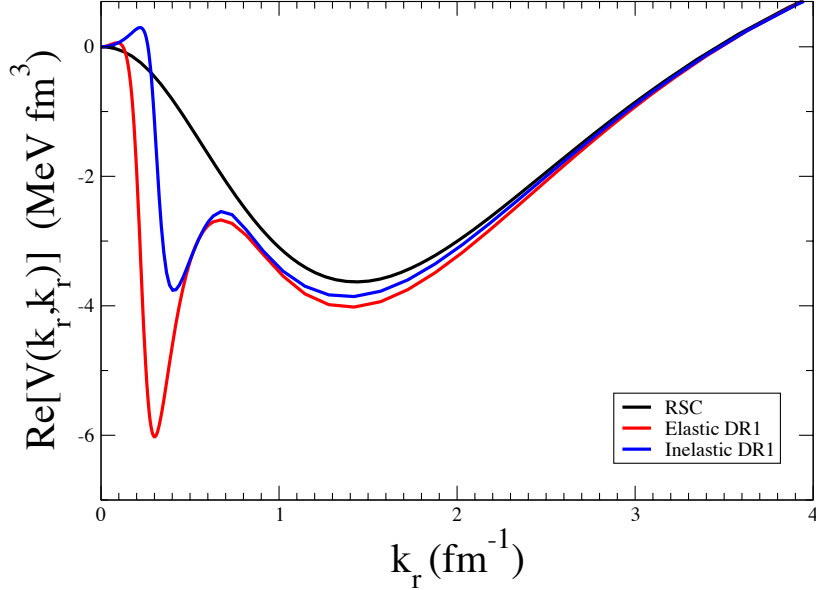


Figure 3.11:  ${}^3P_2$  block ( $L = 1, L' = 1$ ) of the potential for the  $J=2$  coupled channel. Details are as in Fig. 3.7

energy dependence in the pion alone, its contribution to  $A_y$  through the odd-powered spin cross terms in the differential cross section could make a significant change to the overall value of  $A_y$ , but this is a second-order effect. It may be that we need to extend the dynamic aspects to the higher-mass (and shorter range)  $\mathbf{L} \cdot \mathbf{S}$  terms in the interaction in order to observe a larger energy dependent effect on  $A_y$ . This would involve a complete refitting to the data and is possible in future work.

One other interesting factor which might be relevant is the fact that our interaction is charge independent, while  $A_y$  is highly sensitive to charge, especially for small angles. This can be observed in Fig. 3.15 which is taken from [20]. The solid curve shows the effect of including the Coulomb interaction to the nuclear interaction (dashed curve) when computing  $A_y$  for free proton-proton scattering. Although this effect is mostly observed for small angles, it is still apparent for larger angles in the region we are considering. We note only that this Coulomb effect could only



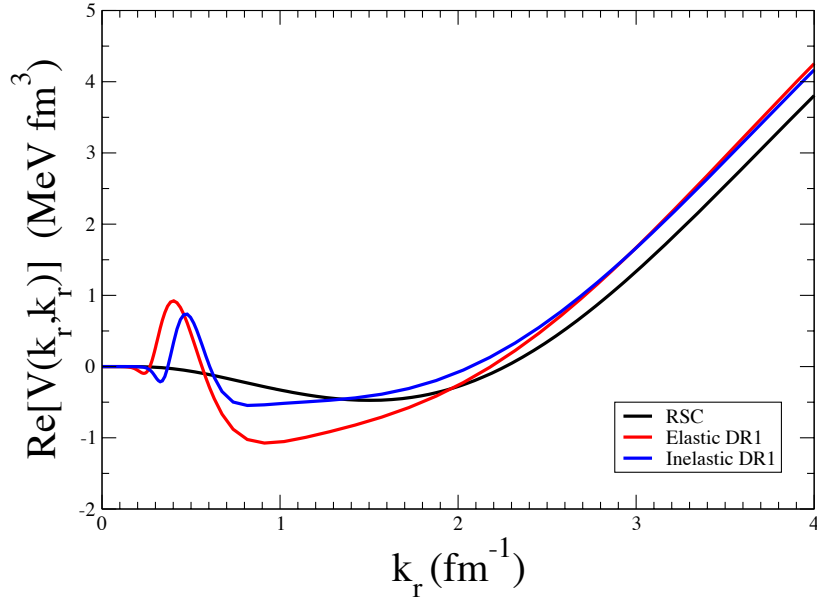


Figure 3.12:  ${}^3F_2$  block ( $L = 3, L' = 3$ ) of the potential for the  $J=2$  coupled channel. Details are as in Fig. 3.7

become stronger with increasing  $Z$  (and therefore increasing  $E_\alpha$ ), so that it might conspire with the other features we have mentioned to further alter  $A_y$  from the case of free scattering. A good strategy for exploring these ideas further would be to update a more modern charge dependent potential such as CDBonn [42], extending the dynamic meson-exchange to higher masses while also including the effects of the Coulomb interaction.

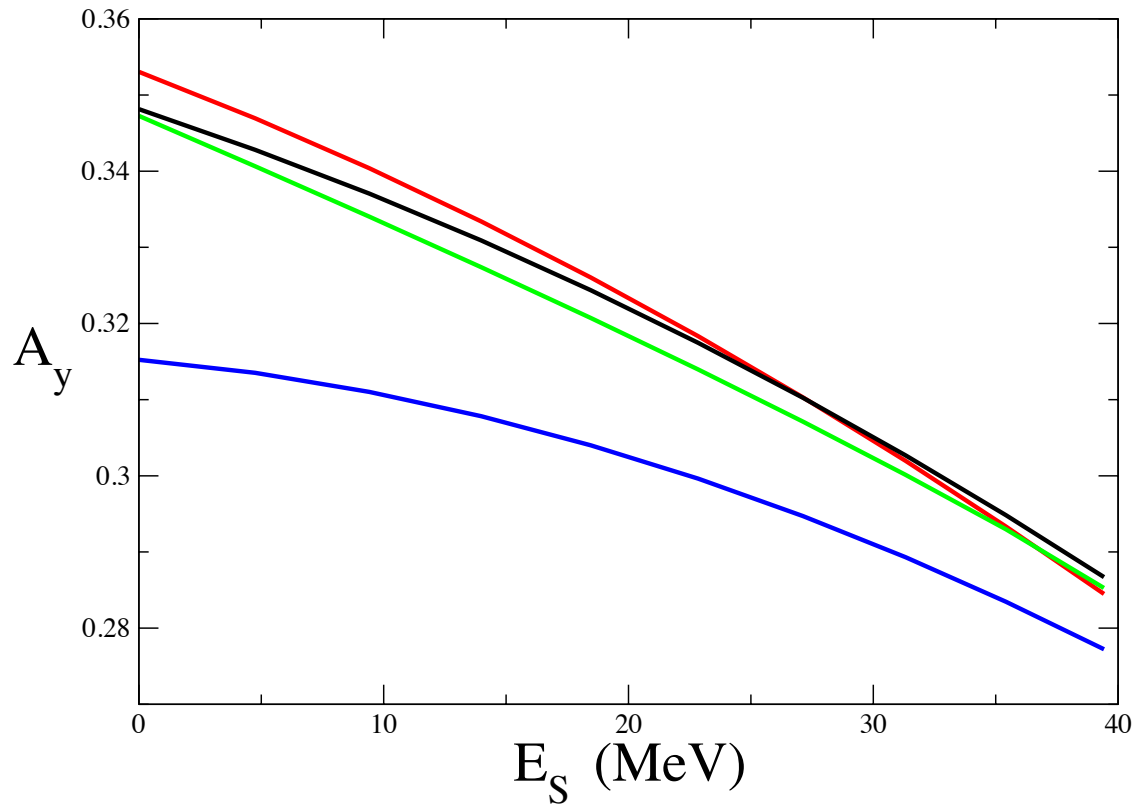


Figure 3.13:  $A_y$  computed for a 392 MeV beam as a function of separation energy using the RSC (black), DR1 (red), and PWA (green). Blue curve is generated using the full inelastic  $\mathcal{T}$ -matrix with the DR1 potential.

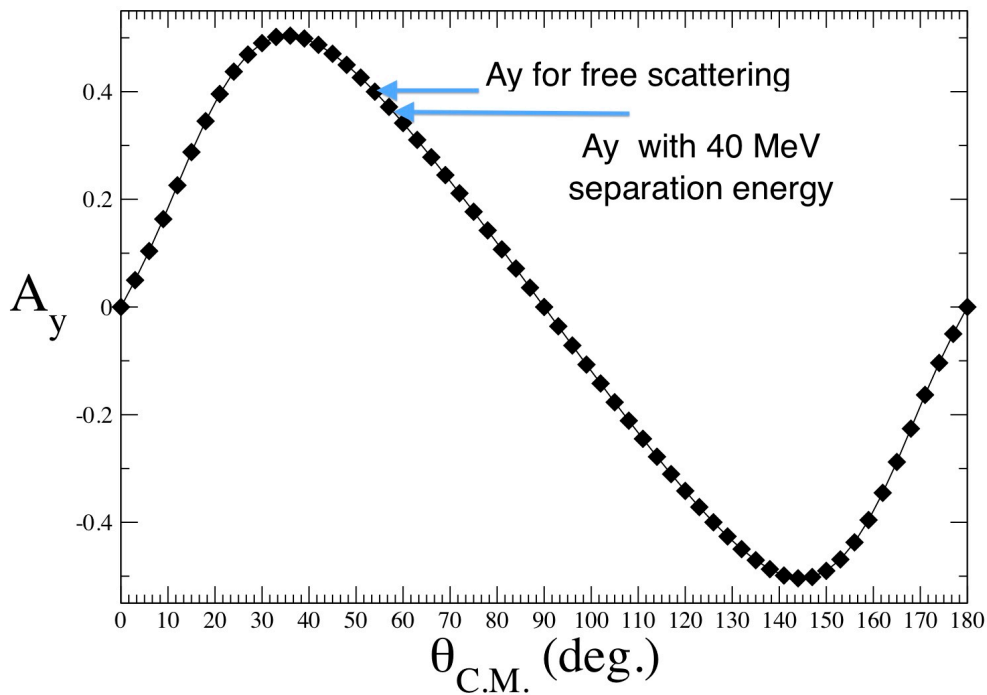


Figure 3.14:  $A_y$  for 392 MeV (lab) beam energy. Top arrow indicates the value of  $A_y$  for the kinematics of free scattering in the RCNP experimental set-up. Bottom arrow indicates the location of the angle that would be sampled for the same experimental set-up with a separation energy of 40 MeV. The increase in C.M. angle is due to the relativistic kinematics, and results in a corresponding reduction in  $A_y$  as separation energy increases. Plot was made using the  $T=1$  polarization numbers generated from the “Current Solution” phase-shift analysis of the Center for Nuclear Studies website [1].

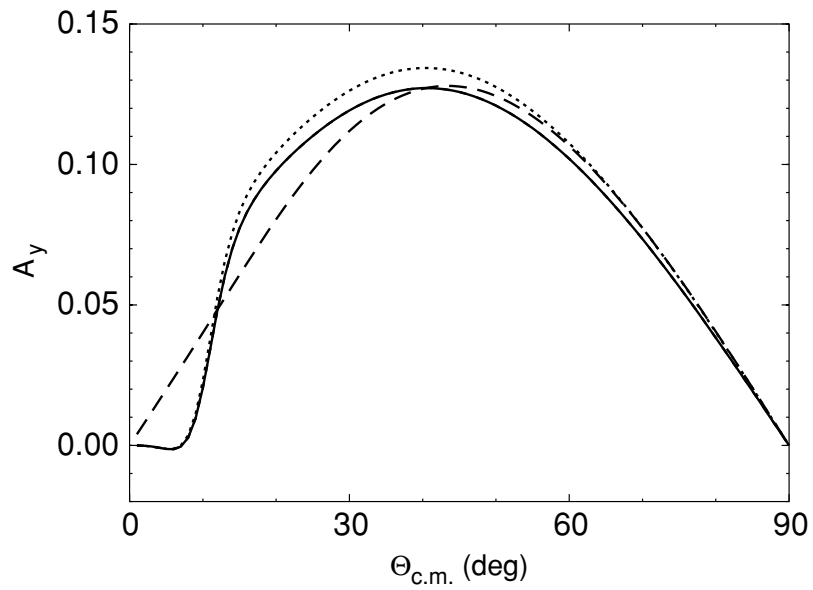


Figure 3.15: Figure taken from Ref. [20]. Proton analyzing power for  $pp$  scattering at 100-MeV proton lab energy as a function of the c.m. scattering angle. Exact results, given by the solid curve, are similar to the authors' Coulomb externally corrected approximation (dotted). The dashed curve corresponds to  $np$  results which do not include the Coulomb force.

# Chapter 4

## Nuclear Matter Saturation Problem

### 4.1 Background

The nuclear saturation problem has been studied in great detail and we provide a short review here. For a more detailed review, see [6, 21, 24]. The presence of the strong short-range repulsion in any realistic  $NN$  interaction makes a study of the properties of nuclear matter through perturbation theory impossible. The problem therefore requires a sophisticated treatment if one is to expect nuclear matter to become self-bound at realistic densities.

The binding energy per nucleon at saturation density of 16 MeV is given by the volume term of the Bethe-Weizsäcker [9, 66] formula, since for symmetric nuclear matter we can ignore any surface, electric charge, or isospin asymmetry effects. The experimentally well determined central charge density of  $^{208}\text{Pb}$  (0.16 nucleons/ $fm^{-3}$  with  $k_F = 1.33 fm^{-1}$ ) provides the preferred density of nuclear matter [31].

Galitskii [32] showed that in the low-density limit the most important terms to consider are multiple scattering events (ladder diagrams) between pairs of particles in the medium. The Hartree-Fock approximation generally fails to find a bound nucleus [47, 46], so it is necessary to consider medium effects which moderate this repulsion. Brueckner and Levinson [14] demonstrated the technique for summing

these ladder diagrams in what has become known as Brueckner  $G$ -matrix. This leads, upon calculation of the ground-state energy, to the so-called Brueckner-Hartree-Fock approximation. This approximation involves summing all ladder diagrams for two particles propagating outside of the Fermi sea (in other words with momenta above  $k_F$ ). The  $G$ -matrix (with notation introduced by Bethe [10]) differs from the free-space  $\mathcal{T}$ -matrix by including the Pauli exclusion principle and including a self-consistently determined single particle spectrum  $U(k)$ . The calculation of  $G$  involves the solution of the so-called Bethe-Goldstone equation

$$\begin{aligned} \langle \mathbf{k}m_\alpha m_{\alpha'} | G(\mathbf{K}, E) | \mathbf{k}'m_\beta m_{\beta'} \rangle &= \langle \mathbf{k}m_\alpha m_{\alpha'} | V | \mathbf{k}'m_\beta m_{\beta'} \rangle \\ &+ \frac{1}{2} \sum_{m_\gamma m_{\gamma'}} \int \frac{d^3q}{(2\pi)^3} \langle \mathbf{k}m_\alpha m_{\alpha'} | V | \mathbf{q}m_\gamma m_{\gamma'} \rangle \\ &\times \frac{\theta(|\mathbf{q} + \mathbf{K}/2| - k_F)\theta(|\mathbf{K}/2 - \mathbf{q}| - k_F)}{E - \varepsilon(\mathbf{q} + \mathbf{K}/2) - \varepsilon(\mathbf{K}/2 - \mathbf{q}) + i\eta} \langle \mathbf{q}m_\gamma m_{\gamma'} | G(\mathbf{K}, E) | \mathbf{k}'m_\beta m_{\beta'} \rangle, \end{aligned} \quad (4.1)$$

where *e.g.* the  $m_\alpha$  represent the discrete quantum numbers (spin, isospin), and  $\mathbf{K}$  is the total momentum, and  $\mathbf{k}, \mathbf{k}'$  and  $\mathbf{q}$  refer to relative momenta. In Eq. (4.1), it must be noted that the energies found in the two-particle propagator,  $\varepsilon(\mathbf{q} + \mathbf{K}/2)$  and  $\varepsilon(\mathbf{K}/2 - \mathbf{q})$ , require calculation of the BHF self-energy  $\Sigma_{BHF}$ , which in turn depends on the  $G$ -matrix and is calculated according to

$$\begin{aligned} \Sigma_{BHF}(k, E) &= \int \frac{d^3k'}{(2\pi)^3} \frac{1}{4} \sum_{m_\alpha m_{\alpha'}} \theta(k_F - k') \\ &\times \langle \frac{1}{2}(\mathbf{k} - \mathbf{k}')m_\alpha m_{\alpha'} | G(\mathbf{k} + \mathbf{k}', E + \varepsilon(\mathbf{k}')) | \frac{1}{2}(\mathbf{k} - \mathbf{k}')m_\alpha m_{\alpha'} \rangle. \end{aligned} \quad (4.2)$$

The single-particle energy  $\varepsilon(\mathbf{k})$  is related to the self-energy by

$$\varepsilon_{BHF}(k) = \frac{\hbar^2 k^2}{2m} + U(k) \quad (4.3)$$

where the auxiliary potential  $U(k)$  is related to the self-energy. Since one needs to know  $U(k)$  in order to compute the  $G$ -matrix, and the self-energy depends on  $G$ , we must solve the problem self-consistently. This non-linearity requires an iterative

approach such that with a reasonable ansatz for the single-particle spectrum, a self-consistent set  $G$  and  $\Sigma_{BHF}$  can be found. When performing this iterative procedure, a choice must be made regarding the relationship between the self-energy and the spectrum that is used. The most convenient from a computational point of view is to choose a spectrum with auxiliary potential  $U_s(k)$  known as “standard choice” or sometimes “gap choice” such that:

$$U_s(k) = \Sigma_{BHF}(k, \varepsilon_{BHF}(k))\theta(k_F - k). \quad (4.4)$$

In other words, the spectrum is equal to the on-shell self-energy for all values of  $k < k_F$ , and  $U_s(k) = 0$  for momenta higher than  $k_F$ . This is a practical strategy since one only needs to know the spectrum below the Fermi momentum in order to compute the binding energy per nucleon

$$\frac{E}{A} = \frac{2}{\rho} \int \frac{d^3k}{(2\pi)^3} \left( \frac{\hbar^2 k^2}{2m} + \varepsilon_{BHF} \right) \theta(k - k_F). \quad (4.5)$$

Once the spectrum is chosen we can evaluate the expression in the following form:

$$\begin{aligned} \frac{E}{A} = & \frac{4}{\rho} \int \frac{d^3k}{(2\pi)^3} \frac{\hbar^2 k^2}{2m} + \frac{1}{2\rho} \int \frac{d^3k}{(2\pi)^3} \int \frac{d^3k'}{(2\pi)^3} \sum_{m_\alpha m_{\alpha'}} \theta(k - k_F) \theta(k_F - k') \\ & \langle \frac{1}{2}(\mathbf{k} - \mathbf{k}') m_\alpha m_{\alpha'} | G(\mathbf{k} + \mathbf{k}'; \varepsilon_{BHF}(k) + \varepsilon_{BHF}(k')) | \frac{1}{2}(\mathbf{k} - \mathbf{k}') m_\alpha m_{\alpha'} \rangle. \end{aligned} \quad (4.6)$$

The gap choice has the advantage that if one restricts the calculation to include only particle-particle propagation (as in BHF), then  $G$  must only be computed once for the desired energies below  $2\varepsilon_F = \hbar^2 k_F^2 / m$  and then only the spectrum must be computed iteratively. Because the particles propagate above the Fermi momentum, where the potential  $U(k)$  is zero, there is no need to iteratively compute  $G$  since for these momenta the spectrum is fixed.

An often employed alternative choice advocated by Jeukenne *et al.* [36], and adopted in the present work, is the “continuous choice”, given by

$$U_c(k) = Re\{\Sigma_{BHF}(k, \varepsilon_{BHF}(k))\} \quad (4.7)$$

so that the spectrum is defined as the real part of the on-shell self-energy for all  $k$ . This approach has the advantage that it allows for a more natural link to the optical potential [36]. This is the strategy employed in the present work for reasons discussed in more detail below.

Historically the BHF approach has been employed for a large variety of realistic  $NN$  interactions always with the result that the strong short-range Hartree-Fock term has been compensated by the higher-order terms and the system is found to be bound. So far, BHF calculations fail to simultaneously predict the proper binding and saturation density, but Coester *et al.* [17] found that the calculated minima of  $E/A$  as a function of density are always found along a band (now referred to as the Coester band) as illustrated in Fig 4.1. In this figure, a band can clearly be seen described by the BHF saturation points (circles). The figure also clarifies that as the  $D$ -state probability of the deuteron increases the saturation point moves up and to the left along the so called Coester band. This suggests that the strength of the tensor force plays a crucial role in determining overall binding and saturation density. The three points (stars) which include three-hole-line contributions in the standard choice show that their inclusion greatly increases binding while moving the saturation point only to slightly higher density.

Higher-order approximations tend to be performed by grouping terms by the number of hole lines included in the summation. The BHF calculations sum all terms at the level of two-hole lines. To include three-hole lines, one must solve the Bethe-Faddeev equations [28, 52]. Day and Wiringa [19] found that variational calculations agreed well with calculations at the three-hole-line level. This was later confirmed by Song *et al.* [59] who also showed that BHF performed under the continuous choice at the two-hole-line level yielded results roughly equivalent to standard choice calculations including three-hole-line contributions for a variety of potentials. Furthermore, three-hole-line calculations in the continuous choice do not change the binding energy much, indicating that for the continuous choice two-hole-line calculations are already nearly converged. In addition, it has been shown that two-hole-line continuous choice calculations have strong agreement with the (also nearly converged) three-hole-line calculations under the gap choice. This indicates that higher-order correlations are largely included under the continuous choice already at the two-hole-line level. In



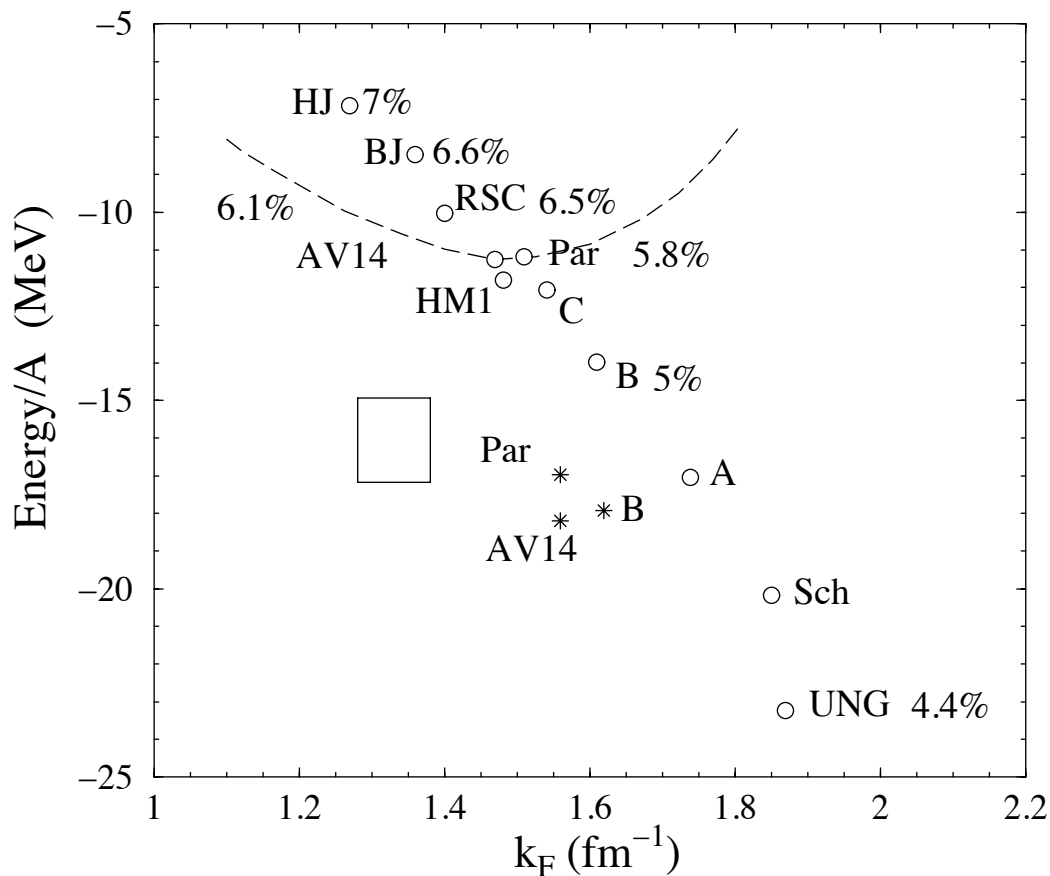


Figure 4.1: Plot of binding energy per nucleon as a function of Fermi momentum for various realistic  $NN$  interactions. The open circles represent the minimum of the saturation curves when computed in the BHF approximation using the standard choice for potential  $U_s(k)$ . The rectangle is the empirical region. The stars are the minima for interactions that have three-hole-line terms included in the standard choice. The dashed line is a sample saturation curve for the AV14 [69] potential. Also displayed for some potentials is the  $D$ -state probability. Figure taken from [24] and adapted from [6].

general, continuous-choice calculations at the two-hole-line level produce more binding compared to gap-choice calculations, particularly in the  $S$ -waves, similar to the amount of extra binding found by including contributions from three-hole-line diagrams, and so for our purposes the two approaches are more or less equivalent. Accordingly we use the continuous choice at the two-hole-line level in the present work.

Some progress on the saturation problem was made by Carlson *et al.* [16] with the inclusion of three-body forces. These phenomenological forces were fit to binding energies of light nuclei and adjusted to yield a satisfactory saturation density of nuclear matter. Extra repulsion was also added *ad hoc* in order to tune to the correct binding energy and saturation density, but the approach does not provide much insight into the mechanism of saturation, apart from pointing to the possible relevance of three-body forces.

Another approach that has been somewhat successful is the relativistic Dirac-BHF. The approach seems to yield good saturation properties, but has not been fully explored by calculating the three-hole-line contribution. A detailed discussion of this approach is beyond the scope of the present work, but the interested reader can find more details in Refs. [63, 11, 3].

Finally, there are some reasons to believe that a truer correspondence between nuclear matter and finite nuclei might be achieved if long-range correlations are deemphasized in nuclear-matter calculations. Recent experimental results in  $^{208}\text{Pb}$  [65] displayed in Fig 4.2 indicate that in nuclei the role of long-range correlations is confined to levels slightly below the Fermi energy, as shown by the curvature of the occupation numbers of proton shells near the Fermi energy. The relative flatness for more deeply bound protons points to the dominance of short-range correlations in depleting the Fermi sea. This  $(e, e'p)$  experiment for the first time covers a large range of missing momenta and energy and shows that the density behavior of the deeply bound  $s$ -waves is dominated by short-range physics. The saturation density extracted from the central charge density of  $^{208}\text{Pb}$  comes entirely from  $s$ -waves. Since only  $s$ -waves can be present in the central density, it has been argued [24, 21] that short-range correlations are dominant in determining nuclear matter saturation properties. Additionally, third-order pionic ring diagrams calculated in nuclear matter and included

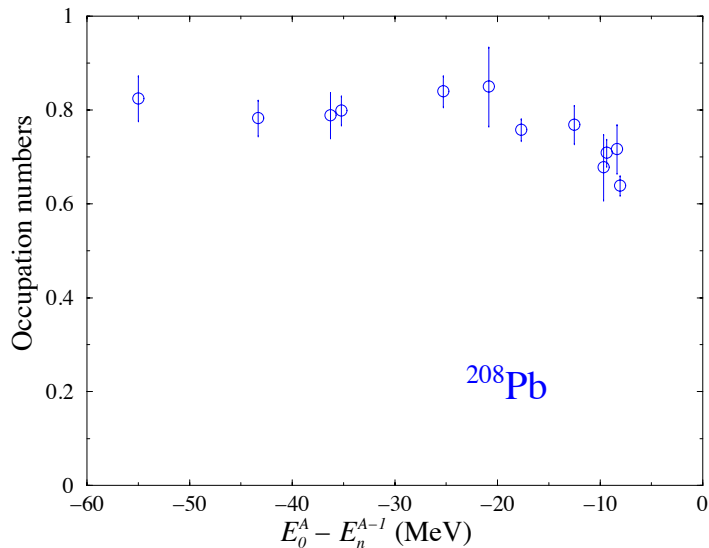


Figure 4.2: Plot of occupation numbers for all  $sp$  orbitals in  $^{208}\text{Pb}$ . Flatness over a large energy scale indicates the importance of short-range correlations in reducing occupation numbers, and in general for determining properties of nuclear matter. The lower energy long-range correlations result in the greater reduction in occupation near the Fermi energy. Figure taken from [24] and adapted from [65].

at the three-hole-line level exhibit considerable attraction, which increases at higher density [22]. Accordingly, they tend to shift the minimum of the saturation curve to the right. Although collective pionic modes must be important in true nuclear matter, they may not be as relevant in finite nuclei (indeed such collective behavior has not been observed) and perhaps *ought not* to be considered when trying to find agreement between nuclear-matter properties and finite nuclei. The authors of [21] report that by using the Self-Consistent Green's Functions (SCGFs) approach including only short-range correlations self-consistently but including full off-shell propagation their results move off the Coester band to the left toward the empirical region (see Fig 4.3). These calculations are more sophisticated than the continuous choice BHF in that

they include both particle-particle  $pp$  and hole-hole  $hh$  propagation self-consistently. They use more realistic spectral functions generated through the SCGF method to represent nucleon propagation [24].

Our goal in this work is not to settle this long-standing unsolved problem, but rather to assess whether or not including a dynamic interaction has anything to say about it. Toward that end, we adopt a BHF calculation under the continuous choice. By making a comparison between static and dynamic calculations at this already fairly well-converged level we can assess whether it is worthwhile to pursue more technically involved procedures in the pursuit of a solution to the nuclear-matter saturation problem.

## 4.2 Computational details

We have chosen to use the BHF  $G$ -matrix as the testing ground of the importance of energy-dependent interactions on the properties of nuclear matter. We sum ladder diagrams to properly control the strong short-range repulsion of our bare interaction, including  $pp$  propagation but neglecting  $hh$  propagation. It has been shown that  $hh$  propagation will tend to introduce some repulsion, so that our results will be overbound relative to a treatment which includes  $hh$  propagation on equal footing with  $pp$ , but it must be recalled that our main goal is much more modest than trying to achieve the correct binding energy and saturation density of nuclear matter. Rather we try only to assess what effect, if any, using dynamic  $NN$  interactions has on nuclear-matter calculations.

In this section, we present first the details of the standard BHF calculation in the continuous choice, and then the modifications to the procedure which must be made to perform this calculation using a dynamic interaction. Many of the details can be found in Ref. [53], although that author includes  $hh$  propagation as well and uses a simpler bare interaction. In the following, we suppress spin and isospin indices, and rewrite the Bethe Goldstone equation in terms of the Pauli operator  $Q_{pp}(\mathbf{K}, \mathbf{q})$  given by

$$Q_{pp}(\mathbf{K}, \mathbf{q}) = \theta(|\mathbf{q} + \mathbf{K}/2| - k_F)\theta(|\mathbf{K}/2 - \mathbf{q}| - k_F). \quad (4.8)$$

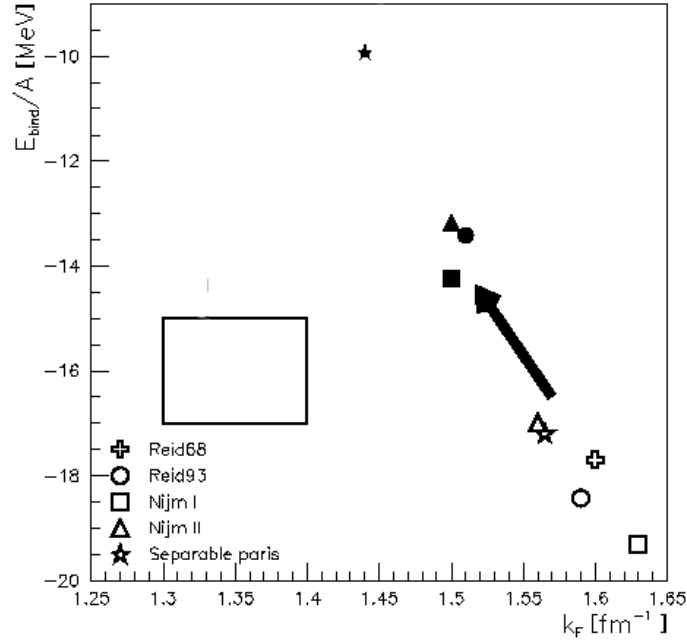


Figure 4.3: Plot of binding energy per nucleon as a function of Fermi momentum for various realistic  $NN$  interactions. Open points indicate continuous choice BHF saturation points for various potentials. Filled points represent calculations with fully self-consistent treatment of short-range correlations using a discrete pole approximation for the spectral functions, except for the two Reid68 points with error bars. Those two points are fully self-consistent calculations in the continuous version of the spectral functions which are not fully converged (uncertainty in convergence represented by the error bars). Rectangle is the empirical saturation region as in Fig. 4.1. Figure taken from [21].

We can then rewrite Eq. (4.1) as follows

$$\begin{aligned} \langle \mathbf{k}_r | G(\mathbf{K}, E) | \mathbf{k}'_r \rangle &= \langle \mathbf{k}_r | V | \mathbf{k}'_r \rangle + \frac{1}{2} \int \frac{d^3 q}{(2\pi)^3} \langle \mathbf{k}_r | V | \mathbf{q} \rangle \\ &\times \frac{Q_{pp}(\mathbf{K}, \mathbf{q})}{E - \varepsilon(|\mathbf{K}/2 + \mathbf{q}|) - \varepsilon(|\mathbf{K}/2 - \mathbf{q}|) + i\eta} \langle \mathbf{q} | G(\mathbf{K}, E) | \mathbf{k}'_r \rangle. \end{aligned} \quad (4.9)$$

Our interaction is expressed in the partial-wave basis, but the presence of the angle between  $\mathbf{K}$  and  $\mathbf{q}$  in the Pauli operator and the energy denominator makes a partial-wave expansion problematic.

### 4.2.1 Treatment of the Pauli operator

Since our potential is already expressed in a partial-wave basis, it would be inconvenient to allow the channels to remix through the angles contained in the Pauli operator. The traditional approach [13] for dealing with this is to perform an angle averaging on the Pauli operator before initiating the partial-wave expansion, and using instead the so called “angle-averaged Pauli operator”  $\bar{Q}(K, q)$  defined by

$$\bar{Q}_{pp}(K, q) = \frac{1}{2} \int_{-1}^1 Q_{pp}(\mathbf{K}, \mathbf{q}) d \cos \theta. \quad (4.10)$$

Although this is a choice of convenience and has been the standard treatment for decades, it has recently been under some scrutiny and it has been shown [61, 56, 57] that the effect of the angle-averaging approximation is minimal, resulting in slightly smaller binding globally while leaving the saturation density unchanged, as shown in Fig. 4.4. For a more up-to-date discussion of the errors induced by angle-averaging the Pauli operator, see [4]. Since the error due to this approximation appears small, and we are not concerned with our overall binding we will use the angle-averaging procedure without further discussion of its merits or faults beyond the pragmatic.

To evaluate Eq. (4.10) we note that  $Q_{pp}(\mathbf{K}, \mathbf{q})$  is equal to unity if both particles are outside the Fermi sea, and zero otherwise. This means that it essentially restricts the angles of integration depending on the relative magnitudes of  $\mathbf{K}$ ,  $\mathbf{q}$ , and  $k_F$ . The

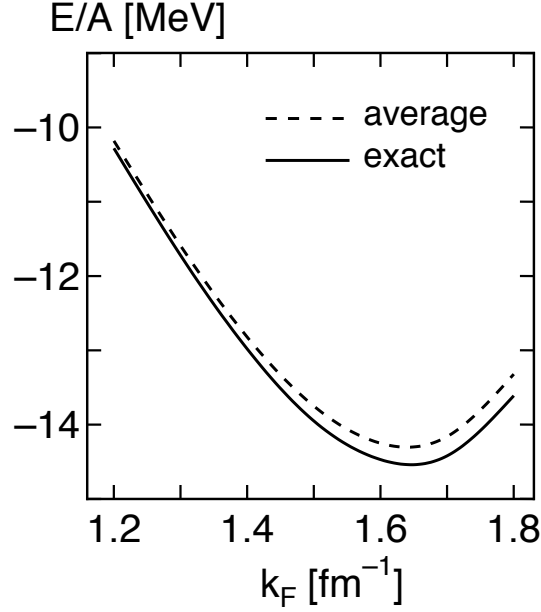


Figure 4.4: Plot of saturation curves for Bonn B potential using angle-averaged Pauli operator (dashed) and exact Pauli operator including partial waves up to  $J = 6$ . This and a similar plot with the same trend may be found in Ref. [61].

integral then becomes

$$\bar{Q}_{pp}(K, q) = \frac{1}{2} \int_{\cos \theta_1}^{\cos \theta_2} Q_{pp}(\mathbf{K}, \mathbf{q}) d \cos \theta. \quad (4.11)$$

To evaluate the limits, we consider the diagrams in Figs. 4.5 and 4.6. Figure 4.5 shows the two theta functions that compose the Pauli operator in the case where  $\mathbf{K}/2 > k_F$ . We can see that the angles between  $\mathbf{K}/2$  and  $\pm \mathbf{q}$  are complimentary. The upper limit  $\theta_2$  will be dictated by Fig. 4.5a, while the lower limit  $\theta_1$  will be dictated by Fig. 4.5b. If either  $q < K/2 - k_F$  or  $q > K/2 + k_F$  then there is no restriction on angle because both particles are guaranteed to lie outside of the Fermi sea. Consequently in these cases,  $\bar{Q}_{pp}(K, q) = 1$ . Otherwise, because of the complementarity of these two angles

( $\theta_1 = \pi - \theta_2$ ) we have finally from Eq (4.11)

$$\bar{Q}_{pp}(K, q) = \cos \theta_2. \quad (4.12)$$

where  $\cos \theta_2$  is given by

$$\cos \theta_2 = \frac{q^2 + \frac{K^2}{4} - k_F^2}{Kq} \quad (4.13)$$

On the other hand, if  $\mathbf{K}/2 < k_F$ , we must consider Fig. 4.6. In these diagrams  $\mathbf{q}$  has been displayed in the position that grants it its minimum value such that both  $\mathbf{q}$  and  $-\mathbf{q}$  barely lie outside the Fermi sphere. If  $\mathbf{q}$  were any smaller, then orientations which leave it outside the Fermi sphere must leave  $-\mathbf{q}$  inside, and vice versa. Consequently  $\bar{Q}_{pp}(K, q) = 0$  for all values of  $q$  such that  $q < \sqrt{k_F^2 - \frac{K^2}{4}}$ . On the other hand, if  $q > K/2 + k_F$  then the angular integration is unrestricted and  $\bar{Q}_{pp}(K, q) = 1$ . Otherwise  $\cos \theta_2 = \frac{q^2 + \frac{K^2}{4} - k_F^2}{Kq}$ . Finally, we can summarize this as follows:

$$\bar{Q}(K, q) = \begin{cases} 0 & \text{if } 0 \leq q < \sqrt{k_F^2 - \frac{K^2}{4}}, \\ \frac{q^2 + \frac{K^2}{4} - k_F^2}{Kq} & \text{if } \sqrt{k_F^2 - \frac{K^2}{4}} \leq q < k_F + \frac{K}{2}, \\ 1 & \text{if } k_F + \frac{K}{2} \leq q. \end{cases} \quad (4.14)$$

if  $K/2 < k_F$  and

$$\bar{Q}(K, q) = \begin{cases} 1 & \text{if } 0 \leq q < \frac{K}{2} - k_F, \\ \frac{q^2 + \frac{K^2}{4} - k_F^2}{Kq} & \text{if } \frac{K}{2} - k_F < q \leq k_F + \frac{K}{2}, \\ 1 & \text{if } k_F + \frac{K}{2} < q, \end{cases} \quad (4.15)$$

if  $K/2 \geq k_F$ .

We can handle the angular dependence of the energy denominator with a similar averaging. Because of the dual energies in the denominator of the form  $f(|\mathbf{K}/2 - \mathbf{q}|)$  and  $f(|\mathbf{K}/2 + \mathbf{q}|)$  the lowest order of angular dependence generated from their sum



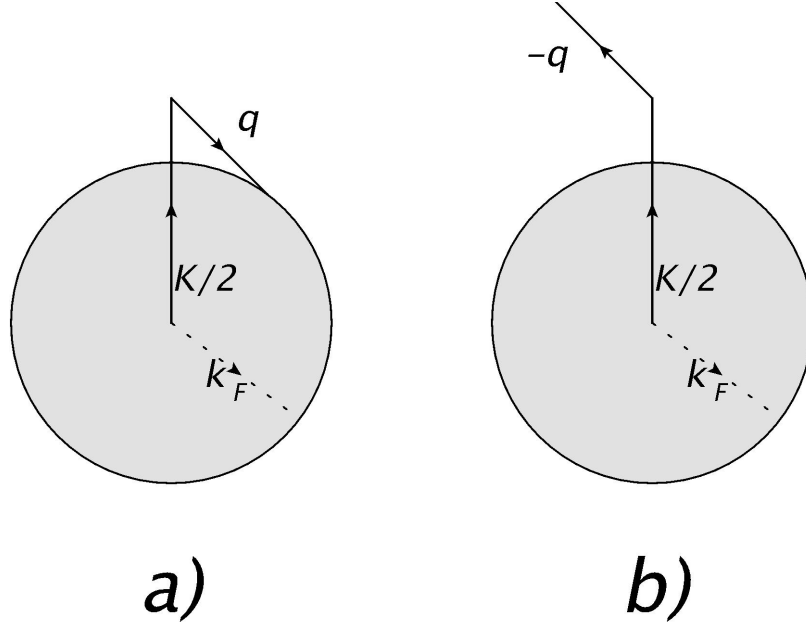


Figure 4.5: In these diagrams we have the case where  $\mathbf{K}/2 > k_F$ . Diagram a) illustrates  $\theta(|\mathbf{q} + \mathbf{K}/2| - k_F)$  while diagram b) illustrates  $\theta(|\mathbf{K}/2 - \mathbf{q}| - k_F)$ .

will be from quadratic terms of the form  $(\mathbf{K} \cdot \mathbf{q})^2$ . We can replace these terms by their angle-average  $\langle \mathbf{K} \cdot \mathbf{q} \rangle^2$  as follows

$$\langle \mathbf{K} \cdot \mathbf{q} \rangle^2 = \langle K^2 q^2 \cos^2 \theta \rangle = K^2 q^2 \langle \cos^2 \theta \rangle_{Kq} \quad (4.16)$$

where

$$\langle \cos^2 \theta \rangle_{Kq} = \frac{1}{2} \int_{-1}^1 \cos^2 \theta Q_{pp}(\mathbf{K}, \mathbf{q}) d \cos \theta. \quad (4.17)$$

In this expression, the Pauli operator ensures that the same limits occur on the angles, so in effect

$$\langle \cos^2 \theta \rangle_{Kq} = \frac{\cos^2 \theta_2^3}{3} = \frac{1}{3} \bar{Q}^3(K, q). \quad (4.18)$$

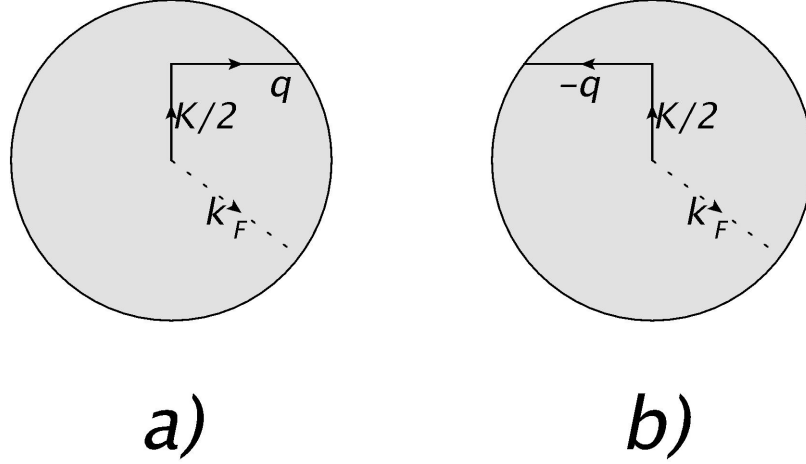


Figure 4.6: In these diagrams we have the case where  $\mathbf{K}/2 < k_F$ . Diagram a) illustrates  $\theta(|\mathbf{q} + \mathbf{K}/2| - k_F)$  while diagram b) illustrates  $\theta(|\mathbf{K}/2 - \mathbf{q}| - k_F)$ .

Using these results, we can now express the arguments of the single-particle energies  $\varepsilon(|\mathbf{K}/2 + \mathbf{q}|)$  and  $\varepsilon(|\mathbf{K}/2 - \mathbf{q}|)$  with angle-averaged arguments

$$|\mathbf{K}/2 \pm \mathbf{q}| = \frac{1}{4}K^2 + q^2 \pm \frac{1}{\sqrt{3}}Kq\bar{Q}^{\frac{3}{2}}(K, q). \quad (4.19)$$

Although the angle-averaged Pauli operator will greatly simplify our calculation when we move to a partial-wave basis by “removing” any additional angular dependence, the discontinuities in its derivatives will pose some numerical challenges. Since the Pauli operator appears in the  $sp$  energies, and we will later need to take derivatives of the  $sp$  energies, we provide here analytical expressions for  $\frac{\partial \bar{Q}(K, q)}{\partial q}$

$$\frac{\partial \bar{Q}(K, q)}{\partial q} = \begin{cases} 0 & \text{if } 0 \leq q < \sqrt{k_F^2 - \frac{K^2}{4}}, \\ \frac{q^2 + k_F^2 - \frac{K^2}{4}}{Kq^2} & \text{if } \sqrt{k_F^2 - \frac{K^2}{4}} \leq q < k_F + \frac{K}{2}, \\ 0 & \text{if } k_F + \frac{K}{2} \leq q. \end{cases} \quad (4.20)$$

if  $K/2 < k_F$  and

$$\frac{\partial \bar{Q}(K, q)}{\partial q} = \begin{cases} 0 & \text{if } 0 \leq q < \frac{K}{2} - k_F, \\ \frac{q^2 + k_F^2 - \frac{K^2}{4}}{Kq^2} & \text{if } \frac{K}{2} - k_F < q \leq k_F + \frac{K}{2}, \\ 0 & \text{if } k_F + \frac{K}{2} < q. \end{cases} \quad (4.21)$$

if  $K/2 \geq k_F$ . We can see the features of  $\bar{Q}(K, q)$  and  $\frac{\partial \bar{Q}(K, q)}{\partial q}$  plotted in Figs. 4.7 and 4.8. Note the discontinuities in the derivatives. We will have to take care that when we discretize any integrals involving  $\frac{\partial \bar{Q}(K, q)}{\partial q}$  our mesh creation is sensitive to the locations of these discontinuities. A discussion of the mesh creation is given in Ref. [53].

## 4.2.2 Calculation of the $G$ -matrix

We now return to the Bethe-Goldstone equation Eq. (4.1) and express it in a partial-wave basis as in Ref. [53]. In this section we treat the uncoupled channels only, leaving the more elaborate but fundamentally similar coupled channels for Appendix B. Using the angle-averaging approximation for a given total angular momentum  $J$ , total spin  $S$ , and total isospin  $T$ , we can write

$$G_L(k_r, k'_r, K, E) = V_L(k_r, k'_r) + \int_0^\infty q^2 dq V_L(k_r, q) \times \frac{\bar{Q}_{pp}(\mathbf{K}, \mathbf{q})}{E - \varepsilon(|\mathbf{K}/2 + \mathbf{q}|) - \varepsilon(|\mathbf{K}/2 - \mathbf{q}|) + i\eta} G_L(q, k'_r, K, E). \quad (4.22)$$

It is clear that whenever the energy  $E$  equals the two-particle energy the integral encounters a pole. A standard way of dealing with this numerically [33] is with the creation of the real reaction matrix  $R_L$  given schematically in operator form by

$$R_L = V_L + V_L \mathcal{P} \frac{\bar{Q}_{pp}}{E - \varepsilon} R_L \quad (4.23)$$

where the  $\mathcal{P}$  indicates performing a principle parts integral if there is a pole, and the energy  $\varepsilon$  represents the energy of two particles propagating outside of the Fermi sea.

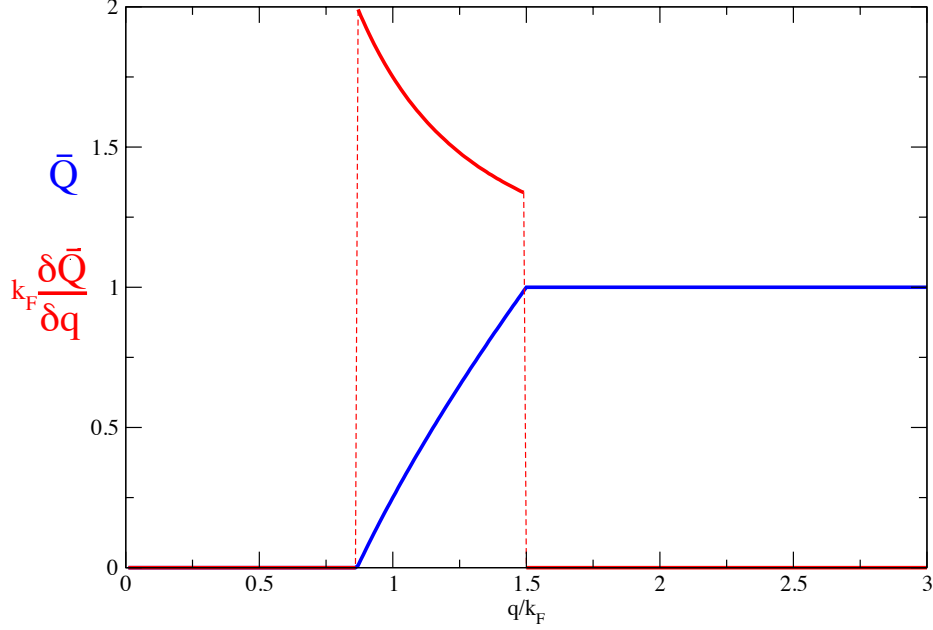


Figure 4.7: Plot of  $\bar{Q}(K, q)$  (blue) and  $k_F \times \frac{\partial \bar{Q}(K, q)}{\partial q}$  (red) for the case  $K/2 < k_F$ . In this plot, we have taken  $K = k_F$ . This figure has been adapted from a similar figure presented for the full  $(pp + hh)$  Pauli operator in Ref. [53].

$R_L$  can be constructed using a matrix inversion [33] as follows:

$$R_L - V_L \mathcal{P} \frac{\bar{Q}_{pp}}{E - \varepsilon} R_L = V_L \quad (4.24)$$

$$\{\mathbf{I} - V_L \mathcal{P} \frac{\bar{Q}_{pp}}{E - \varepsilon}\} R_L = V_L \quad (4.25)$$

$$R_L = \{\mathbf{I} - V_L \mathcal{P} \frac{\bar{Q}_{pp}}{E - \varepsilon}\}^{-1} V_L. \quad (4.26)$$

We can also write Eq. (4.22) for the  $G$ -matrix in operator form as well by

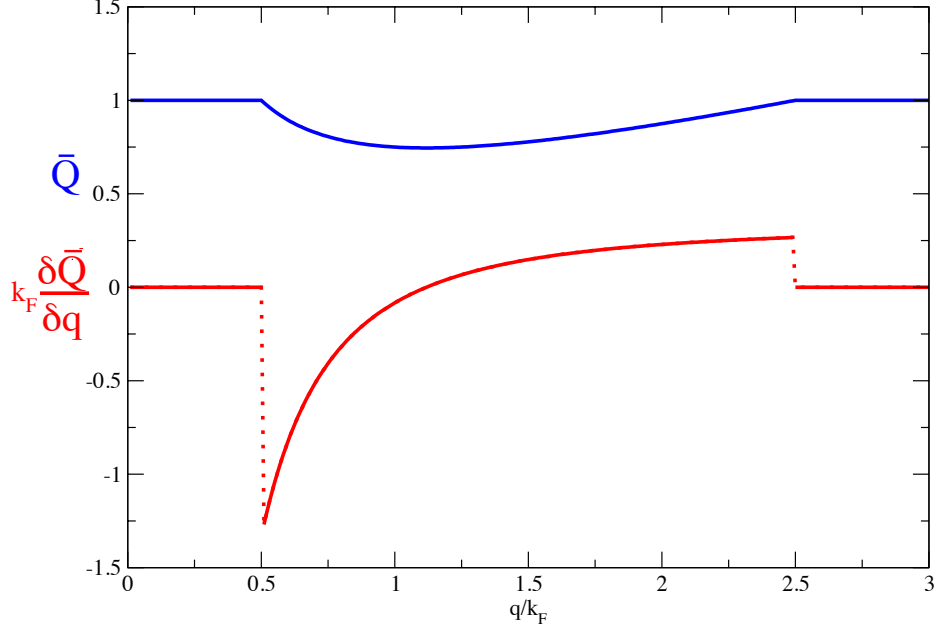


Figure 4.8: Plot of  $\bar{Q}(K, q)$  (blue) and  $k_F \times \frac{\partial \bar{Q}(K, q)}{\partial q}$  (red) for the case  $K/2 > k_F$ . In this plot, we have taken  $K = 3k_F$ . This figure has been adapted from a similar figure presented for the full  $(pp + hh)$  Pauli operator in Ref. [53].

$$G_L = V_L + V_L \frac{\bar{Q}_{pp}}{E - \varepsilon + i\eta} G_L. \quad (4.27)$$

Then the connection between  $R$  and  $G$  is

$$G_L = R_L - i\pi R_L \bar{Q}_{pp} \delta(E - \varepsilon) G_L. \quad (4.28)$$

From this we can see that for energies below twice the Fermi energy, where the integration encounters no pole,  $G_L$  is real and equal to  $R_L$ . We can write this equation

explicitly in terms of momentum and energy variables as follows:

$$G_L(k_r, k'_r, K, E) = R_L(k_r, k'_r, K, E) - i\pi \int_0^\infty q^2 dq R_L(k_r, q, K, E) \\ \times \bar{Q}_{pp}(K, q) \delta(E - \varepsilon(|\mathbf{K}/2 + \mathbf{q}|) - \varepsilon(|\mathbf{K}/2 - \mathbf{q}|)) G_L(q, k'_r, K, E) \quad (4.29)$$

The integral can be evaluated explicitly due to the  $\delta$ -function, by noting

$$\delta(f(x)) = \left| \frac{df(x)}{dx} \right|_{x=x_0}^{-1} \times \delta(x - x_0) \quad (4.30) \\ \text{with } f(x_0) = 0,$$

so that Eq. (4.29) becomes

$$G_L(k_r, k'_r, K, E) = R_L(k_r, k'_r, K, E) - i \frac{\pi k_p^2}{\left| \frac{dE}{dq} \right|_{q=k_p}} R_L(k_r, k_p, K, E) \\ \times \bar{Q}_{pp}(K, k_p) G_L(k_p, k'_r, K, E), \quad (4.31)$$

where  $k_p$  is the value of the momentum at the pole. We note that the  $G$ -matrices appearing on right and left have different arguments, but by taking  $k_r = k_p$  we can solve algebraically for  $G_L(k_p, k'_r, K, E)$ . We can also simplify our expression by letting

$$A(k_p) = \frac{\pi k_p^2 \bar{Q}_{pp}(K, k_p)}{\left| \frac{dE}{dq} \right|_{q=k_p}}. \quad (4.32)$$

Having done this, we can reinsert the expression for  $G_L(k_p, k'_r, K, E)$  into Eq. (4.31) with the resulting final expression

$$G_L(k_r, k'_r, K, E) = R_L(k_r, k'_r, K, E) \quad (4.33)$$

$$- A^2(k_p) \frac{R_L(k_r, k_p, K, E) R_L(k_p, k'_r, K, E) R_L(k_p, k_p, K, E)}{1 + A^2(k_p) R_L^2(k_p, k_p, K, E)} \\ - i \frac{R_L(k_r, k_p, K, E) R_L(k_p, k'_r, K, E)}{1 + A^2(k_p) R_L^2(k_p, k_p, K, E)}. \quad (4.34)$$

Since the  $R$ -matrix is real, we can see explicitly that the real part of the  $G$ -matrix is given by the first two terms on the RHS, while the third term is the imaginary part.

The procedure for handling the coupled channels is essentially the same, but has the additional complication that there is a sum over angular momentum states within the coupled channel. The details are given in Appendix B.

Computation of the  $G$ -matrix through the real reaction matrix has been found to be quite numerically stable [33] once the proper momentum and energy meshes have been chosen, but because of the discontinuities in the Pauli operator the construction of the proper mesh requires considerable thought. Particular details can be found in Ref. [53].

### 4.3 Self-energy and binding

Once we have computed the  $G$ -matrix with a suitable *ansatz* for the  $sp$  spectrum we can generate the real part of the self-energy according to the real part of Eq. (4.2). From the partial-wave basis, we can recover the full  $G$ -matrix with

$$\begin{aligned} \text{Re } G(k_r, k'_r, K, E) = \\ \sum_{LST} (1 - (-1)^{L+S+T}) (2J+1)(2T+1) \text{Re } G_L(k_r, k'_r, K, E) \end{aligned} \quad (4.35)$$

so that, defining  $\mathbf{P} = \mathbf{K}/2$ , we have

$$\begin{aligned} \text{Re } \Sigma_{BHF}(k, E) = \int P^2 dP d(\cos \theta) \\ \times \text{Re } G(k_r, 2P, E + \varepsilon(\mathbf{k}')) \theta(k_F - k') \end{aligned} \quad (4.36)$$

where

$$k_r = \left| \frac{\mathbf{k} - \mathbf{k}'}{2} \right| = |\mathbf{k} - \mathbf{P}| = \sqrt{k^2 + P^2 - 2kP \cos \theta} \quad (4.37)$$

and

$$k' = \left| 2\mathbf{P} - \mathbf{k} \right| = \sqrt{k^2 + 4P^2 - 4kP \cos \theta}. \quad (4.38)$$

The only subtlety involved in evaluating this integral lies in evaluating the theta-function. As we can see in Figs. 4.9a and 4.9b, the Fermi sphere imposes minimum and maximum restrictions on  $P$  for the  $dP$  integral. From Fig. 4.9a, we see that when  $\mathbf{k} < k_F$  that in order for  $2\mathbf{P} - \mathbf{k}$  to remain inside the Fermi sphere,  $2\mathbf{P}$  must be less than or equal to than  $k_F + k$ . If, on the other hand,  $k > k_F$ , then Fig. 4.9b illustrates the additional condition that if  $2\mathbf{P} < (k - k_F)$  then  $2\mathbf{P} - \mathbf{k}$  can never be inside the Fermi sphere. The upper limit on  $P$  remains the same in this case. These features can be summarized as follows:

$$\begin{aligned} 0 < 2P < k + k_F & & k < k_F \\ k - k_F < 2P < k + k_F & & k > k_F. \end{aligned}$$

So, for a given  $k$ , this condition creates limits on the  $dP$  integral, allowing us to create a momentum mesh  $P_i$  for the evaluation of this integral. Then, for each  $P_i$ , limits for the  $d\cos\theta$  integral must be computed. Here again the Fermi sphere can impose limitations on the possible values of  $\cos\theta$ , as seen in Fig. 4.10. Keeping in mind that the angle in the integral is the angle between  $\mathbf{P}$  and  $\mathbf{k}$ , we can see from both Fig. 4.10a and Fig. 4.10b that theta can always begin at  $0^\circ$ , as long as the conditions on  $P$  have been satisfied. Then, as the angle increases, it is possible depending the relative sizes of  $P$ ,  $k$ , and  $k_F$  that the vector  $2\mathbf{P} - \mathbf{k}$  could extend beyond the Fermi sphere. If  $k$  and  $P$  are sufficiently small, it is possible that  $2\mathbf{P} - \mathbf{k}$  will remain within the Fermi sphere for all angles  $\theta$ . This occurs whenever  $0 < 2P < k_F - k$ . Otherwise, the angles can increase until the points illustrated in Fig. 4.10, where  $\cos\theta = \frac{k^2 + 4P^2 - k_F^2}{4kP}$ . These limits can best be summarized as follows:

$$\begin{aligned} (\cos\theta)_{min} &= \begin{cases} -1 & \text{if } 0 < 2P \leq k_F - k, \\ \frac{k^2 + 4P^2 - k_F^2}{4kP} & \text{if } |k_F - k| < 2P \leq k_F + k, \end{cases} \\ (\cos\theta)_{max} &= 1 \quad \text{for all values of } P. \end{aligned} \tag{4.39}$$

Once these limits for the integrals are chosen for a particular value of  $k$ , we found that with a mesh using Gaussian quadrature, sixteen points for the integral over  $P$ , and ten points for the integral over  $\cos\theta$  were sufficiently stable numerically.



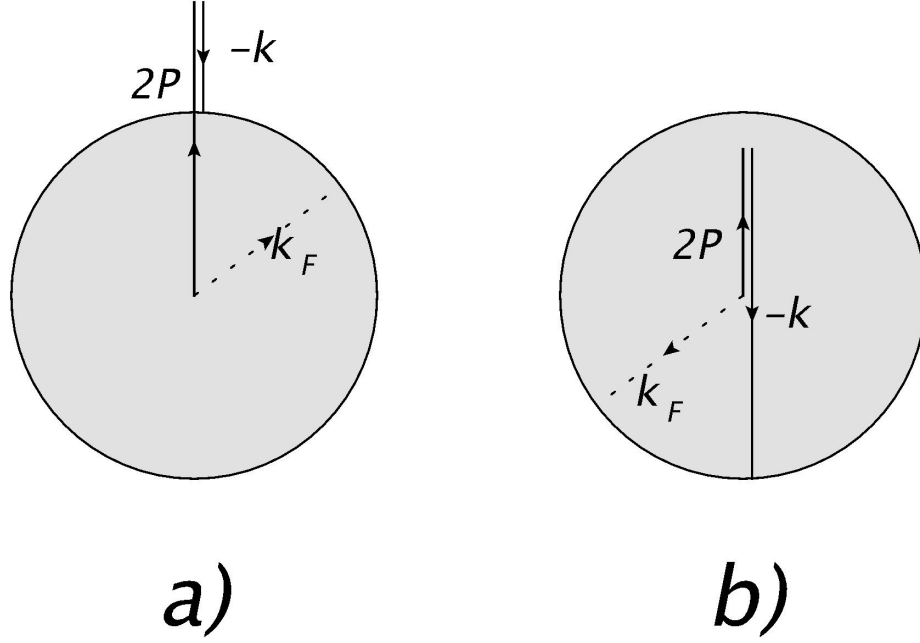


Figure 4.9: Fermi spheres of  $\theta(k_F - |2\mathbf{P} - \mathbf{k}|)$  in two separate cases. In sub-diagram a),  $k < k_F$ . in digram b),  $k > k_F$ .

Once the on-shell self-energy is properly calculated, we can compute the binding energy per nucleon  $E/A$  using Eq. (4.5). Reducing this integral to one dimension, and using for the density  $\rho = \frac{2k_F^3}{3\pi^2}$  we have ( $\hbar = 1$ )

$$\frac{E}{A} = \frac{2}{\rho} \int_0^{k_F} \frac{4\pi k^2 dk}{(2\pi)^3} \left( \frac{k^2}{2m} + \varepsilon(k) \right) = T_F + \frac{3}{2k_F^3} \int_0^{k_F} k^2 dk U_c(k) \quad (4.40)$$

where in the preceding,  $T_F \equiv \frac{3k_F^2}{10m}$  is the kinetic energy of the system of free nucleons.

## 4.4 Results

In order to verify the soundness of our numerical procedure, we first computed the binding energy per nucleon for the RSC in the continuous choice. We used the full continuous choice BHF procedure for partial waves with  $J \leq 2$ , and included higher partial waves (up to  $J = 7$ ) at the level of HF. Since the RSC was not fit to

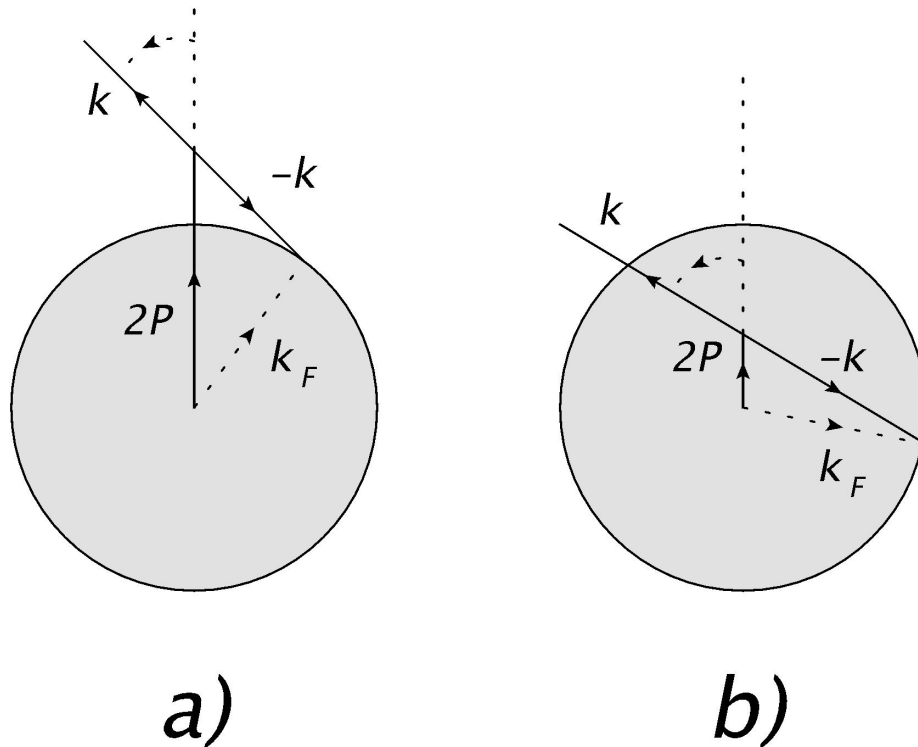


Figure 4.10: Fermi spheres of  $\theta(k_F - |2\mathbf{P} - \mathbf{k}|)$  in two separate cases. In sub-diagram a),  $2P > k_F$ . in digram b),  $2P < k_F$ .

such high partial waves, we used the extension of the RSC created by Ben Day [18] for  $J \geq 3$ . Table 4.1 compares the continuous-choice contributions to the binding energy at  $k_F = 1.36 fm^{-1}$  for each partial wave, to the gap-choice results of Haftel and Tabakin [33]. Both calculations use the RSC, but in the case of the gap choice calculation the authors used only pion exchange for partial waves higher than  $J = 2$ . Therefore we should expect some discrepancy for those partial waves even though both techniques use only the HF contribution.

Also displayed in the table are similar results for the AV14 potential [69] in both gap and continuous choice from [7]. In that work, Baldo *et al.* found that continuous choice calculations yield similar binding energies in all channels but the  $S$ -waves, and that in those channels (particularly the triplet  $S$ ) continuous choice calculations yield considerably more binding. Our results exhibit the same feature, and also agree

reasonably well with the continuous choice results of the AV14 for all channels but the  $^1P_1$ . An examination of modern fits to scattering data [60] quickly shows that the data available at the time of Reid’s initial fitting in that channel were of poor quality, so it is not surprising to find a discrepancy in this channel when the RSC is compared with a more modern potential fit to more modern data. Even so, we observe that in the  $^1P_1$  channel we see an increase in binding between gap choice and continuous choice of comparable size to the change found for the AV14.

It should be noted, however, that our binding energy is about 3 MeV greater at saturation than that cited by [21], who also use continuous choice with the RSC. In that calculation, the authors computed the  $G$ -matrix up to  $J = 3$  (as opposed to  $J = 2$  in our calculation), and only included partial waves up to  $J = 5$  at the level of HF (whereas we included partial waves up to  $J = 7$ ). It is not clear if these differences fully account for the discrepancy between these calculations, so this discrepancy still needs to be better understood. Nevertheless, there seems to be sufficient agreement with the AV14 results to proceed with a comparison between our dynamic potential and the static RSC at this level of approximation.

We now turn to the  $sp$  potentials generated at various densities. The rate of convergence can be seen in Fig. 4.11, where the input spectrum is depicted as a magenta dashed line, and successive iterations are plotted. For the input spectrum in this plot we used the self-consistent spectrum from a different density. After the fourth iteration the curves are visually indistinguishable on this scale, but in general as many as 12 iterations were necessary to achieve the desired precision in the binding energy.

Figure 4.12 compares the real parts of the on-shell static (black) and dynamic (red) self-energies for different densities. There are several important features to note here.

1. The general trend for all densities is that the dynamic self-energy is more attractive at low  $k$ , but becomes less attractive at higher  $k$ .
2. For lower densities (first three panels) the point where the two curves intersect lies above  $k_F$ , while for higher densities (last three panels) it lies below.

Table 4.1: The first column indicates the partial wave, while the remaining columns report the contribution to the binding energy from that partial wave, measured in MeV. The second and third columns report the results of the gap choice calculation of [33] and our own continuous choice calculation, both using the RSC. The last two columns reproduce the results of gap and continuous choice calculations of [7] for AV14.

	RSC Gap	RSC Cont.	AV14 Gap	AV14 Cont.
$^1S_0$	-15.57	-15.88	-16.31	-16.51
$^1P_1$	2.39	1.99	4.13	3.94
$^1D_2$	-2.55	-2.58	-2.84	-2.82
$^3P_0$	-3.32	-3.31	-3.83	-3.83
$^3P_1$	9.93	9.27	11.06	10.56
$^3D_2$	-4.32	-4.43	-4.16	-4.18
$^1F_3$	0.84	0.82	0.91	0.89
$^3F_3$	1.56	1.55	1.72	1.70
$^1G_4$	-0.47	-0.47	-0.48	-0.47
$^3G_4$	-0.72	-0.72	-0.77	-0.77
$^1H_5$	0.21	0.21		
$^3H_5$	0.33	0.34		
$^1I_6$	-0.11	-0.11		
$^3I_6$	-0.16	-0.14		
$^1J_7$	0.05	0.050		
$^3J_7$	0.08	0.074		
$^3S_1 + ^3D_1$	-13.71	-20.36	-15.54	-19.09
$^3P_2 + ^3F_2$	-7.60	-8.19	-7.60	-7.90
$^3D_3 + ^3G_3$	0.53	-0.04		
$^3F_4 + ^3H_4$	-0.30	-0.29		
$^3G_5 + ^3I_5$	0.13	0.13		

Table 4.2: Contributions to  $E/A$  at various densities for all partial waves with total angular momentum  $J \leq 2$ . This information is also broken down in terms of total spin and isospin combinations in Table 4.3 and displayed in Fig. 4.14.

$k_F = 1.00 fm^{-1}$	DR1	RSC	$k_F = 1.36 fm^{-1}$	DR1	RSC
$^1S_0$	-8.21	-8.97	$^1S_0$	-14.14	-15.88
$^1P_1$	-0.17	0.48	$^1P_1$	-0.1	1.99
$^1D_2$	-0.42	-0.66	$^1D_2$	-1.6	-2.58
$^3P_0$	-0.6	-1.36	$^3P_0$	-0.86	-3.31
$^3P_1$	1.55	2.85	$^3P_1$	4.45	9.27
$^3D_2$	-0.85	-1.21	$^3D_2$	-2.81	-4.43
$^3S_1 + ^3D_1$	-15.27	-14.77	$^3S_1 + ^3D_1$	-22.01	-20.36
$^3P_2 + ^3F_2$	-2	-2.25	$^3P_2 + ^3F_2$	-7.17	-8.19
$k_F = 1.46 fm^{-1}$	DR1	RSC	$k_F = 1.56 fm^{-1}$	DR1	RSC
$^1S_0$	-15.91	-18.03	$^1S_0$	-17.66	-20.18
$^1P_1$	0.16	2.82	$^1P_1$	0.62	3.92
$^1D_2$	-2.19	-3.5	$^1D_2$	-2.93	-4.62
$^3P_0$	-0.78	-3.96	$^3P_0$	-0.61	-4.6
$^3P_1$	5.75	12.14	$^3P_1$	7.39	15.6
$^3D_2$	-3.63	-5.84	$^3D_2$	-4.6	-7.49
$^3S_1 + ^3D_1$	-23.4	-21.66	$^3S_1 + ^3D_1$	-24.36	-22.59
$^3P_2 + ^3F_2$	-9.48	-10.82	$^3P_2 + ^3F_2$	-12.23	-13.94
$k_F = 1.66 fm^{-1}$	DR1	RSC	$k_F = 1.76 fm^{-1}$	DR1	RSC
$^1S_0$	-19.36	-22.2	$^1S_0$	-20.99	-24.15
$^1P_1$	1.36	5.39	$^1P_1$	2.44	7.23
$^1D_2$	-3.88	-5.97	$^1D_2$	-5.05	-7.59
$^3P_0$	-0.32	-5.32	$^3P_0$	8.81E-002	-5.88
$^3P_1$	9.44	19.9	$^3P_1$	12.02	24.76
$^3D_2$	-5.73	-9.47	$^3D_2$	-7.07	-11.69
$^3S_1 + ^3D_1$	-24.77	-23.78	$^3S_1 + ^3D_1$	-24.54	-23.7
$^3P_2 + ^3F_2$	-15.47	-17.69	$^3P_2 + ^3F_2$	-19.23	-21.93

Table 4.3: Contributions to  $E/A$  at various densities, broken down in terms of spin and isospin combinations. The differences between the contributions from the static potential and the dynamic potential for each spin-isospin combination are highlighted in red, indicating a systematic increase in the difference with increasing density. This information is also displayed in Fig. 4.14.

$k_F = 1.00 fm^{-1}$	T=0,S=0	T=0,S=1	T=1,S=0	T=1,S=1
Static (MeV)	0.48	-15.98	-9.63	-0.76
Dynamic (MeV)	-0.17	-16.12	-8.63	-1.05
Difference (MeV)	0.65	0.14	-1	0.29
$k_F = 1.36 fm^{-1}$	T=0,S=0	T=0,S=1	T=1,S=0	T=1,S=1
Static (MeV)	1.96	-24.79	-18.46	-2.23
Dynamic (MeV)	-0.08	-24.7	-15.77	-3.56
Difference (MeV)	2.04	-0.09	-2.69	1.33
$k_F = 1.46 fm^{-1}$	T=0,S=0	T=0,S=1	T=1,S=0	T=1,S=1
Static (MeV)	2.81	-27.63	-21.55	-2.65
Dynamic (MeV)	0.16	-27.03	-18.1	-4.51
Difference (MeV)	2.65	-0.6	-3.45	1.86
$k_F = 1.56 fm^{-1}$	T=0,S=0	T=0,S=1	T=1,S=0	T=1,S=1
Static (MeV)	3.92	-30.07	-24.80	-2.94
Dynamic (MeV)	0.62	-28.96	-20.59	-5.45
Difference (MeV)	3.3	-1.11	-4.21	2.51
$k_F = 1.66 fm^{-1}$	T=0,S=0	T=0,S=1	T=1,S=0	T=1,S=1
Static (MeV)	5.39	-33.25	-28.17	-3.11
Dynamic (MeV)	1.36	-30.50	-28.17	-6.36
Difference (MeV)	4.03	-2.75	-4.94	3.25
$k_F = 1.76 fm^{-1}$	T=0,S=0	T=0,S=1	T=1,S=0	T=1,S=1
Static (MeV)	7.23	-35.39	-31.74	-3.05
Dynamic (MeV)	2.45	-31.62	-26.04	-7.13
Difference (MeV)	4.78	-3.77	-5.7	4.08

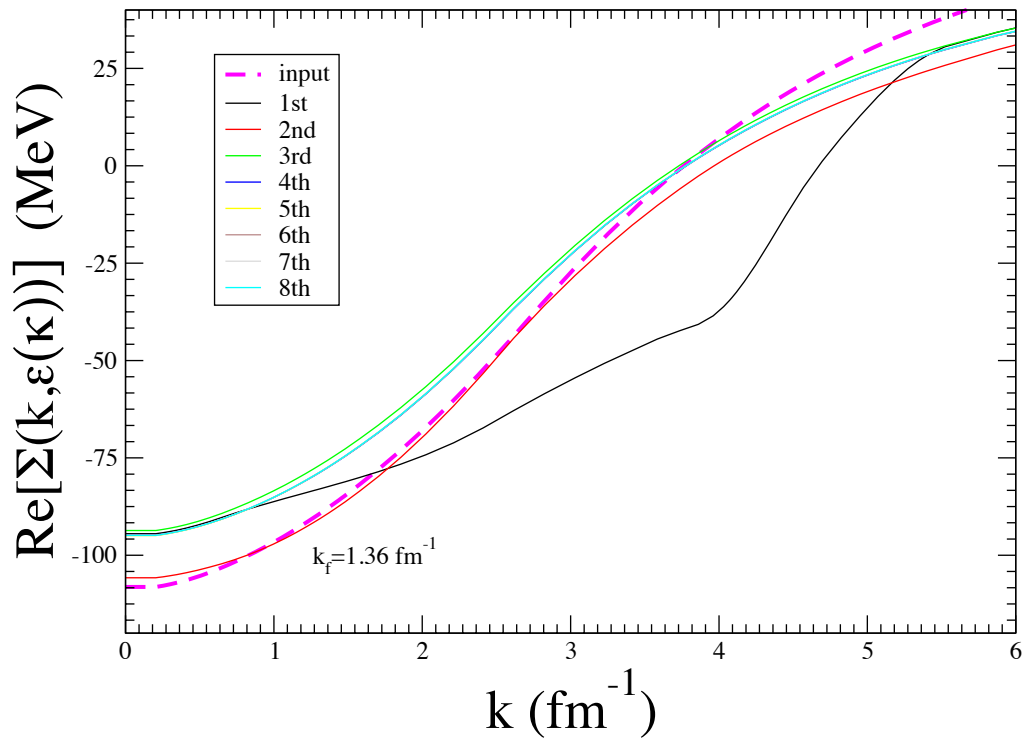


Figure 4.11: Real part of the on-shell self-energies for successive iterations in the case  $k_F = 1.36 \text{ fm}^{-1}$ . Input spectrum is dashed (magenta). Iterations 4-8 are visually indistinguishable on this scale.

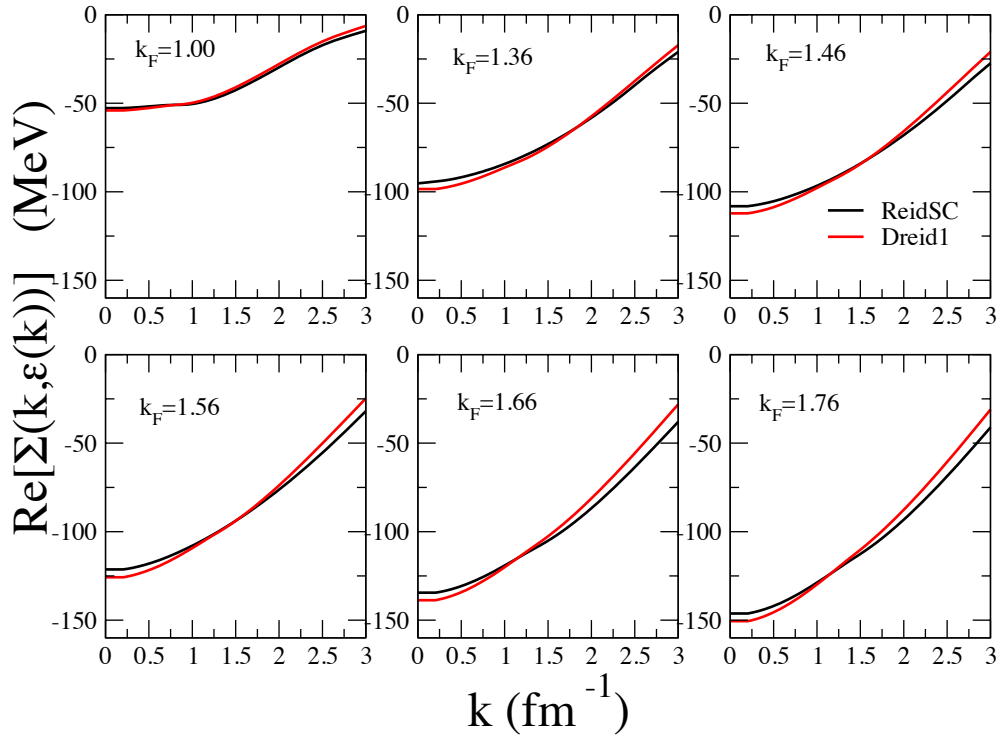


Figure 4.12: Real part of the on-shell self-energies for increasing  $k_F$ . Red is the spectrum formed using the DR1 potential, while black was obtained using the RSC. It can be seen that in general the dynamic self-energy is more attractive at low  $k$ , and less attractive at higher  $k$ .



3.  $E/A$  is only sensitive to the real part of the on-shell self-energy for values of  $k < k_F$ . This means that for densities for which the dynamic potential is more attractive than the static up to  $k = k_F$  the dynamic potential must lead to greater binding than the static.
4.  $E/A$  is most sensitive to the value of the self-energy near  $k_F$  due to the  $k^2$  weight in the integral in Eq. (4.40).
5. As density increases, the phase space wherein the dynamic self-energy is less attractive than the static also increases. Consequently it must be the case that at some density the dynamic potential energy contribution to the binding must be smaller than for the static interaction.

These factors ultimately lead to a shift to the left of the saturation curve, as illustrated in Fig. 4.13. The shift of the saturation curve toward the empirical region by roughly  $0.05 fm^{-1}$  is substantial and quite relevant to the discussion of the nuclear saturation problem in general. Because saturation density is proportional to  $k_F^3$ , a  $0.05 fm^{-1}$  reduction in Fermi momentum corresponds to roughly a 10% decrease in saturation density. Machleidt *et al.* also found a reduction of saturation density with their dynamic version of the Bonn potential, but with a concurrent reduction in binding energy that kept their saturation point on the Coester band [39]. Their method differed from ours in that they employ the standard choice for their  $sp$  spectrum, while we use the continuous choice.

Our result suggests that at a given level of approximation, replacement of a static  $NN$  interaction with a phase shift equivalent dynamic interaction within the continuous choice can move the saturation point off the Coester band toward the left, without a significant change in overall binding energy. Before drawing further conclusions, we will probe more deeply into the ingredients of this calculation to see if we can derive further insight into this change in the saturation mechanism.

We begin with an examination of the contributions to overall binding energy from each partial wave. In Tables 4.2 and 4.3 we have tabulated the total potential energy contribution for partial waves with  $J \leq 2$  to the binding energy for each value of  $k_F$ . In the former, the information is broken down to display the contribution from each partial wave. It is very interesting to note that the drastic changes in

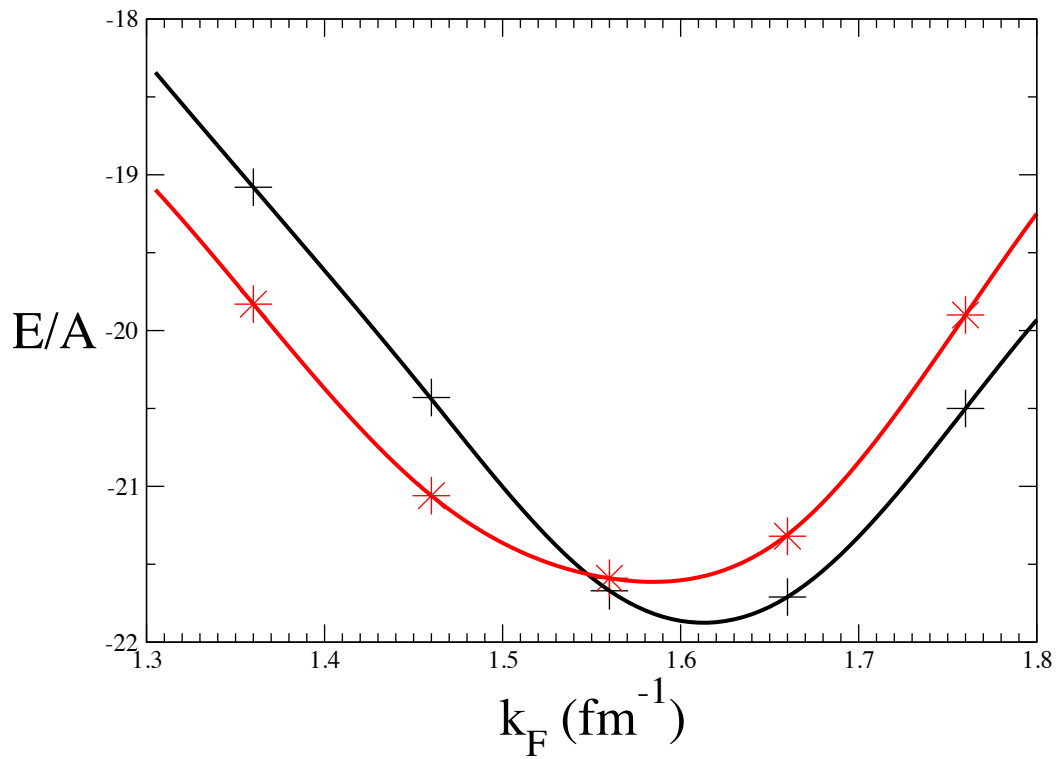


Figure 4.13: Saturation curves for DR1 (red) and RSC (black). Red stars are calculated binding energies for DR1. Black pluses are calculated binding energies for RSC. Curves are cubic spline interpolation.

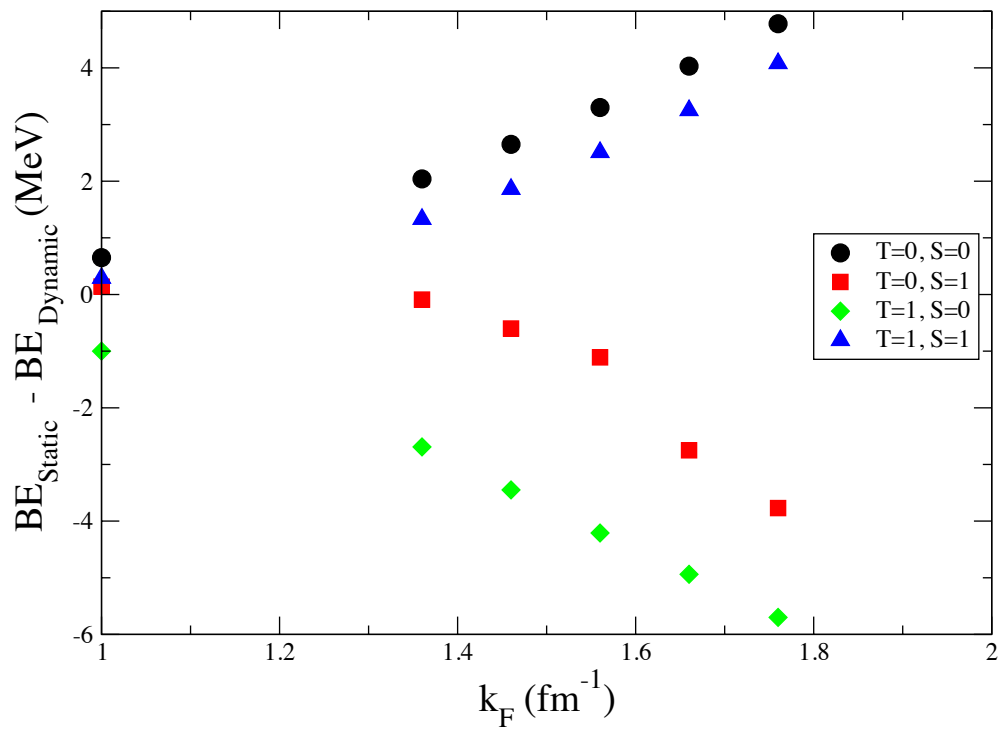


Figure 4.14: Difference between potential energy contributions to binding energy of the static and the dynamic cases.

the contributions to binding are not limited to the  $S$ -waves. There are substantial changes to the binding energy contributions seen also in both the  $L = 1$  and  $L = 2$  channels, yet the overall binding is only slightly changed. How this transpires can be seen by examining Table 4.3 and Fig. 4.14 where the contributions are broken down in terms of the various combinations of total spin and isospin. In the Table 4.3 we highlight (in red) the difference between the static and dynamic contributions at each density.

Several trends are clear from these tables. Table 4.2 in particular makes clear in particular that for both the strong tensor force in the  ${}^3S_1 - {}^3D_1$  channel and the attractive  ${}^1S_0$  channel, the contributions from the dynamic interaction becomes considerably less attractive than the static contributions as density increases. This will reduce the density range over which pairing occurs in these channels, as well as reducing the gaps necessary for dealing with them.

Additionally, a general trend for the differences between the contributions from the RSC and the DR1, illustrated in Fig. 4.14 and quantified in Table 4.3, is that for odd- $L$  channels ( $T = 0, S = 0$  and  $T = 1, S = 1$ ) the difference is positive and grows with increasing density, while for even- $L$  channels ( $T = 0, S = 1$  and  $T = 1, S = 0$ ) the difference is negative but grows in magnitude at roughly the same rate. For three of the channels, the trend is strongly linear for the five highest Fermi momenta, while for the fourth ( $T = 0, S = 1$ ) it is not quite linear. The alternating sign of the difference corresponds to the signs of the  $\sigma_1 \cdot \sigma_2 \tau_1 \cdot \tau_2$  term in the OPEP (Eq. (2.22)). Explicitly,

$$\begin{aligned}
 \sigma_1 \cdot \sigma_2 \tau_1 \cdot \tau_2 &= 9 && \text{if } T = 0, S = 0 \\
 \sigma_1 \cdot \sigma_2 \tau_1 \cdot \tau_2 &= -3 && \text{if } T = 0, S = 1 \\
 \sigma_1 \cdot \sigma_2 \tau_1 \cdot \tau_2 &= -3 && \text{if } T = 1, S = 0 \\
 \sigma_1 \cdot \sigma_2 \tau_1 \cdot \tau_2 &= 1 && \text{if } T = 1, S = 1,
 \end{aligned}$$

further clarifying and confirming the systematic nature of the replacement of a static treatment of the OPEP with a dynamic one.

It is the near equality in the magnitudes of the slopes (but opposite signs) in Fig. 4.14 of the odd- $L$  and even- $L$  cases that is responsible for the (near) lack of

change to the overall binding energy at the corresponding saturation density despite the fact that the individual contributions differ greatly at higher density. It is the downturn in the difference for the  $(T = 0, S = 1)$  partial waves that leads to a change in the total difference, and consequently is responsible for the shift to the left of the saturation curve.

The fact that the  $T = 0, S = 1$  partial waves do not quite fit this linear trend is not so surprising since this is where the strong  ${}^3S_1 - {}^3D_1$  tensor force occurs. In the density range we consider there is likely a pairing solution in the  ${}^3S_1 - {}^3D_1$  channel [67]. It is also expected that there is a pairing solution in the  ${}^1S_0$  channel  $(T = 1, S = 0)$  for the lowest density point, but not for the higher densities. Because of the different attraction of the dynamic self-energy in these channels we expect that handling these pairing solutions will require a larger gap for the  ${}^3S_1 - {}^3D_1$  channel and a smaller gap for the  ${}^1S_0$  channel.

It is clear that at the BHF level of approximation, including dynamic propagation of pions in the continuous choice has a significant influence on the saturation properties of nuclear matter. It provides a needed shift away from the Coester band and toward the empirical region for a Reid-like dynamic interaction. Potential future exploration of this effect will be discussed in more detail in Chapter 5.

# Chapter 5

## Conclusion and Outlook

To date, all of the realistic  $NN$  interactions that are widely used contain static pion exchange. For most applications this has been sufficient. The reasons for the appeal of the static pion are manifold. From a computational point of view, the static pion contains no pole above the pion-production threshold and is therefore easy to control numerically. Static pions and dynamic pions agree on-shell, and only on-shell  $\mathcal{T}$ -matrix elements are needed to fit the potential to phase shifts. With a static pion one need not worry about evaluating two-pion in flight diagrams. However, with all of these virtues, we have demonstrated that it is possible to overcome the same difficulties, albeit with more effort, with dynamic pions. Furthermore, there are some applications where the off-shell behavior of the relevant scattering matrix becomes important. We have demonstrated that there is reason to believe that a dynamic pion might be better suited toward a description of the data in those applications.

We have developed a potential for testing the consequences of allowing pions to carry energy. This potential is no toy model, and because of its harder core compared to more modern potentials might have the same continuing usefulness as the Reid potential does in many-body calculations. We have also demonstrated that it should be possible to obtain a fit to more modern data, but to do this with the same quality as currently used potentials is a large-scale project beyond the scope of this work. It is our hope that this better fit occur in the future; an update akin to the Reid93 and one which can act as a foil to the modern potentials as our own model has done for the Reid. We have offered a prescription for replacing static pions with dynamic ones,

both above and below pion-production threshold, which could easily be inserted into any of these modern potentials.

We have also argued that inelastic scattering data, such as the polarization observable  $A_y$ , might be better analyzed with dynamic potentials. Although our model was not able to explain the  $A_y$  puzzle presented by Noro [49], we did clarify some aspects of it. We note that  $A_y$  is very sensitive to the Coulomb force, and some of the decrease in  $A_y$  with increasing separation energy could be related to the increasing nuclear charge which our model cannot address. We propose that future efforts with dynamic pions should be fit to modern  $pp$  data as well as  $np$  data, and the Coulomb force taken into account. It might also be necessary to make higher-mass terms dynamic, since these are primarily responsible for the two-body spin-orbit interaction. Toward both of these ends a suitable candidate potential for the inclusion of dynamic meson exchange is the CDBonn interaction, which contains both explicit meson exchange and the Coulomb force. We are forced to admit, however, that it is possible that the resolution to this puzzle lies elsewhere. Nevertheless, from a formal standpoint a dynamic interaction seems more suitable to this class of experiments and should be explored further. It is also very important that the  $NN$  interaction be clarified and any remaining puzzles solved, so that we have a cleaner analysis of the important  $(p, 2p)$  experiments that are only recently possible in inverse kinematics with unstable beams.

We have also made an interesting discovery toward the clarification of the nuclear-matter saturation problem. The difficulty in simultaneously predicting the proper binding energy per nucleon and saturation density of nuclear matter has over the last several decades assumed almost mythic proportions. Although much work has been done in the area, and there are several approaches which are able to come close to the mark, a full understanding of the underlying saturation mechanism has not yet been achieved. We offer only a modest contribution to this understanding, but hope that our work combined with the gargantuan efforts that have gone before can bring us closer to that deep understanding. Our results suggest that the presence of propagating pions in the medium, at the level studied here, effects a global shift in the density dependence of the binding energy. It reduces the Fermi momentum of the saturation point by about  $0.05 fm^{-1}$  toward the empirical saturation point,

resulting in a 10% decrease in saturation density, without significantly altering the binding energy per nucleon. As Dewulf *et al.* have recently argued [21], the manner of treatment of pions in many-body calculations seems central to the nuclear-matter saturation problem. The authors achieve reasonable binding with Fermi momentum at saturation density a little (roughly  $0.1fm^{-1}$ ) too high (see Fig 4.3) by excluding collective pionic modes, while including short-range correlations self-consistently. It will be very interesting to see how those results are altered with the inclusion of dynamic pions.

Additionally, it is interesting to note that in the  $T = 1$  channels, our dynamic interaction becomes more attractive (on the order of 1-2 MeV/nucleon) as a function of density than the static Reid. This indicates that in pure neutron matter the dynamic propagation of pions most likely leads a somewhat softer equation of state and therefore an altered density dependence of the symmetry energy. If this is borne out by further calculations in asymmetric nuclear matter it would also indicate that dynamic pion propagation moves the neutron drip line away from the valley of stability.

We have demonstrated that a systematic treatment of dynamic pion propagation is not only possible, but of potential interest in the future study of inelastic scattering as well as nuclear-matter properties. Pions *do* carry energy in certain applications, and it is reasonable to include these dynamic effects from the beginning during the construction of  $NN$  potentials. We have provided a prescription for their inclusion in any  $NN$  interaction which already includes static pions, as well as an analysis of when such inclusion might exhibit interesting results. We hope that this work can be of use to others in future studies.



# Appendix A

## Potential Parameters

### A.1 Reid soft-core potential

For reference we reproduce here the functional form of the RSC [54]. The  $T=1$  channels for  $J \leq 2$  are given below.

$$V(^1S_0) = -h \frac{e^{-x}}{x} - 1650.6 \frac{e^{-4x}}{x} + 6484.2 \frac{e^{-7x}}{x} \quad (\text{A.1})$$

$$V(^1D_2) = -h \frac{e^{-x}}{x} - 12.322 \frac{e^{-2x}}{x} - 1112.6 \frac{e^{-4x}}{x} + 6484.2 \frac{e^{-7x}}{x} \quad (\text{A.2})$$

$$V(^3P_0) = -h \left[ \left( 1 + \frac{4}{x} + \frac{4}{x^2} \right) \frac{e^{-x}}{x} - \left( \frac{16}{x} + \frac{4}{x^2} \right) \frac{e^{-4x}}{x} \right] + 27.133 \frac{e^{-2x}}{x} - 790.74 \frac{e^{-4x}}{x} + 20662 \frac{e^{-7x}}{x} \quad (\text{A.3})$$

$$V(^3P_1) = h \left[ \left( 1 + \frac{2}{x} + \frac{2}{x^2} \right) \frac{e^{-x}}{x} - \left( \frac{8}{x} + \frac{2}{x^2} \right) \frac{e^{-4x}}{x} \right] - 135.25 \frac{e^{-2x}}{x} + 472.81 \frac{e^{-3x}}{x} \quad (\text{A.4})$$

$$V(^3P_2 - ^3F_2) = V_C + V_T S_{12} + V_{LS} \mathbf{L} \cdot \mathbf{S} \quad (\text{A.5})$$

where

$$V_C = \frac{h}{3} \frac{e^{-x}}{x} - 933.48 \frac{e^{-4x}}{x} + 4152.1 \frac{e^{-6x}}{x} \quad (\text{A.6})$$

$$V_T = h \left[ \left( \frac{1}{3} + \frac{1}{x} + \frac{1}{x^2} \right) \frac{e^{-x}}{x} - \left( \frac{4}{x} + \frac{1}{x^2} \right) \frac{e^{-4x}}{x} \right] - 34.925 \frac{e^{-3x}}{x} \quad (\text{A.7})$$

$$V_{LS} = -2074.1 \frac{e^{-6x}}{x}. \quad (\text{A.8})$$

The  $T=0$  channels for  $J \leq 2$  are given below.

$$V(^1P_1) = 3h \frac{e^{-x}}{x} - 634.39 \frac{e^{-2x}}{x} + 2163.4 \frac{e^{-3x}}{x} \quad (\text{A.9})$$

$$V(^3D_2) = -3h \left[ \left( 1 + \frac{2}{x} + \frac{2}{x^2} \right) \frac{e^{-x}}{x} - \left( \frac{8}{x} + \frac{2}{x^2} \right) \frac{e^{-4x}}{x} \right] - 220.12 \frac{e^{-2x}}{x} + 871 \frac{e^{-3x}}{x} \quad (\text{A.10})$$

$$V(^3S_1 - ^3D_1) = V_C + V_T S_{12} + V_{LS} \mathbf{L} \cdot \mathbf{S} \quad (\text{A.11})$$

where

$$V_C = h \frac{e^{-x}}{x} + 105.468 \frac{e^{-2x}}{x} - 3187.8 \frac{e^{-4x}}{x} + 9924.3 \frac{e^{-6x}}{x} \quad (\text{A.12})$$

$$V_T = -h \left[ \left( 1 + \frac{3}{x} + \frac{3}{x^2} \right) \frac{e^{-x}}{x} - \left( \frac{12}{x} + \frac{3}{x^2} \right) \frac{e^{-4x}}{x} \right] + 351.77 \frac{e^{-4x}}{x} - 1673.5 \frac{e^{-6x}}{x} \quad (\text{A.13})$$

$$V_{LS} = 708.91 \frac{e^{-4x}}{x} - 2713.1 \frac{e^{-6x}}{x}. \quad (\text{A.14})$$

## A.2 Dynamic Reid 1(DR1) refit parameters

Our potential is given with the pion piece provided by our Extended Legendre Function in momentum space. Here the  $\tilde{V}_\pi$  indicates schematically the position space version of our dynamic pion potential. It is the static higher-mass Yukawa terms that

are of importance here. We can compare the parameters in this refit to the parameters in the phenomenological multiple-pion exchange terms in the RSC, to gauge the effect in position space of the dynamic pion on the potential.

The  $T=1$  channels for  $J \leq 2$  are given below.

$$\tilde{V}(^1S_0) = \tilde{V}_\pi - 1666.0 \frac{e^{-4x}}{x} + 6494.2 \frac{e^{-7x}}{x} \quad (\text{A.15})$$

$$\tilde{V}(^1D_2) = \tilde{V}_\pi - 12.322 \frac{e^{-2x}}{x} - 1112.6 \frac{e^{-4x}}{x} + 6484.2 \frac{e^{-7x}}{x} \quad (\text{A.16})$$

$$\tilde{V}(^3P_0) = \tilde{V}_\pi + 128.04 \frac{e^{-2x}}{x} - 3225.9 \frac{e^{-4x}}{x} + 43994 \frac{e^{-7x}}{x} \quad (\text{A.17})$$

$$\tilde{V}(^3P_1) = \tilde{V}_\pi - 130.27 \frac{e^{-2x}}{x} + 391.09 \frac{e^{-3x}}{x} \quad (\text{A.18})$$

$$\tilde{V}(^3P_2 - ^3F_2) = \tilde{V}_C + \tilde{V}_T S_{12} + \tilde{V}_{LS} \mathbf{L} \cdot \mathbf{S} \quad (\text{A.19})$$

where

$$\tilde{V}_C = \tilde{V}_\pi - 949.64 \frac{e^{-4x}}{x} + 4133.1 \frac{e^{-6x}}{x} \quad (\text{A.20})$$

$$\tilde{V}_T = \tilde{V}_\pi - 36.458 \frac{e^{-3x}}{x} \quad (\text{A.21})$$

$$\tilde{V}_{LS} = -2074.1 \frac{e^{-6x}}{x}. \quad (\text{A.22})$$

The  $T=0$  channels for  $J \leq 2$  are given below.

$$\tilde{V}(^1P_1) = \tilde{V}_\pi - 665.71 \frac{e^{-2x}}{x} + 2157.9 \frac{e^{-3x}}{x} \quad (\text{A.23})$$

$$\tilde{V}(^3D_2) = \tilde{V}_\pi - 387.89 \frac{e^{-2x}}{x} + 1286 \frac{e^{-3x}}{x} \quad (\text{A.24})$$

$$\tilde{V}(^3S_1 - ^3D_1) = \tilde{V}_C + \tilde{V}_T S_{12} + \tilde{V}_{LS} \mathbf{L} \cdot \mathbf{S} \quad (\text{A.25})$$

where

$$\tilde{V}_C = \tilde{V}_\pi - 13.298 \frac{e^{-2x}}{x} - 2700.1 \frac{e^{-4x}}{x} + 9957.8 \frac{e^{-6x}}{x} \quad (\text{A.26})$$

$$\tilde{V}_T = \tilde{V}_\pi + 351.77 \frac{e^{-4x}}{x} - 1551.7 \frac{e^{-6x}}{x} \quad (\text{A.27})$$

$$\tilde{V}_{LS} = 708.91 \frac{e^{-4x}}{x} - 2713.1 \frac{e^{-6x}}{x}. \quad (\text{A.28})$$

### A.3 Dynamic Reid 1 plots

These plots were presented in Ch. 2 in a single 12-panel, and are here presented in larger form for closer inspection.

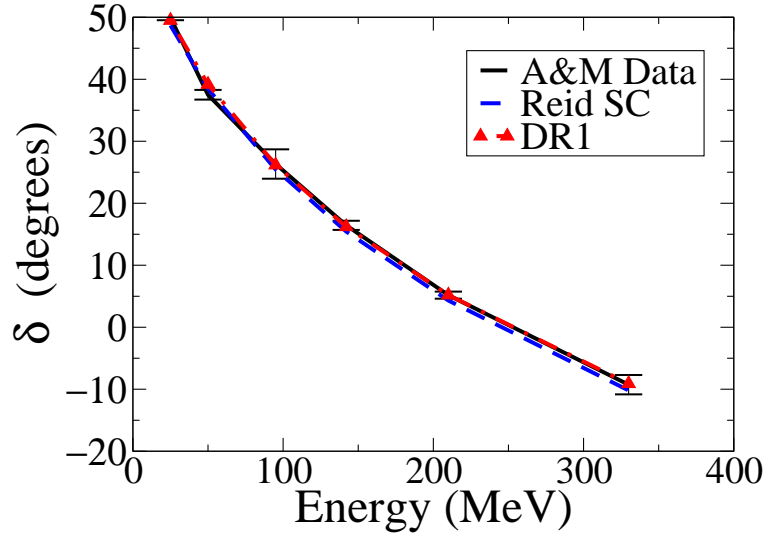


Figure A.1: Plot of RSC and DR1  $^1S_0$  phase shifts. Black error bars are from the original analysis of Arndt and MacGregor. Dashed (blue) curve is Reid's fit. Red dash-dotted line is the DR1 refit.

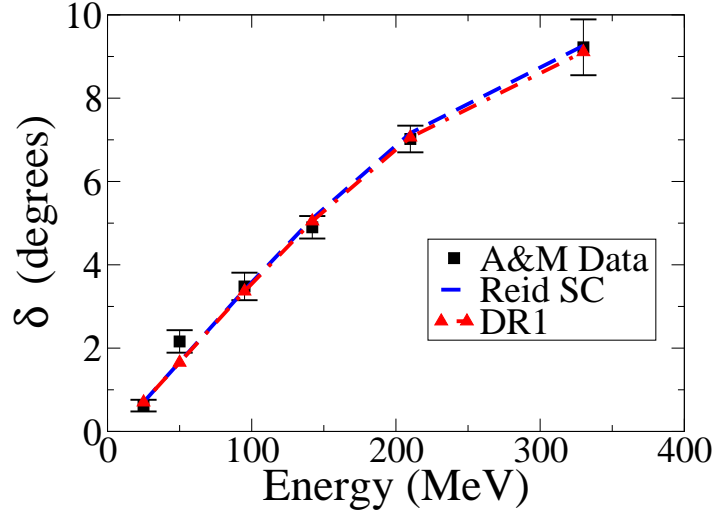


Figure A.2: Plot of RSC and DR1  $^1D_2$  phase shifts. Lines are as in Fig. A.1.

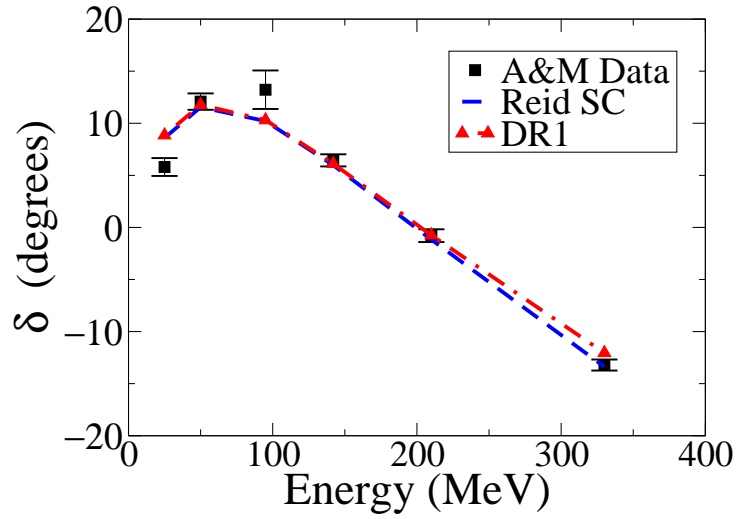


Figure A.3: Plot of RSC and DR1  $^3P_0$  phase shifts. Lines are as in Fig. A.1.

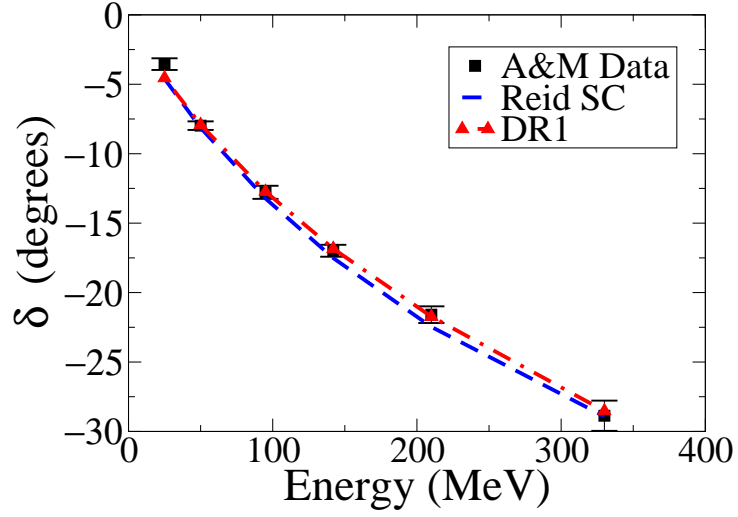


Figure A.4: Plot of RSC and DR1  ${}^3P_1$  phase shifts. Lines are as in Fig. A.1.

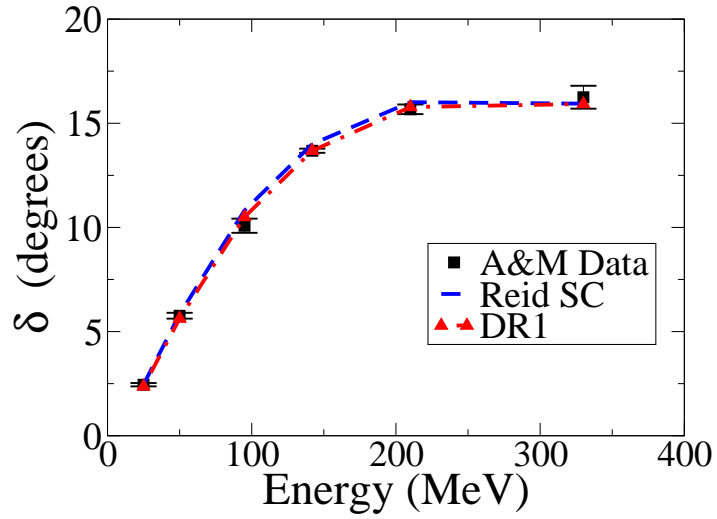


Figure A.5: Plot of RSC and DR1  ${}^3P_2$  phase shifts. Lines are as in Fig. A.1.

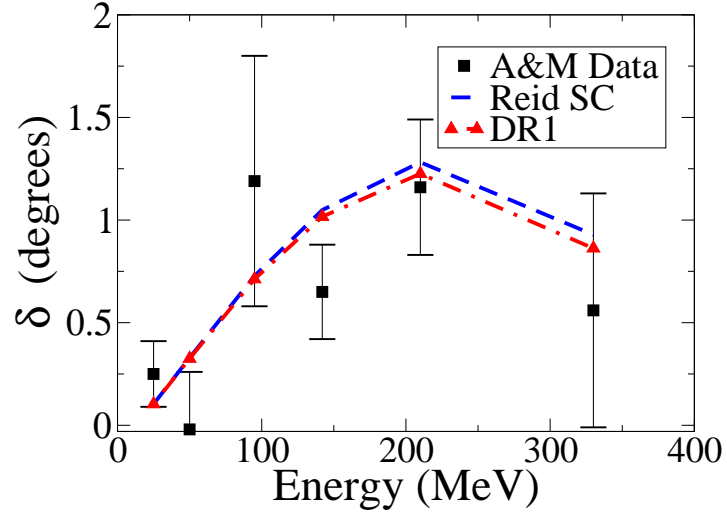


Figure A.6: Plot of RSC and DR1  ${}^3F_2$  phase shifts. Lines are as in Fig. A.1.

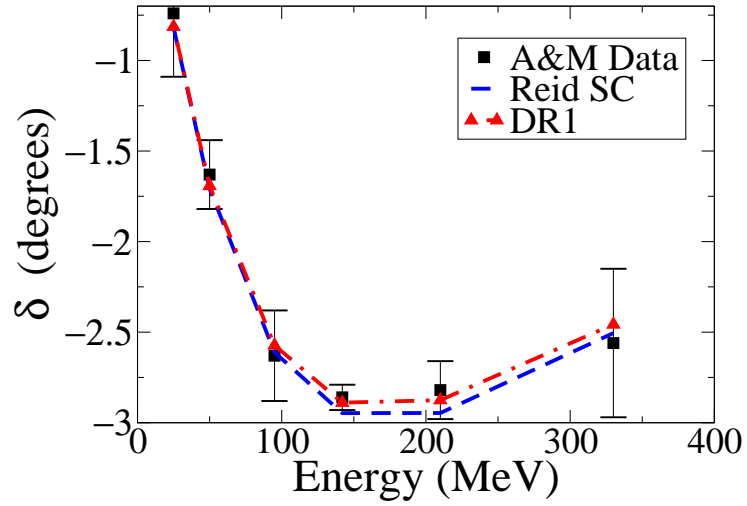


Figure A.7: Plot of RSC and DR1  $\epsilon_2$  mixing angles. Lines are as in Fig. A.1.

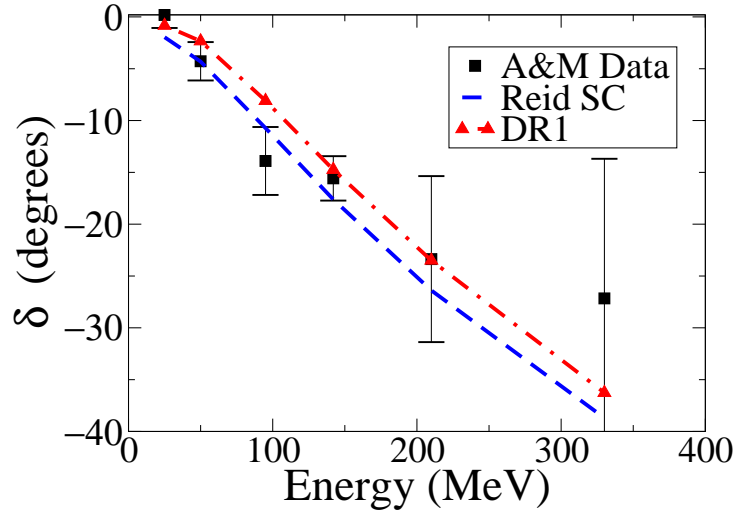


Figure A.8: Plot of RSC and DR1  $^1P_1$  phase shifts. Lines are as in Fig. A.1.

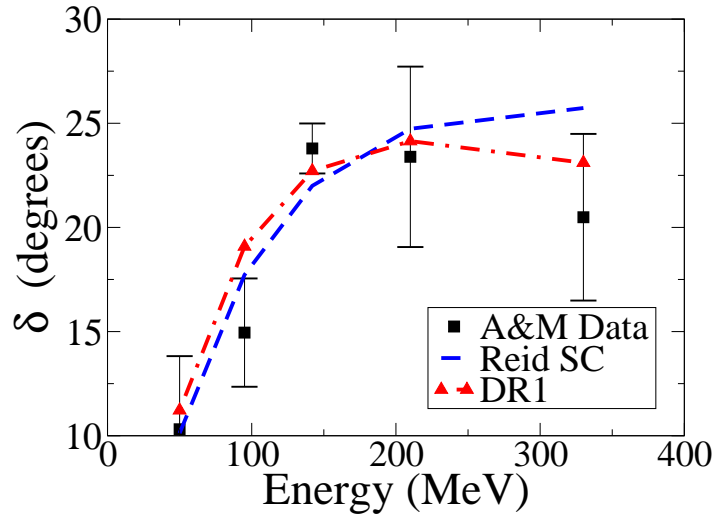


Figure A.9: Plot of RSC and DR1  $^3D_2$  phase shifts. Lines are as in Fig. A.1.



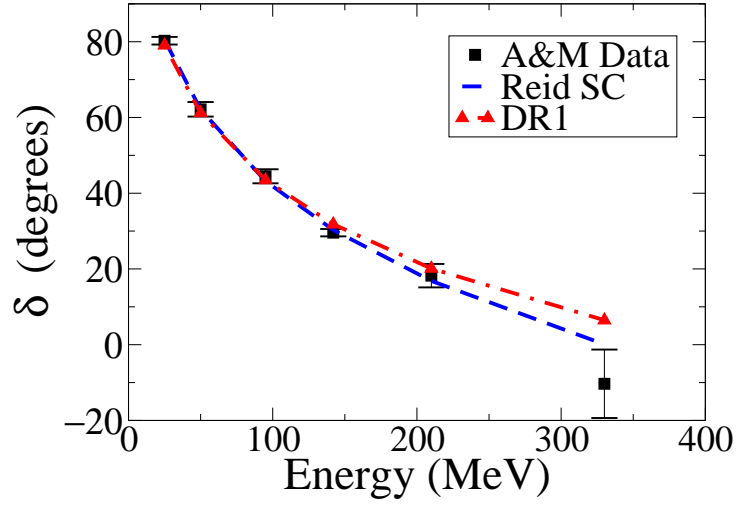


Figure A.10: Plot of RSC and DR1  $^3S_1$  phase shifts. Lines are as in Fig. A.1.

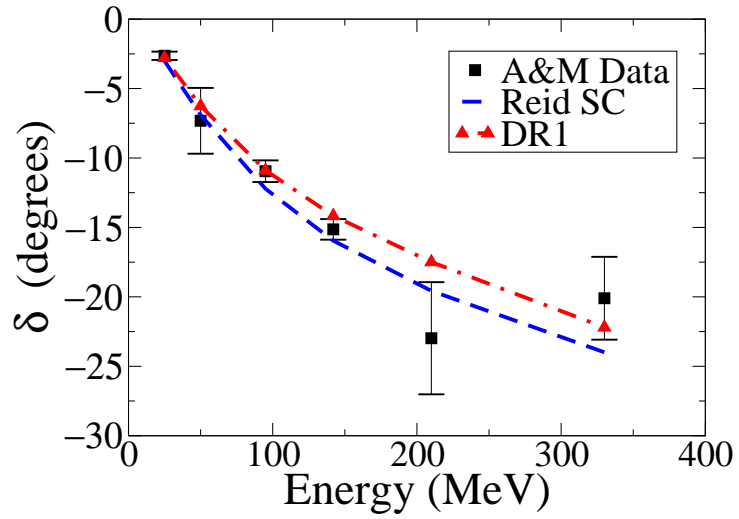


Figure A.11: Plot of RSC and DR1  $^3D_1$  phase shifts. Lines are as in Fig. A.1.

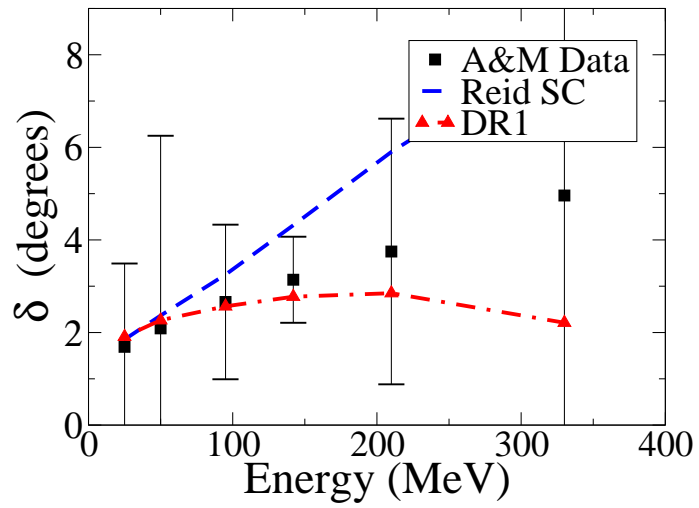


Figure A.12: Plot of RSC and DR1  $\epsilon_1$  mixing angles. Lines are as in Fig. A.1.

## A.4 Dynamic Reid 2 (DR2) plots

The following plots represent our best qualitative fit to the Nijmegen Partial Wave analysis [60]. This partial-wave analysis did not contain error bars in the isovector channel, so we present these only as a qualitative illustration of the possibility of obtaining a fit to the data of similar quality to the PWA and the various potentials of the Nijmegen group. These plots should demonstrate the plausibility of constructing a high quality realistic dynamic potential by including electromagnetic terms and fitting directly to modern data. Although these plots were presented in Ch. 2 in a single 7-panel plot, they are here reproduced in larger form for closer inspection.

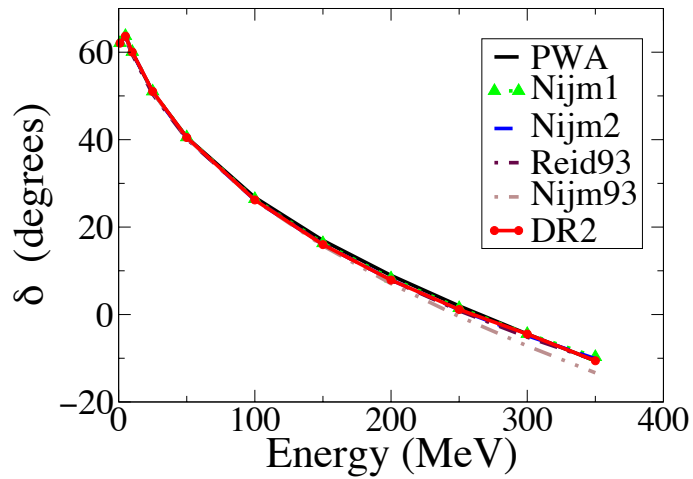


Figure A.13: Plot of DR2 fit to partial-wave analysis  $^1S_0$  phase shifts. Solid black line is the PWA. DR2 is solid red line, while the other curves for comparison are Nijm 1 (green dots), Nijm 2 (blue dashes), Reid 93 (purple dash-dot-dots), and Nijm 93 (tan dash-dots).

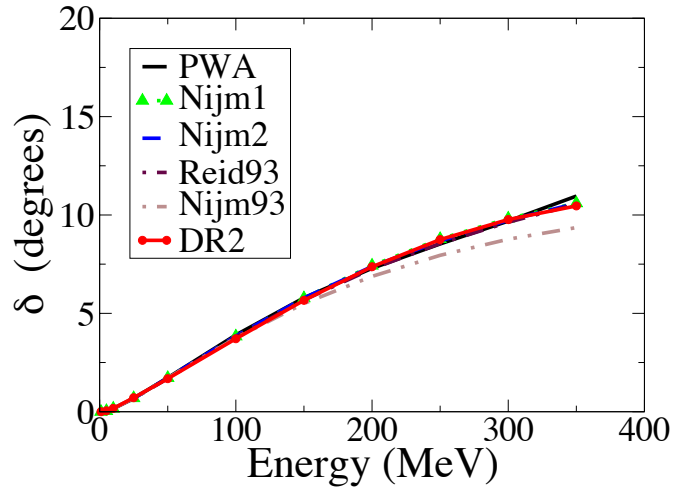


Figure A.14: Plot of DR2 fit to partial-wave analysis  $^1D_2$  phase shifts. Curves as labeled in Fig A.13.

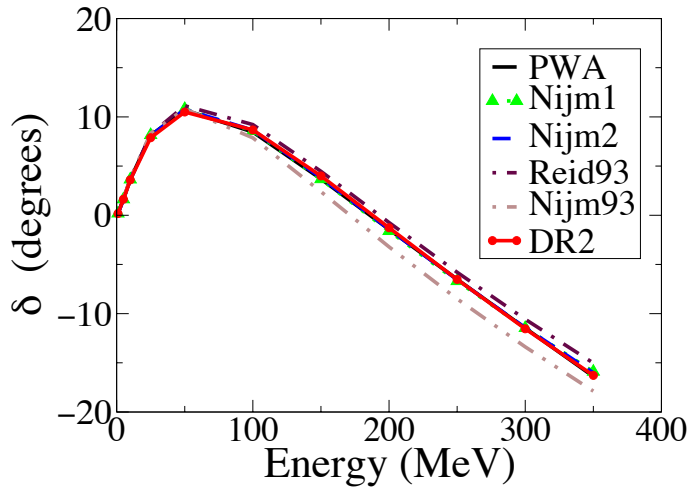


Figure A.15: Plot of DR2 fit to partial-wave analysis  $^3P_0$  phase shifts. Curves as labeled in Fig A.13.

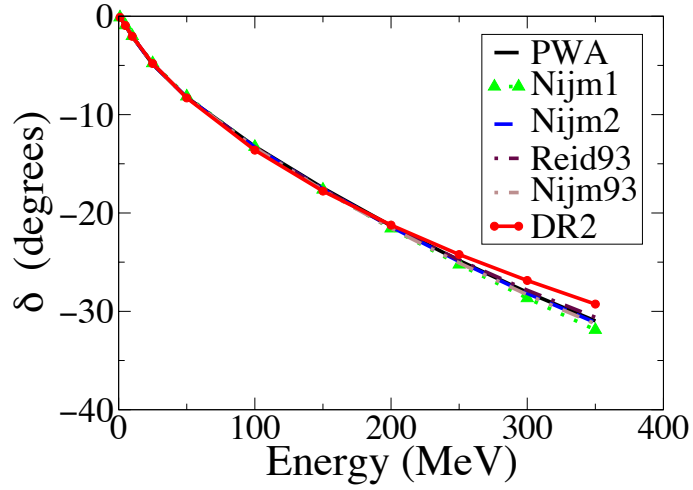


Figure A.16: Plot of DR2 fit to partial-wave analysis  ${}^3P_1$  phase shifts. Curves as labeled in Fig A.13.

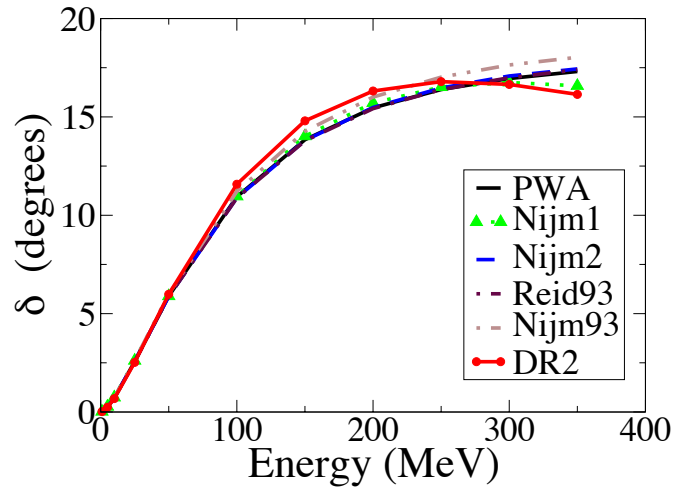


Figure A.17: Plot of DR2 fit to partial-wave analysis  ${}^3P_2$  phase shifts. Curves as labeled in Fig A.13.

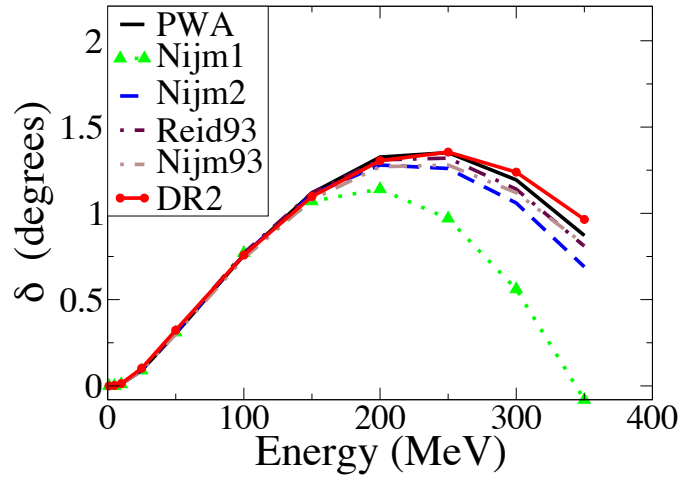


Figure A.18: Plot of DR2 fit to partial-wave analysis  ${}^3F_2$  phase shifts. Curves as labeled in Fig A.13.

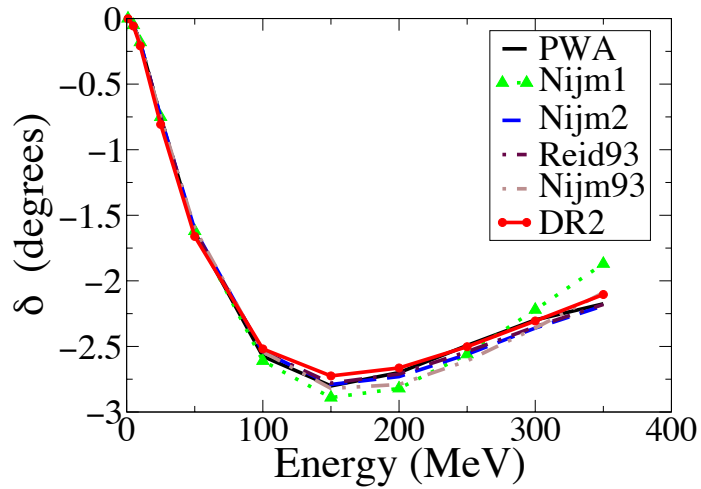


Figure A.19: Plot of DR2 fit to partial-wave analysis  $\epsilon_2$  mixing angles. Curves as labeled in Fig A.13.

# Appendix B

## $G$ -Matrix Coupled Channels

Here we present the details for full (on- and off-shell) calculation of both the real and imaginary parts of the coupled-channel Bruekner  $G$ -matrix. These details can also be found in more concise but equivalent form in Ref. [64]. We provide this alternative which has the advantage of separating  $G$  into real and imaginary parts. The coupled channels differ from the single channels mainly in that for a given set of quantum numbers  $(k_r, k'_r, K, E)$ , there is an additional sum over angular momentum states  $L = \{J - 1, J + 1\}$ . We begin by writing the equation for the coupled channel  $R$ -matrix, in analogy with Eq. (4.23).

$$R_{LL'} = V_{LL'} + \sum_{L''} V_{LL''} \mathcal{P} \frac{\bar{Q}_{pp}}{E - \varepsilon} R_{L''L}. \quad (\text{B.1})$$

The only thing here that is different from Eq. (4.23) is the sum over  $L''$ , which creates a 2x2 matrix equation for each set of  $(k_r, k'_r, K, E)$ .

In order to explore the (2x2) matrix nature of the coupled channel  $R$  and  $G$ -matrix equations, we simplify the notation as much as possible. Consequently, we write terms such as e.g.  $R_{J+1, J-1}(k_r, k'_r, K, E)$  with the simplified notation  $R_{+-}^{12}$ . This allows us to write the 2x2 (in angular momentum space)  $R$ -matrix more succinctly, as follows.

$$\begin{bmatrix} R_{--}^{12} & R_{-+}^{12} \\ R_{+-}^{12} & R_{++}^{12} \end{bmatrix} \equiv \begin{bmatrix} R_{J-1, J-1}(k_r, k'_r, K, E) & R_{J-1, J+1}(k_r, k'_r, K, E) \\ R_{J+1, J-1}(k_r, k'_r, K, E) & R_{J+1, J+1}(k_r, k'_r, K, E) \end{bmatrix} \quad (\text{B.2})$$



In this definition, a lower index of (+) indicates an angular momentum state  $L = J + 1$ , while a (-) indicates the  $L = J - 1$  state. Upper indices of (1) and (2) indicate momentum states ( $k_r$ ) and ( $k'_r$ ) respectively. Since the ensuing 2x2 matrix equation must be solved for each (K,E) independently, we suppress those variables. Finally, for the on-shell or half on-shell  $R$ -matrix elements, where one or both respectively of the  $k_r, k'_r$  are replaced by the value of relative momentum at the pole  $k_p$ , we will use an upper index of (p) where a “p” in the first slot indicates that  $k_r = k_p$  and a “p” in the second slot indicates that  $k'_r = k_p$ . This means that for example,  $R_{J+1, J-1}(k_r, k_p, K, E)$  will be written as  $R_{+-}^{1p}$ , while  $R_{J+1, J-1}(k_p, k'_r, K, E)$  would be written as  $R_{+-}^{p2}$  *etc.* All of these notational introductions are necessary so that we can express the rather lengthy matrix equations to follow in a minimum of space. Similar notational changes will apply to elements of the coupled channel  $G$ -matrix also.

With these notational changes in mind, we begin by writing the 2x2 matrix equation for the coupled channel  $R$ -matrix,

$$\begin{bmatrix} R_{--}^{12} & R_{-+}^{12} \\ R_{+-}^{12} & R_{++}^{12} \end{bmatrix} = \begin{bmatrix} V_{--}^{12} & V_{-+}^{12} \\ V_{+-}^{12} & V_{++}^{12} \end{bmatrix} + \mathcal{P} \frac{\bar{Q}_{pp}}{E - \varepsilon} \begin{bmatrix} V_{--}^{1p} & V_{-+}^{1p} \\ V_{+-}^{1p} & V_{++}^{1p} \end{bmatrix} \begin{bmatrix} R_{--}^{p2} & R_{-+}^{p2} \\ R_{+-}^{p2} & R_{++}^{p2} \end{bmatrix} \quad (\text{B.3})$$

which can be solved by matrix inversion in a manner analagous to the single channel case seen in Eqs. (4.24-4.26). Once we have solved for the full  $R$ -matrix, taking care to solve also for the pole values, we can proceed to the more subtle solution of the  $G$ -matrix equation

$$\begin{bmatrix} G_{--}^{12} & G_{-+}^{12} \\ G_{+-}^{12} & G_{++}^{12} \end{bmatrix} = \begin{bmatrix} R_{--}^{12} & R_{-+}^{12} \\ R_{+-}^{12} & R_{++}^{12} \end{bmatrix} + iA(k_p) \begin{bmatrix} R_{--}^{1p} & R_{-+}^{1p} \\ R_{+-}^{1p} & R_{++}^{1p} \end{bmatrix} \begin{bmatrix} G_{--}^{p2} & G_{-+}^{p2} \\ G_{+-}^{p2} & G_{++}^{p2} \end{bmatrix} \quad (\text{B.4})$$

where  $A(k_p)$  is as given in Eq. (4.32). As in the single channel case, we note that the arguments of  $G$  on the LHS and RHS differ, so we first solve for the half on-shell  $\begin{bmatrix} G_{--}^{p2} & G_{-+}^{p2} \\ G_{+-}^{p2} & G_{++}^{p2} \end{bmatrix}$  by letting  $1 \rightarrow p$ , equivalent to letting  $k_r = k_p$ . Then Eq. (B.4) leads

to

$$\begin{bmatrix} G_{--}^{p2} & G_{-+}^{p2} \\ G_{+-}^{p2} & G_{++}^{p2} \end{bmatrix} = \begin{bmatrix} R_{--}^{p2} & R_{-+}^{p2} \\ R_{+-}^{p2} & R_{++}^{p2} \end{bmatrix} + iA(k_p) \begin{bmatrix} R_{--}^{pp} & R_{-+}^{pp} \\ R_{+-}^{pp} & R_{++}^{pp} \end{bmatrix} \begin{bmatrix} G_{--}^{p2} & G_{-+}^{p2} \\ G_{+-}^{p2} & G_{++}^{p2} \end{bmatrix}. \quad (\text{B.5})$$

Then, bringing the second term on the RHS to the left we have

$$-iA(k_p) \begin{bmatrix} R_{--}^{pp} & R_{-+}^{pp} \\ R_{+-}^{pp} & R_{++}^{pp} \end{bmatrix} \begin{bmatrix} G_{--}^{p2} & G_{-+}^{p2} \\ G_{+-}^{p2} & G_{++}^{p2} \end{bmatrix} + \begin{bmatrix} G_{--}^{p2} & G_{-+}^{p2} \\ G_{+-}^{p2} & G_{++}^{p2} \end{bmatrix} = \begin{bmatrix} R_{--}^{p2} & R_{-+}^{p2} \\ R_{+-}^{p2} & R_{++}^{p2} \end{bmatrix}. \quad (\text{B.6})$$

Now we can combine terms on the left by factoring out the  $G$ -matrix to the right, yielding

$$\begin{bmatrix} 1 - iA(k_p)R_{--}^{pp} & -iA(k_p)R_{-+}^{pp} \\ -iA(k_p)R_{+-}^{pp} & 1 - iA(k_p)R_{++}^{pp} \end{bmatrix} \begin{bmatrix} G_{--}^{p2} & G_{-+}^{p2} \\ G_{+-}^{p2} & G_{++}^{p2} \end{bmatrix} = \begin{bmatrix} R_{--}^{p2} & R_{-+}^{p2} \\ R_{+-}^{p2} & R_{++}^{p2} \end{bmatrix}. \quad (\text{B.7})$$

Finally, by multiplying both side by the inverse of the first matrix on the LHS, we can solve for the half on-shell  $G$ -matrix .

$$\begin{bmatrix} G_{--}^{p2} & G_{-+}^{p2} \\ G_{+-}^{p2} & G_{++}^{p2} \end{bmatrix} = \begin{bmatrix} 1 - iA(k_p)R_{--}^{pp} & -iA(k_p)R_{-+}^{pp} \\ -iA(k_p)R_{+-}^{pp} & 1 - iA(k_p)R_{++}^{pp} \end{bmatrix}^{-1} \begin{bmatrix} R_{--}^{p2} & R_{-+}^{p2} \\ R_{+-}^{p2} & R_{++}^{p2} \end{bmatrix}. \quad (\text{B.8})$$

We can use Cramer's Rule to solve for the inverse as follows:

$$\begin{aligned} & \begin{bmatrix} 1 - iA(k_p)R_{--}^{pp} & -iA(k_p)R_{-+}^{pp} \\ -iA(k_p)R_{+-}^{pp} & 1 - iA(k_p)R_{++}^{pp} \end{bmatrix}^{-1} \\ &= \frac{1}{\Delta} \begin{bmatrix} 1 - iA(k_p)R_{++}^{pp} & -iA(k_p)R_{-+}^{pp} \\ -iA(k_p)R_{+-}^{pp} & 1 - iA(k_p)R_{--}^{pp} \end{bmatrix} \end{aligned} \quad (\text{B.9})$$

where  $\Delta$  is the determinant of the matrix we are inverting and

$$\Delta = (1 - iA(k_p)R_{--}^{pp})(1 - iA(k_p)R_{++}^{pp}) + A^2(k_p)R_{+-}^{pp}R_{-+}^{pp}. \quad (\text{B.10})$$

Using this result, we can solve for the half on-shell  $G$ .

$$\begin{bmatrix} G_{--}^{p2} & G_{-+}^{p2} \\ G_{+-}^{p2} & G_{++}^{p2} \end{bmatrix} = \frac{1}{\Delta} \begin{bmatrix} 1 - iA(k_p)R_{++}^{pp} & -iA(k_p)R_{-+}^{pp} \\ -iA(k_p)R_{+-}^{pp} & 1 - iA(k_p)R_{--}^{pp} \end{bmatrix} \begin{bmatrix} R_{--}^{p2} & R_{-+}^{p2} \\ R_{+-}^{p2} & R_{++}^{p2} \end{bmatrix}. \quad (\text{B.11})$$

Inserting this result into Eq. (B.4) yields, after some algebra,

$$\begin{aligned} G_{--}^{12} &= R_{--}^{12} - \frac{iA(k_p)}{\Delta} \\ &\quad \times \left[ R_{--}^{1p} \left( R_{--}^{p2} + iA(k_p)R_{++}^{pp}R_{--}^{p2} - iA(k_p)R_{-+}^{pp}R_{+-}^{p2} \right) \right. \\ &\quad \left. R_{-+}^{1p} \left( R_{+-}^{p2} + iA(k_p)R_{--}^{pp}R_{+-}^{p2} - iA(k_p)R_{+-}^{pp}R_{--}^{p2} \right) \right] \end{aligned} \quad (\text{B.12})$$

$$\begin{aligned} G_{-+}^{12} &= R_{-+}^{12} - \frac{iA(k_p)}{\Delta} \\ &\quad \times \left[ R_{--}^{1p} \left( R_{-+}^{p2} + iA(k_p)R_{++}^{pp}R_{-+}^{p2} - iA(k_p)R_{-+}^{pp}R_{++}^{p2} \right) \right. \\ &\quad \left. R_{-+}^{1p} \left( R_{++}^{p2} + iA(k_p)R_{--}^{pp}R_{++}^{p2} - iA(k_p)R_{+-}^{pp}R_{-+}^{p2} \right) \right] \end{aligned} \quad (\text{B.13})$$

$$\begin{aligned} G_{+-}^{12} &= R_{+-}^{12} - \frac{iA(k_p)}{\Delta} \\ &\quad \times \left[ R_{+-}^{1p} \left( R_{--}^{p2} + iA(k_p)R_{++}^{pp}R_{--}^{p2} - iA(k_p)R_{-+}^{pp}R_{+-}^{p2} \right) \right. \\ &\quad \left. R_{++}^{1p} \left( R_{+-}^{p2} + iA(k_p)R_{--}^{pp}R_{+-}^{p2} - iA(k_p)R_{+-}^{pp}R_{--}^{p2} \right) \right] \end{aligned} \quad (\text{B.14})$$

$$\begin{aligned} G_{++}^{12} &= R_{++}^{12} - \frac{iA(k_p)}{\Delta} \\ &\quad \times \left[ R_{+-}^{1p} \left( R_{-+}^{p2} + iA(k_p)R_{++}^{pp}R_{-+}^{p2} - iA(k_p)R_{-+}^{pp}R_{++}^{p2} \right) \right. \\ &\quad \left. R_{++}^{1p} \left( R_{++}^{p2} + iA(k_p)R_{--}^{pp}R_{++}^{p2} - iA(k_p)R_{+-}^{pp}R_{-+}^{p2} \right) \right]. \end{aligned} \quad (\text{B.15})$$

Finally, for completeness we can separate these  $G$ -matrix elements into real and imaginary parts. We note that only the determinant  $\Delta$  and the explicit factors of  $i$  are complex, so we can multiply Eqs. (B.12-B.15) by  $\frac{\Delta^*}{\Delta^*}$  to get a real denominator.

Then,

$$\Delta\Delta^* = (1 - A(k_p)(R_{++}^{pp}R_{--}^{pp} - R_{+-}^{pp}R_{-+}^{pp}))^2 + A^2(k_p)(R_{++}^{pp} + R_{--}^{pp})^2 \quad (\text{B.16})$$

and with some algebra in the numerators we can get both the real parts

$$\begin{aligned} \text{Re } G_{--}^{12} &= R_{--}^{12} - \frac{A(k_p)}{\Delta\Delta^*} \\ &\times \left[ A(k_p)(R_{++}^{pp} + R_{--}^{pp})(R_{--}^{1p}R_{--}^{p2} + R_{-+}^{1p}R_{+-}^{p2}) \right. \\ &- A(k_p)\left(1 - A^2(k_p)(R_{++}^{pp}R_{--}^{pp} - R_{+-}^{pp}R_{-+}^{pp})\right) \\ &\times \left. \left( R_{--}^{1p}R_{++}^{pp}R_{--}^{p2} - R_{--}^{1p}R_{-+}^{pp}R_{+-}^{p2} + R_{-+}^{1p}R_{--}^{pp}R_{+-}^{p2} - R_{-+}^{1p}R_{+-}^{pp}R_{--}^{p2} \right) \right] \quad (\text{B.17}) \end{aligned}$$

$$\begin{aligned} \text{Re } G_{-+}^{12} &= R_{-+}^{12} - \frac{A(k_p)}{\Delta\Delta^*} \\ &\times \left[ A(k_p)(R_{++}^{pp} + R_{--}^{pp})(R_{--}^{1p}R_{-+}^{p2} + R_{-+}^{1p}R_{++}^{p2}) \right. \\ &- A(k_p)\left(1 - A^2(k_p)(R_{++}^{pp}R_{--}^{pp} - R_{+-}^{pp}R_{-+}^{pp})\right) \\ &\times \left. \left( R_{--}^{1p}R_{++}^{pp}R_{-+}^{p2} - R_{--}^{1p}R_{-+}^{pp}R_{++}^{p2} + R_{-+}^{1p}R_{--}^{pp}R_{++}^{p2} - R_{-+}^{1p}R_{+-}^{pp}R_{--}^{p2} \right) \right] \quad (\text{B.18}) \end{aligned}$$

$$\begin{aligned} \text{Re } G_{+-}^{12} &= R_{+-}^{12} - \frac{A(k_p)}{\Delta\Delta^*} \\ &\times \left[ A(k_p)(R_{++}^{pp} + R_{--}^{pp})(R_{+-}^{1p}R_{--}^{p2} + R_{++}^{1p}R_{+-}^{p2}) \right. \\ &- A(k_p)\left(1 - A^2(k_p)(R_{++}^{pp}R_{--}^{pp} - R_{+-}^{pp}R_{-+}^{pp})\right) \\ &\times \left. \left( R_{+-}^{1p}R_{++}^{pp}R_{--}^{p2} - R_{+-}^{1p}R_{-+}^{pp}R_{+-}^{p2} + R_{++}^{1p}R_{--}^{pp}R_{+-}^{p2} - R_{++}^{1p}R_{+-}^{pp}R_{--}^{p2} \right) \right] \quad (\text{B.19}) \end{aligned}$$

$$\begin{aligned}
\text{Re } G_{++}^{12} &= R_{++}^{12} - \frac{A(k_p)}{\Delta\Delta^*} \\
&\times \left[ A(k_p)(R_{++}^{pp} + R_{--}^{pp})(R_{+-}^{1p}R_{-+}^{p2} + R_{++}^{1p}R_{++}^{p2}) \right. \\
&- A(k_p)\left(1 - A^2(k_p)(R_{++}^{pp}R_{--}^{pp} - R_{-+}^{pp}R_{+-}^{pp})\right) \\
&\left. \times \left( R_{+-}^{1p}R_{++}^{pp}R_{-+}^{p2} - R_{+-}^{1p}R_{-+}^{pp}R_{++}^{p2} + R_{++}^{1p}R_{--}^{pp}R_{++}^{p2} - R_{++}^{1p}R_{+-}^{pp}R_{-+}^{p2} \right) \right] \quad (\text{B.20})
\end{aligned}$$

and the imaginary parts

$$\begin{aligned}
\text{Im } G_{--}^{12} &= -\frac{A(k_p)}{\Delta\Delta^*} \quad (\text{B.21}) \\
&\times \left[ \left(1 - A^2(k_p)(R_{++}^{pp}R_{--}^{pp} - R_{-+}^{pp}R_{+-}^{pp})\right)(R_{--}^{1p}R_{--}^{p2} + R_{-+}^{1p}R_{+-}^{p2}) \right. \\
&\quad \left. + A^2(k_p)(R_{++}^{pp} + R_{--}^{pp}) \right. \\
&\left. \times \left( R_{--}^{1p}R_{++}^{pp}R_{--}^{p2} - R_{--}^{1p}R_{-+}^{pp}R_{+-}^{p2} + R_{-+}^{1p}R_{--}^{pp}R_{++}^{p2} - R_{-+}^{1p}R_{+-}^{pp}R_{--}^{p2} \right) \right]
\end{aligned}$$

$$\begin{aligned}
\text{Im } G_{-+}^{12} &= -\frac{A(k_p)}{\Delta\Delta^*} \quad (\text{B.22}) \\
&\times \left[ \left(1 - A^2(k_p)(R_{++}^{pp}R_{--}^{pp} - R_{-+}^{pp}R_{+-}^{pp})\right)(R_{--}^{1p}R_{-+}^{p2} + R_{-+}^{1p}R_{++}^{p2}) \right. \\
&\quad \left. + A^2(k_p)(R_{++}^{pp} + R_{--}^{pp}) \right. \\
&\left. \times \left( R_{--}^{1p}R_{++}^{pp}R_{-+}^{p2} - R_{--}^{1p}R_{-+}^{pp}R_{++}^{p2} + R_{-+}^{1p}R_{--}^{pp}R_{++}^{p2} - R_{-+}^{1p}R_{+-}^{pp}R_{--}^{p2} \right) \right]
\end{aligned}$$

$$\begin{aligned}
\text{Im } G_{+-}^{12} &= -\frac{A(k_p)}{\Delta\Delta^*} \quad (\text{B.23}) \\
&\times \left[ \left(1 - A^2(k_p)(R_{++}^{pp}R_{--}^{pp} - R_{-+}^{pp}R_{+-}^{pp})\right)(R_{+-}^{1p}R_{--}^{p2} + R_{++}^{1p}R_{+-}^{p2}) \right. \\
&\quad \left. + A^2(k_p)(R_{++}^{pp} + R_{--}^{pp}) \right. \\
&\left. \times \left( R_{+-}^{1p}R_{++}^{pp}R_{--}^{p2} - R_{+-}^{1p}R_{-+}^{pp}R_{++}^{p2} + R_{++}^{1p}R_{--}^{pp}R_{+-}^{p2} - R_{++}^{1p}R_{+-}^{pp}R_{--}^{p2} \right) \right]
\end{aligned}$$

$$\begin{aligned}
\text{Im } G_{++}^{12} &= -\frac{A(k_p)}{\Delta\Delta^*} & (\text{B.24}) \\
&\times \left[ \left( 1 - A^2(k_p)(R_{++}^{pp}R_{--}^{pp} - R_{-+}^{pp}R_{+-}^{pp}) \right) (R_{+-}^{1p}R_{-+}^{p2} + R_{++}^{1p}R_{++}^{p2}) \right. \\
&\quad \left. + A^2(k_p)(R_{++}^{pp} + R_{--}^{pp}) \right. \\
&\times \left. \left( R_{+-}^{1p}R_{++}^{pp}R_{-+}^{p2} - R_{+-}^{1p}R_{-+}^{pp}R_{++}^{p2} + R_{++}^{1p}R_{--}^{pp}R_{++}^{p2} - R_{++}^{1p}R_{+-}^{pp}R_{-+}^{p2} \right) \right].
\end{aligned}$$

In practice, we only need  $G_{++}^{12}$  and  $G_{--}^{12}$  for the present application and so do not compute the full off-shell  $G$ -matrix, although all of the technology is in place should we need it in the future.

# References

- [1] [http://gwdac.phys.gwu.edu/analysis/nn\\_analysis.html](http://gwdac.phys.gwu.edu/analysis/nn_analysis.html), 2011.
- [2] M. Abrahamowitz and I. A. Stegun, editors. *Handbook of Mathematical Functions*. Dover, New York, 1964.
- [3] A. Amorim and J. A. Tjon. *Phys. Rev. Lett.*, 68:772, 1992.
- [4] H. F. Arellano and J. P. Delaroche. *Phys. Rev. C*, 83:044306, 2011.
- [5] R. A. Arndt and M. H. MacGregor. *Phys. Rev.*, 141:1873, 1966.
- [6] M. Baldo. *Nuclear Methods and the Nuclear Equation of State*. World Scientific, New Jersey, 1999.
- [7] M. Baldo, I. Bombaci, L. S. Ferreira, G. Giansiracusa, and U. Lombardo. *Phys. Rev. C*, 43:2605, 1991.
- [8] G. F. Bertsch, L. Frankfurt, and M. Strikman. *Science*, 259:773, 1993.
- [9] H. A. Bethe. *Rev. Mod. Phys.*, 96:139, 1936.
- [10] H. A. Bethe. *Phys. Rev. A.*, 103:1343, 1956.
- [11] R. Brockman and R. Machleidt. *Phys. Rev. C*, 42:1965, 1990.
- [12] G.E. Brown and A.D. Jackson. *The Nucleon Nucleon Interaction*. North-Holland, Amsterdam, 1976.
- [13] K. A. Brueckner and J. L. Gammel. *Phys. Rev.*, 109:1023, 1958.

- [14] K. A. Brueckner and C. A. Levinson. *Phys. Rev.*, 97:1344, 1955.
- [15] T. A. Carey et al. *Phys. Rev. Lett.*, 53:144, 1984.
- [16] J. Carlson, V. R. Pandharipande, and R. B. Wiringa. *Nuc. Phys. A*, 401:59, 1983.
- [17] F. Coester, S. Cohen, B. Day, and C. M. Vincent. *Phys. Rev. C*, 1:769, 1970.
- [18] B. D. Day. *Phys. Rev. C*, 24:1203, 1981.
- [19] B. D. Day and R. B. Wiringa. *Phys. Rev. C*, 32:1057, 1985.
- [20] A. Deltuva, A. C. Fonseca, and P. U. Sauer. *Phys. Rev. C*, 71:054005, 2005.
- [21] Y. Dewulf, W. H. Dickhoff, D. Van Neck, E. R. Stoddard, and M. Waroquier. *Phys. Rev. Lett.*, 90:152501, 2003.
- [22] W. H. Dickhoff, A. Faessler, and H. Müther. *Nucl. Phys.*, A389:492, 1982.
- [23] W. H. Dickhoff and E. P. Roth. *Acta Phys. Pol.*, B33:65, 2002.
- [24] W. H. Dickhoff and D. Van Neck. *Many-Body Theory Exposed!, 2nd edition*. World Scientific, New Jersey, 2008.
- [25] C. Elster, W. Ferchländer, K. Holinde, D. Schütte, and R. Machleidt. *Phys. Rev. C*, 37:1647, 1988.
- [26] D. R. Entem and R. Machleidt. *Phys. Rev. C*, 66:014002, 2002.
- [27] D. R. Entem and R. Machleidt. *Phys. Rev. C*, 68:014001, 2003.
- [28] L.D. Faddeev. *Sov Phys JETP*, 12:1014, 1961.
- [29] A. L. Fetter and J. D. Walecka. *Quantum Theory of Many-Particle Physics*. McGraw-Hill, New York, 1971.
- [30] T. Frick, H. Müther, A. Rios, A. Polls, and A. Ramos. *Phys. Rev. C*, 71:014313, 2005.



- [31] B. Frois et al. *Phys. Rev. Lett.*, 38:152, 1977.
- [32] V. M. Galitskii. *Sov. Phys. JETP*, 7:104, 1958.
- [33] M. I. Haftel and F Tabakin. *Nucl. Phys. A*, 158:1, 2003.
- [34] K. Hatanaka et al. *Phys. Rev. Lett.*, 78:1014, 1997.
- [35] N. Ishii, S. Aoki, and T. Hatsuda. *Phys. Rev. Lett.*, 99:022001, 2007.
- [36] J. P. Jeukenne, A. Lejeune, and C. Mahaux. *Phys. Rep.*, 25C:83, 1976.
- [37] T. Kobayashi et al. *Nucl. Phys. A*, 805:431, 2008.
- [38] L. Lapikás. *Nucl. Phys.*, A553:297c, 1993.
- [39] R. Machleidt. *Adv. Nucl. Phys.*, 19:189, 1989.
- [40] R. Machleidt. *Phys. Rev. C*, 63:024001, 2001.
- [41] R. Machleidt, K. Holinde, and C. Elster. *Phys. Rep.*, 149:1, 1987.
- [42] R. Machleidt, F. Sammarruca, and Y. Song. *Phys. Rev. C*, 53:R1463, 1996.
- [43] G. D. Mahan. *Comm. Cond. Matt. Phys.*, 16:333, 1994.
- [44] A. B. Migdal. *Sov. Phys.-JETP*, 34:1184, 1972.
- [45] H. Müther and W. H. Dickhoff. *Phys. Rev. C*, 72:054313, 2005.
- [46] H. Müther and A. Polls. *Phys. Rev. C*, 61:014304, 2000.
- [47] H. Müther, A. Polls, and R. Machleidt. *Phys. Lett. B*, 445:256, 1999.
- [48] T. Noro. Quasifree scattering with radioactive ion beams. ECT\* Workshop presentation, 2008.
- [49] T. Noro et al. *Phys. Rev. C*, 72:041602(R), 2005.
- [50] E. Oset, H. Toki, and W. Weise. *Phys. Rep.*, 83:281, 1982.

- [51] V. R. Pandharipande, I. Sick, and P. K. A. de Witt Huberts. *Rev. Mod. Phys.*, 69:981, 1997.
- [52] R. Rajaraman and H. A. Bethe. *Rev. Mod. Phys.*, 39:745, 1967.
- [53] A. Ramos. *Ph.D. Thesis*. University of Barcelona, 1988.
- [54] R. V. Reid. *Ann. Phys.*, 50:411, 1968.
- [55] A. Rios, A. Polls, and W. H. Dickhoff. *Phys. Rev. C*, 79:064308, 2009.
- [56] E. Schiller, H Müther, and P. Czerski. *Phys. Rev. C*, 59:2934, 1999.
- [57] E. Schiller, H Müther, and P. Czerski. *Phys. Rev. C*, 60:059901, 1999.
- [58] M. Schwamb and H. Arenhövel. *Nucl. Phys.*, A690:647, 2001.
- [59] H. Q. Song, M. Baldo, G. Giansiracusa, and U. Lombardo. *Phys. Rev. Lett.*, 81:1584, 1998.
- [60] V. G. J. Stoks, R. A. M. Klomp, C. P. F. Terheggen, and J. J. de Swart. *Phys. Rev. C*, 48:792, 1993.
- [61] K. Suzuki, R. Okamoto, M Kohno, and S. Nagata. *Nucl. Phys.*, A665:92, 2000.
- [62] T. N. Taddeucci et al. *Phys. Rev. Lett.*, 73:3516, 1994.
- [63] B. ter Haar and R. Malfliet. *Phys. Rev. Lett.*, 56:1237, 1986.
- [64] M. Trefz, A. Faessler, and W. H. Dickhoff. *Nucl. Phys.*, A443:499, 1985.
- [65] M. F. van Batenburg. PhD thesis, University of Utrecht, 2001.
- [66] C.F. von Weizsäcker. *Z. Phys.*, 96:431, 1935.
- [67] B. E. Vonderfecht, C. C. Gearhart, W. H. Dickhoff, A. Polls, and A. Ramos. *Phys. Lett. B*, 253, 1991.
- [68] T. Wakasa et al. *Phys. Rev. C*, 59:3177, 1999.

- [69] R. B. Wiringa, R. A. Smith, and T. L. Ainsworth. *Phys.Rev. C*, 29:1207, 1984.
- [70] R. B. Wiringa, V. G. J. Stoks, and R. Schiavilla. *Phys.Rev. C*, 51:38, 1995.
- [71] H. Yukawa. *Proc. Phys. Math. Soc. Jpn*, 17:48, 1935.